PHOTONIC APPROACHES FOR THE THERMAL CONTROL OF PHOTOVOLTAICS

A Thesis submitted for the degree of Doctor of Philosophy by

GEORGE PERRAKIS

Supervisor: Prof. Maria Kafesaki

University of Crete, Department of Materials Science and Technology
&
Foundation for Research and Technology (FORTH), Institute of Electronic Structure and Laser (IESL)

Heraklion, Crete, April 2021

ACKNOWLEDGEMENTS

I would like to express my deepest appreciation to my advisor Prof. Maria Kafesaki for her patience, relentless support and guidance all these years of my Ph.D. research. Her continuous assistance, knowledge, and motivation were truly invaluable to make this thesis a reality. I wish to sincerely thank Dr. George Kenanakis for all his patience and constant support throughout my studies, always willing to provide knowledge and help. Additionally, I would like to especially acknowledge Prof. Stelios Tzortzakis for all his help and the contribution to my committee.

Special thanks to all the members of the Photonic- Phononic- and Metamaterials (PPM) group for the assistance and the warm and friendly atmosphere. Moreover, my sincere regards go to Dr. Anna Tasolamprou for all her assistance and research feedback, as well as the fruitful collaboration in several projects.

I would like to thank the Foundation for Research and Technology - Hellas (FORTH) for the financial support throughout my studies.

Besides my advisors, I wish to also thank all the members of my thesis committee: Dr. Emmanuel Stratakis, Prof. Dimitris Papazoglou, Prof. Nikos Pelekanos and Prof. Elefterios Lidorikis for accepting to evaluate my Ph.D. thesis.

Finally, special and warm thanks go to my Ritsa, my family and my friends for their patience and support in every way.

ABSTRACT

Current state-of-the-art solar cell technology converts incident solar to electrical power with a conversion efficiency that has reached values of up to ~22.8 % when operating at Standard Test Conditions (STC) (i.e., 1000 W/m² irradiance, cell temperature 25 ^{o}C). These conditions though are rarely met in practice, where the module temperature significantly rises, reaching values even ≥20 degrees higher than 25 ^{o}C, especially in the Summer. The relative photovoltaic (PV) efficiency drops by ~-0.3 to -0.5 %/^{o}C (depending on solar cell's architecture). Additionally, providing no further cooling approaches may accelerate PV's thermally activated power degradation significantly. Important parameters for the temperature rise in solar cells are the solar irradiation level, increased ambient temperature and low wind speeds in conjunction with the unoptimized cooling and heat dissipation.

Conventional strategies for solar cell cooling are mainly focused on non-radiative heat transfer, i.e., through forced air flow or heat-pipe-based cooling etc., most of which consume extra energy (usually for pumping) or water (if water is utilized as the circulating cooling fluid) or increase system's complexity if the cooling structures are integrated into actual systems. Recently, due to current advances in fabrication technology, studies demonstrated for the first time passive (i.e., no extra energy input needed) daytime photonic cooling in the form of radiative heat transfer, despite the fact that the structures were exposed to direct solar irradiance. Interestingly, the radiative cooling of an earth object is possible because when it faces the sky, it has radiative access to the coldness of the universe (~ -270 ^{o}C), through the atmospheric transparency window in the mid-infrared wavelengths (mid-IR – 8-13 μm). By engineering, through photonics, the reflection properties of a surface in the solar wavelengths (reflecting sunlight and reducing this way heat generation), and providing selective (within the atmospheric window) high amplitude thermal emission, efficient temperature reductions below the ambient were demonstrated.

A photovoltaic, by necessity, faces the sky. Therefore, it is of great importance to examine the requirements, constraints and impact for daytime radiative cooling and other photonic heat reduction techniques to be implemented in photovoltaic systems, where also the absorption of incident sunlight is critical for their performance.

In the present thesis, to answer this question we develop an opto-electro-thermal model that accurately describes the effects of the photonic cooling strategies not only on the PV operating temperature but also on its efficiency

in power conversion. Applying the proposed modeling we identify the impact of PV reflection/transmission/absorption properties on the PV temperature and PV efficiency, and we identify the materials and design requirements for maximum temperature-drop and efficiency-enhancement in PVs. Finally, we propose realistic photonic coolers compatible with photovoltaics where a main aim in the photonic coolers' design was the reduced complexity and fabrication feasibility. Particularly, fabrication simplicity and low cost are very important factors in the PV industry, in order also for such cooling structures and their associated efficiency and temperature gains to enter rapidly into the market.

Our results demonstrate that radiative cooling and photonic heat reduction techniques in general can lower PV temperature and enhance the output electrical power when appropriate materials together with appropriate photonic designs are effectively combined, even in the case of structures with reduced complexity.

CONTENTS

1

INTRODUCTION

1.1 INTRODUCTION

According to the U.S. Energy Information Administration (EIA) [1], ~85 % of the primary energy consumption in the world is sourced from fossil fuels (crude oil, coal, natural gas etc.). Fossil fuels are excellent to use for the energy base-load, since they are cheap (average cost around $0.05/kWh) and reliable as well as well-developed. On the other hand, recognizing that fossil fuels are finite and world energy consumption keeps increasing (see Fig. 1.1), it implies that there are supply constraints of fossil fuels.

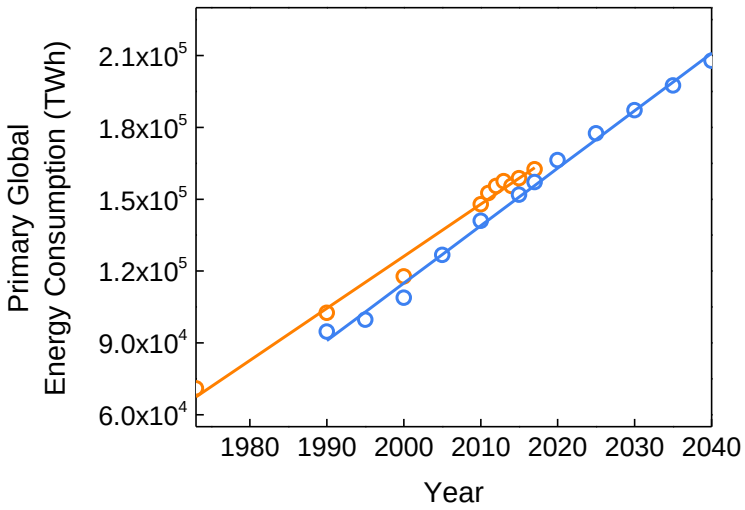

Fig. 1.1: Primary (total energy demand – orange circles) and primary-projected (blue circles) global energy consumption (in TWh) per year, extracted from [2,3], and their linear-fitting lines.

Based on British Petroleum's (BP's) Statistical Review of World Energy, there is still around 1,000,000 Mtoe of proven reserves of fossil fuels. To give a static (based on the current rate of production) indicative estimate of how long we could feasibly consume fossil fuels for, we'd have about 115 years of coal production and roughly 50 years of both oil and natural gas remaining.

The solar energy source is a promising alternative to fulfill our energy needs since it is renewable and sustainable (one hour of earth's solar energy absorption would cover world's entire energy demand for one year). Additionally, the potential harnessing of solar energy in the terawatt-scale could contribute to decarbonization, reducing greenhouse gas emissions such as CO_2 or CH_4. In fact, examining the issue of CO_2 emissions from the supply side, and even if the contribution of the non-conventional fossil fuels is excluded [4], studies have shown that the climate change is the more urgent issue to face compared to the fossil fuel resource constraints.

Currently, the crucial factor for renewable solar energy technologies to penetrate drastically into the market is the cost. Fossil fuel prices average around \$0.05/kWh (\$0.03/kWh for natural gas). Until the past decade, no alternative energy resource came close competing that prices. Surprisingly though, in the last decade, electricity cost from conventional silicon-based solar photovoltaics (PVs) has rapidly dropped by a factor of 10, largely due to module cost reductions and the recent advances in solar technologies. In particular, in 2014, the PV technology gained cost-competitive values producing solar energy even for an average price as low as \$0.05/kWh, factoring in subsidies and incentives [5]. Record low solar energy prices were achieved in 2016. That year, bids awarded in several tenders were as low as \$0.029/kWh unsubsidized (up to ~\$0.0234/kWh in 2018, and up to ~\$0.016/kWh in 2020), effectively leveling fossil fuels' cheapest offerings.

PV's technology recent cost-competitive values together with its higher reliability compared to other renewable energy sources (like wind power) made photovoltaics the fastest growing power generation source in recent years [6]. Indicatively, in 2018, additions of renewable power capacity from solar PVs accounted for 55% (~100 GW added, raising their cumulative installed capacity to above half a Terawatt), followed by wind power (28%) and hydropower (11%). In 2018, PVs have contributed to roughly 2.5% [over 550 Terawatt-hour (TWh)] of the world's electricity generation (~23000 TWh). The current PV growth rate is on track to reach the levels envisioned by the International Energy Agency (IEA) [2], which targets a 2030 global PV generation of >2500 TWh, producing thus in the terawatt-scale and potentially mitigating effectively the climate change in the future. As a consequence, solar PV source has become a viable energy solution. Therefore, to enhance or even

maintain the current rate of PV deployment, further advancements in the solar PV industry are required. Innovations in nanotechnology and quantum physics allow the levelized cost of electricity to keep dropping by increasing the efficiency or the lifetime [7] of the solar panels or even modifying their intermittent nature [8]. Specifically, the field of photonics, which explores the use of light molding techniques in the range of visible and infrared, is an important candidate to optimize further the interaction of PVs with light. Current advances in fabrication technology allow to control the geometry of various materials and decrease their size down to the light scale, i.e., micro- or even nano-scale regime (< 1 μm), in a practical manner, for large scale production. As a result, novel ways to tailor the flow of light become available, compatible with PV requirements, such as optimized performance by effectively maintaining fabrication simplicity.

Despite though the recent advances, there is still plenty of space for improvements in the PV-related technologies. In this study, we are interested in one of the limitations of the technology, which is related to the high temperatures that are developed in the PV systems when exposed under the sun. Although the sunlight is the source of energy to be converted to the desired electric one, it comes always and inevitably with an unwanted conversion to heat. Just like any energy conversion device, PVs are subject to waste heat. The reason that heat turns out to be a problem is clearly shown in Fig. 1.2.

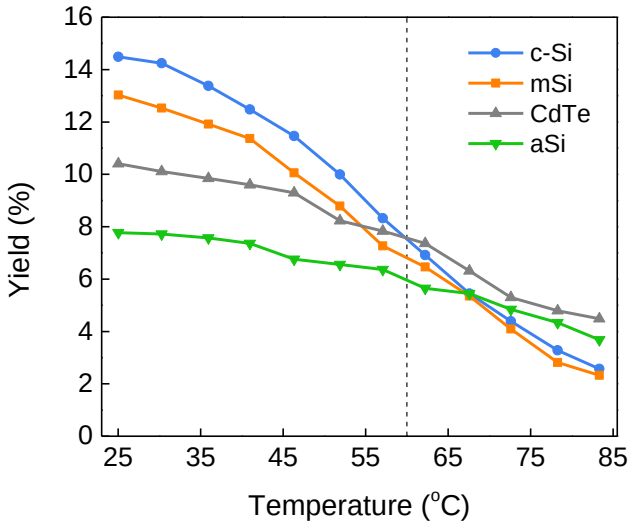

Fig. 1.2: Operating temperature dependence of the PV yield, for various PV technologies available in the market: crystalline silicon- (blue), multicrystalline silicon- (orange), cadmium telluride- (gray) and amorphous silicon-based (green). Results extracted from

Dr. Abu-Zaid at Masdar, tested in UAE field conditions. Cases at the right of the vertical line correspond to PV's temperature in Summer.

As operating temperature increases the PV yield decreases. The lifetime of the PVs reduces as well [9]. This can be quite severe especially in countries where temperatures can reach very high values. Indicatively, for a crystalline silicon solar cell, every 1 K temperature rise leads to a relative efficiency decline [10] of about 0.45 %. Moreover, the aging rate of a solar cell array doubles for every 10 K solar cell temperature increase [9]. Although there are a number of cooling techniques that help reducing the temperature, they nevertheless come at an energetic cost and thus there is a compromise in the gain from the increased PV efficiency against the energy expended for the cooling. Conventional strategies for cooling are mainly focused on non-radiative heat transfer via conduction or convection, like forced air flow [11], water cooling [12], heat-pipe-based systems [13], etc., most of which consume extra energy or increase system's complexity.

In this thesis, we are interested on the heat energy transfer in the form of electromagnetic radiation. Radiative energy transfer may provide an alternative to dissipate heat at the environment, it is passive (i.e., no extra energy input needed), and thus achieves energy-cost-free temperature reduction in PVs, and can be used in conjunction with conventional non-radiative cooling techniques. As shown in Fig. 1.2, PV operating temperatures can reach high values, higher than ambient temperature, ~300 K, due to the increased heat load arising by the sunlight absorption (sun temperature ~5778 K). From the second law thermodynamics, there must be a net radiative/non-radiative power outflow at the atmosphere. Furthermore, when an earth object faces the sky, it has radiative access to the coldness of the universe (~3 K), through the atmospheric transparency window in the mid-IR (8-13 μm). Therefore, a terrestrial surface may additionally dissipate waste heat radiatively to outer space, of a much lower temperature (~3 K) than that of the atmosphere (~ 300 K). This approach, i.e., to exploit the lower temperature of the outer space through radiative heat transfer at the atmospheric window, is known as the *Passive Radiative Cooling* (PRC) strategy and it is an appealing cooling approach to be examined in the case of PVs. Exploiting this approach, one can further tune the radiative properties of a device, i.e., reflection, transmission, to reduce the non-useful absorption from the sun and thus decrease the thermal load.

In the current thesis we intend to explore the use of light molding techniques to enhance the radiative cooling of highly-efficient and mainstream crystalline silicon-based PVs that are available in the market. To examine the physical mechanisms of how heat affects PVs' operating temperature and

energy conversion efficiency, as well as the requirements and potential for reducing the temperature and increasing the efficiency radiatively, by means of photonics, we develop an opto-electro-thermal modeling, which accurately describes the outdoor operation of selected PV architectures. A significant advantage of the proposed modeling, compared to literature, is that it further validates how much the absorption efficiency of the PV cells, i.e., the absorption inside the active layer where the conversion of the incident solar power to electricity takes place, is affected by the requirements for radiative cooling. This is a key factor to definitely conclude whether radiative cooling techniques can enhance the PV yield. In parallel and in order to further increase the overall performance of photovoltaics, we intend to enhance the useful absorptivity in the PV cells using solutions involving nano- or micro-patterning of the top PV surface as to lower its reflectivity.

Concluding, this work aims at developing new optimizations of the PV device-parameters that would include thermal criteria in addition to the optical and electrical ones.

1.2 OUTLINE

This thesis is organized as follows: In Chapter 2 we discuss the main photonic concepts relevant with passive radiative cooling and absorption enhancement in photovoltaics.

In Chapter 3 we exploit the principles of passive radiative cooling and we examine when a material can be considered as a radiative cooler. We further discuss the requirements for cooling radiatively photovoltaics.

In Chapter 4 we describe the features of solar cell operation as well as the physical mechanisms of how heat affects PVs' operating temperature and conversion efficiency. Specifically, the optical, electrical and thermal properties of commercial crystalline silicon-based photovoltaic modules are outlined. Moreover, we develop a coupled thermal-electrical modeling to address how a radiative cooler affects the overall efficiency of commercial photovoltaic modules operating outdoors and how the radiative cooling impact is compared to other photonic strategies for reducing heat generation within PVs, such as harmful ultraviolet and sub-bandgap (i.e., beyond the absorption band of the active layer, for silicon ~1.1-4.0 μm) radiation reflection.

In Chapter 5 we describe the electrical mechanisms and theoretical potential for reducing PVs' operating temperature and increasing the efficiency radiatively, i.e., by employing optimized radiative cooling or other

radiative techniques for reducing heat generation, like filtering sub-bandgap and detrimental UV radiation (the main power degradation factor in PVs, that degrades their performance, lifetime and reliability).

Subsequently, in Chapter 6 we propose some realistic photonic designs that fulfill the radiative cooling requirements and we evaluate (exploiting the proposed modeling described in Chapter 4) their impact on the overall efficiency of a realistic PV system operating outdoors.

Finally, in Chapter 7 we summarize our work and present an outlook.

1.3 PUBLICATIONS IN THE FRAMEWORK OF THIS THESIS

1. Perrakis, G., Tasolamprou, A. C., Kenanakis, G., Economou, E. N., Tzortzakis, S., & Kafesaki, M. *Combined nano and micro structuring for enhanced radiative cooling and efficiency of photovoltaic cells.* Scientific Reports, Under Revision (2021)

2. Perrakis, G., Tasolamprou, A. C., Kenanakis, G., Economou, E. N., Tzortzakis, S., & Kafesaki, M. *Passive radiative cooling and other photonic approaches for the temperature control of photovoltaics: A comparative study for crystalline silicon-based architectures.* Optics Express, 28(13), 18548-18565 (2020)

3. Perrakis, G., Tasolamprou, A. C., Kenanakis, G., Economou, E. N., Tzortzakis, S., & Kafesaki, M. *Ultraviolet radiation impact on the efficiency of commercial crystalline silicon-based photovoltaics: A theoretical thermal-electrical study in realistic device architectures.* OSA Continuum, 3(6), 1436-1444 (2020)

4. Perrakis, G., Kakavelakis, G., Kenanakis, G., Petridis, C., Stratakis, E., Kafesaki, M., & Kymakis, E. *Efficient and environmental-friendly perovskite solar cells via embedding plasmonic nanoparticles: an optical simulation study on realistic device architectures.* Optics Express, 27(22), 31144-31163 (2019)

5. Perrakis, G., Tsilipakos, O., Kenanakis, G., Kafesaki, M., Soukoulis, C. M., & Economou, E. N. *Perfect optical absorption with*

nanostructured metal films: design and experimental demonstration. Optics Express, 27(5), 6842-6850 (2019)

6. Papadopoulos, A., Skoulas, E., Mimidis, A., Perrakis, G., Kenanakis, G., Tsibidis, G. D., & Stratakis, E. *Biomimetic omnidirectional antireflective glass via direct ultrafast laser nanostructuring.* Advanced Materials, 31(32), 1901123 (2019)

7. Viskadourakis, Z., Perrakis, G., Symeou, E., Giapintzakis, J., & Kenanakis, G. *Transport properties of 3D printed polymer nanocomposites for potential thermoelectric applications.* Applied Physics A, 125(3), 1-10 (2019)

2

PHOTONIC CONCEPTS

2.1 INTRODUCTION

Photons are everywhere around us and are involved in most of the aspects of our everyday life. Photonic applications aim to control the flow of light, mostly in the range of visible and near-infrared, and extend from energy production to information detection and processing. Some examples are the regulation of the light intensity passing through certain routes, light confinement in space, light emission, amplification and detection by optical elements, including laser devices and other light sources, optical fibers and electro-optical devices.

The behavior of electric and magnetic fields is governed by Maxwell equations [14]. In SI units, they are

$$\nabla \cdot \boldsymbol{D} = \rho, \quad (2.1)$$
$$\nabla \cdot \boldsymbol{B} = 0, \quad (2.2)$$
$$\nabla \times \boldsymbol{E} + \partial \boldsymbol{B}/\partial t = 0, \quad (2.3)$$
$$\nabla \times \boldsymbol{H} - \partial \boldsymbol{D}/\partial t = \boldsymbol{J}, \quad (2.4)$$

where $\boldsymbol{E}$ and $\boldsymbol{H}$ are the electric and magnetic field in V/m and A/m, respectively, $\boldsymbol{D}$ and $\boldsymbol{B}$ are the electric displacement field and magnetic induction, in Cb/m^2 and Wb/m^2 respectively, and ρ and $\boldsymbol{J}$ are the volumetric external charge and current density, in Cb/m^3 and A/m^2, respectively. The charge and current density are the sources of the electromagnetic field and they are usually localized in space, such as the current in an antenna.

The relations of $\boldsymbol{E}$ with $\boldsymbol{D}$ and of $\boldsymbol{H}$ with $\boldsymbol{B}$, often called constitutive relations, specify the response of matter, specifically the response of bound charge and current, to the applied fields. In a linear, homogeneous and isotropic medium, $\boldsymbol{E}$ and $\boldsymbol{D}$ and $\boldsymbol{H}$ and $\boldsymbol{B}$ are related by

$$\boldsymbol{D} = \varepsilon_0 \varepsilon \boldsymbol{E}, \quad (2.5)$$
$$\boldsymbol{B} = \mu_0 \mu \boldsymbol{H}, \quad (2.6)$$

where ε_0 and μ_0 are the vacuum electric permittivity (ε_0=8.85×10^{-12} Farad/m) and magnetic permeability (μ_0=4π×10^{-7} Henry/m), respectively, and ε, μ, the relative permittivity and permeability, respectively.

Assuming a freely propagating, monochromatic, i.e., of certain angular frequency, ω, EM wave with harmonic time dependence of the form $\boldsymbol{E}(\boldsymbol{r})e^{-i\omega t}$, propagating in a homogeneous medium, its electric field profile, $\boldsymbol{E}(\boldsymbol{r})$, fulfills the time-independent vector wave equation which follows from the Maxwell equations [14]. For $n = \sqrt{\varepsilon}$ being the constant refractive index of the medium (and μ=1), this equation reads as

$$\nabla \times \nabla \times \boldsymbol{E}(\boldsymbol{r}) - (k_0 n)^2 \boldsymbol{E}(\boldsymbol{r}) = 0, \quad (2.7)$$

where $k_0=\omega/c_0$, and $c_0 = 1/\sqrt{\varepsilon_0 \mu_0}$ is the speed of light in vacuum. If we identify the left term of the wave equation as an operator $\hat{\Theta} = (1/n^2)\nabla \times \nabla \times$ (dividing also by n^2) acting on $\boldsymbol{E}(\boldsymbol{r})$, Equation (2.7) is written as a traditional eigenvalue equation:

$$\hat{\Theta}\boldsymbol{E}(\boldsymbol{r}) = (\omega/c_0)^2 \boldsymbol{E}(\boldsymbol{r}), \quad (2.8)$$

The eigenvectors $\boldsymbol{E}(\boldsymbol{r})$ are the spatial patterns of the harmonic modes. For a homogeneous medium they are of the form $\boldsymbol{E}(\boldsymbol{r})=\boldsymbol{E}_0 e^{-i\boldsymbol{k}\boldsymbol{r}}$, where $\boldsymbol{E}_0$ is a constant vector; the eigenvalues are proportional to the squared frequencies of those modes $(\omega/c_0)^2=|\boldsymbol{k}|^2/n^2$, yielding the well-known dispersion relation

$$\omega(k) = c_0 k/\sqrt{\varepsilon}, \quad (2.9)$$

Equation (2.9) implies that photons travelling in a higher refractive index medium have larger momentum (the canonical momentum of a photon, p, follows the expression $p=h|\boldsymbol{k}|/2\pi$, where h is Planck's constant) as $|\boldsymbol{k}|$ depends linearly on the refractive index.

Note that the spatial dependence of a mode EM field profile is affected by its environment, resulting to a different dispersion relation for a non-homogeneous medium. For simpler cases, the eigenfield profiles are analytically known, in most cases, though, they need to be solved numerically.

The main interest of this study is on energy harvesting in PVs. In this case, one needs to reduce, sufficiently, the heat arising by the absorption of the unwanted incident solar radiation and at the same time enhance device's

absorption at the beneficial wavelengths. I.e., the utilization of photonics aims to control the flow of light in two main ways: by selectively reflecting or coupling with incident radiation, thus selectively decreasing or increasing the absorption of the device, respectively.

Aside from improving in-coupling, one can utilize photonic structures to enhance the emission properties of PVs. The thermal radiation emission enhancement of PV devices at the thermal wavelengths, inside the atmospheric transparency window (8-13 μm), together with the reduction of the thermal load (through proper reflection) may result to efficient passive (i.e., no extra energy input needed) radiative cooling, thus lowering the operating temperature of the device and increasing the PV yield [15,16].

To reflect unwanted sunlight, photonic structures known as *Photonic Crystals* (PCs) may be utilized that reflect incident radiation as a consequence of their photonic bandgap, where radiation propagation is forbidden (Section 2.2). To increase the absorption and the thermal emission, the utilization of other appropriate photonic structures (besides PCs) aims to increase the number of photons reaching the appropriate layer and their interaction time with matter. This could be achieved by confining light in space either through non-propagating localization or restricting light to propagate confined in space along a desired route, known as confined or *guided* propagation (Sections 2.3, and 2.4).

2.2 BASIC PHOTONIC CRYSTAL CONCEPTS AND BANDGAP ORIGIN

Photonic crystals (PCs), the optical analogue of semiconductor crystals in quantum mechanics, have been extensively examined in the framework of solar cell applications and in passive radiative cooling due to their undeniable potential of controlling completely the light propagation. In PCs the atoms or molecules of semiconductor crystals are replaced by macroscopic media with differing dielectric constants, and the periodic atomic potential is replaced by a periodic dielectric function (or, equivalently, a periodic index of refraction) (see Fig. 2.1).

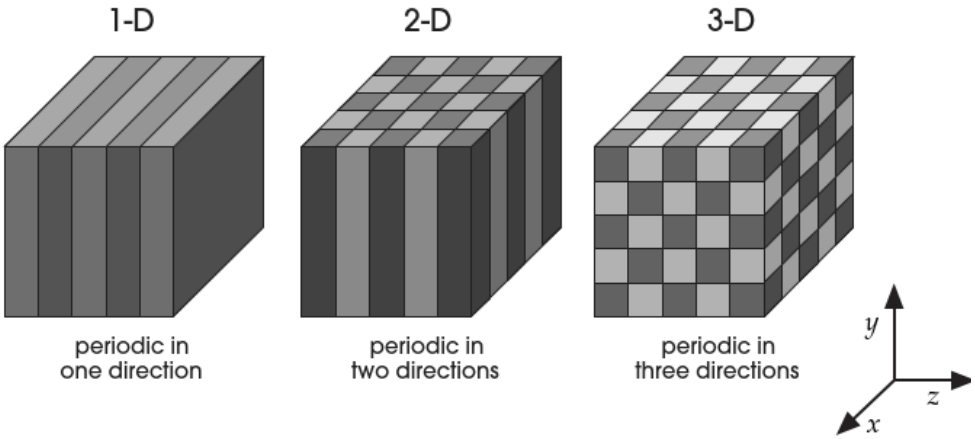

Fig. 2.1: Simple examples of one-, two-, and three-dimensional photonic crystals. The different colors represent materials with different dielectric constants. The defining feature of a photonic crystal is the periodicity of dielectric material along one or more axes. Image adopted from Ref. [17].

The refractions and reflections of light from all of the various PC interfaces can produce for photons (light modes) many of the phenomena that the atomic potential produces for electrons, like gaps, known as photonic bandgaps, i.e., frequency regions where radiation propagation is forbidden. If, for some frequency range, a photonic crystal prohibits the propagation of electromagnetic waves of any polarization traveling in any direction, we say that the crystal has a complete photonic band gap, implying that any incident radiation upon the photonic crystal is reflected. By choosing the appropriate materials, dimensions, and periodicity of the PC, one can control over wave propagation and tune the spectral position and size of the bandgap, hence, selectively reflect or couple with incident radiation.

To explain the physical origin of the photonic bandgap, we take advantage of the simplicity of the one-dimensional (1D) PC (see left 1D PC in Fig. 2.1). If we consider waves that propagate entirely in the *z* direction ($\boldsymbol{k}_{//} = 0$ along *x*-, *y*-axis), crossing the sheets of dielectric at normal incidence, only the k_z wave vector component is important and we can abbreviate it by *k*. For this system (the 1D PC) that repeats in the *z*-direction with period α, we gradually increase the component materials dielectric index contrast starting from an isotropic, homogeneous dielectric material slab. For a homogeneous dielectric medium, the speed of light is reduced by the index of refraction and the modes lie along the light line, given by Equation (2.9). As shown in Section 2.1, the eigenmodes of such a homogeneous system of constant refractive index are actually freely propagating waves with $\sqrt{\varepsilon}$ reduced speed, compared to c_0, and with their propagation vector conserved; thus, the electric field, $\boldsymbol{E}$, in such a

medium has the form (omitting the time dependence), $\boldsymbol{E}(z)=\boldsymbol{E}_0\cdot e^{ikz}$, where $\boldsymbol{E}_0$ (in V/m) is a constant vector.

Upon introduction of 1D periodicity in the z-direction (1D PC in Fig. 2.1), the Bloch theorem states that the energy eigenstates can be written as Bloch waves that is planewaves [e^{ikz}] multiplied by a periodic function [$\boldsymbol{u}_k(z)$] with the same periodicity (α) as the unit cell of the system due to the coherent scattering by the periodic index of refraction [17]. Such modes, in analogy with the atomic crystals, constitute the electromagnetic modes sustainable by the crystal and can travel through it without scattering (although they will be scattered by defects and impurities). For 1D periodicity along z, $\boldsymbol{u}_k(z)$ can be expressed as Fourier series,

$$\boldsymbol{u}_k(z) = \sum_{-\infty}^{+\infty} \boldsymbol{c}_{m,k} \cdot e^{imk_G z}, \quad (2.10)$$

where the $\boldsymbol{c}$'s are expansion coefficients to be determined by explicit solution, $k_G=2\pi/\alpha$ is the reciprocal lattice vector and m is an integer. From Equation (2.10), there would be modes that differ by the term $\exp(imk_G\cdot z)$ in their wavefunction due to the addition of reciprocal lattice vectors. The Bloch theorem dictates that, due to the discrete translational symmetry along z-axis, such modes are physically identical [17]. As a result, looking at the first Brillouin zone (BZ) ($-\pi/\alpha<k<\pi/\alpha$) [17] in Fig. 2.2(a), and arbitrarily assigning a periodicity of α, effectively folds the dispersion diagram [$\omega(k)$, see Equation (2.9)] of the modes back into the zone when they reach an edge.

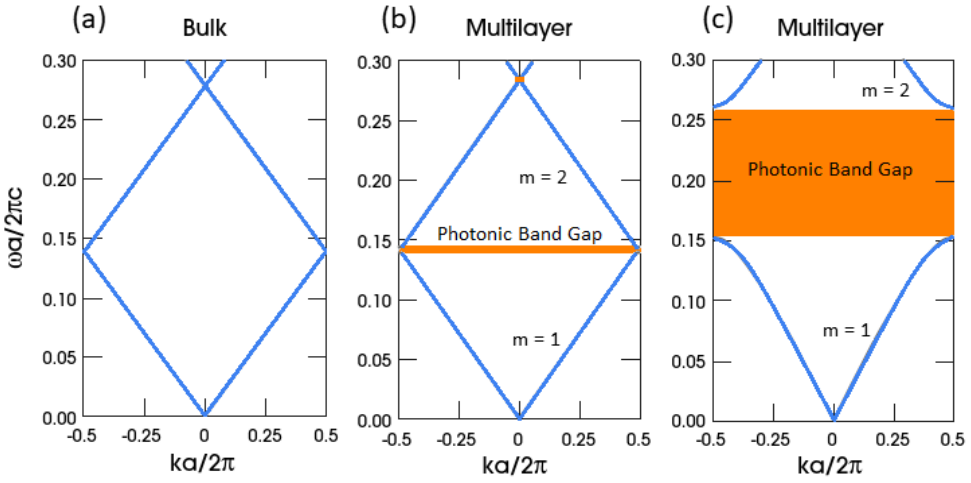

Fig. 2.2: (a) The photonic band structures for on-axis propagation [along z-axis, see 1D PC in Fig. 2.1], for three different multilayer films. In all three cases, each layer has a

width 0.5α. (a) Every layer has the same dielectric constant ε=13, (b) layers alternate between ε of 13 and 12 and (c) layers alternate between ε of 13 and 1. Image adopted from Ref. [17].

The center plot, which is for a nearly-homogeneous medium, looks like the homogeneous case with one important difference: there is a gap in frequency between the upper and lower branches of the lines. There is no allowed mode in the crystal that has a frequency within this gap, regardless of k. We call such a gap a photonic band gap. The right-hand plot shows that the gap widens considerably as the dielectric index contrast is increased. Specifically, for $k = \pi/\alpha$, the modes are standing waves that have a wavelength of 2α, twice the crystal's spatial period. The modes of this type can have the nodes either in each low-ε layer, as in Fig. 2.3(a), or in each high-ε layer, as in Fig. 2.3(b). Any other position would violate the symmetry of the unit cell about its center. It is now clear that the mode just under the gap has more of its energy concentrated in the high-ε regions, as shown in Fig. 2.3(a), giving it a lower frequency than the next band, most of whose energy is in the low-ε regions as shown in Fig. 2.3(b). This difference in frequency that increases with increasing the dielectric index contrast provides the energy gap in the photonic dispersion relation.

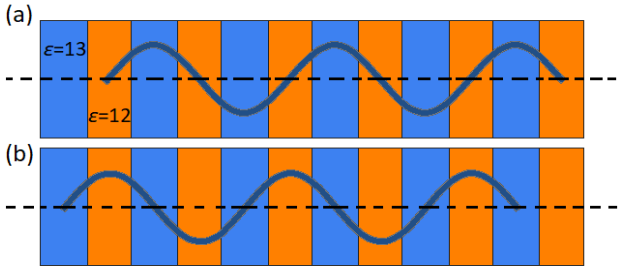

Fig. 2.3: The modes associated with the lowest band gap of the band structure plotted in the center panel of Fig. 2.2(b), at k = π/α. (a) Electric field of band 1; (b) electric field of band 2. Image adopted from Ref. [17].

In several applications, to achieve a high contrast in the refractive index, the use of metallic scatterers, which possess huge values in their dielectric function, is often preferred rather than dielectric ones. However, care must be taken, since metals are very absorptive, especially at optical frequencies, and also there is a strong frequency dispersion in their refractive index, which complicates the presented physical picture of the photonic bandgaps.

We note that omnidirectional reflection is not a general property of 1D PCs, since, for off-axis propagation (along x-, y-axis), there are no periodic dielectric regions to coherently scatter the light and open a gap. However, the

layered dielectric medium can still be designed to reflect external waves that are incident from any angle [18,19].

2.3 GUIDED MODES OF LIGHT

Confining light in space through guided propagation along the desired material could favor solar cell applications due to the enhanced interaction of incident photons with matter hence increasing the absorptivity/emissivity of the device. One of the most well-known phenomena in classical optics that forces light to guided propagation is the total internal reflection (TIR). The familiar description of TIR is that light rays within a high index medium that strike the interface with a lower-index material at too shallow angles are totally reflected.

TIR results from the necessity the parallel to the interface wavevector component, $k_{//}=|\boldsymbol{k}|\sin\theta$ ($|\boldsymbol{k}|=\sqrt{\varepsilon}\,\omega/c_0$) to be identical at both sides of the interface, arising from the continuity of the tangential components of the electric, $\boldsymbol{E}$, and the magnetic, $\boldsymbol{H}$, fields when there are no free surface charges or currents. Assuming a high-index (ε_{slab}) slab of a finite thickness, if $k_{//}$ of the wave that strikes from the high-index medium is higher than the allowed momentum of propagating plane waves at the low-index cladding material ($|k_{clad.}|= \sqrt{\varepsilon_{clad.}}\cdot\omega/c_0$), then the wave is "index-guided" along the in-plane direction (Fig. 2.4) bouncing back and forth between the two interfaces.

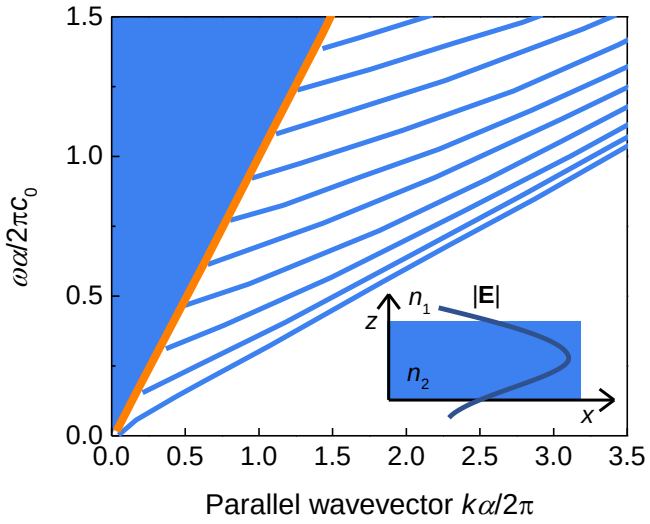

Fig. 2.4: (a) Mode frequencies for a slab of finite thickness and $n_2=\sqrt{\varepsilon_{slab}}$ as shown in the inset (the slab extends much further in the x and y directions than in the z direction). Blue lines correspond to modes that are localized in the slab. The shaded blue region is a

continuum of states that extend into both the glass and the air ($n_1=\sqrt{\varepsilon_{clad.}}$) around it. The orange line corresponds to the light line $\omega=c_0k_{//}$. This plot shows modes of only one polarization, for which H is perpendicular to both the z and k directions. Image adopted from Ref. [17].

To understand the dispersion of the EM modes in such a system, i.e., the frequency ω versus the wavevector $k_{//}$, we first consider the modes that are not confined to the higher-index slab, and extend into the lower-index medium, assuming it is air ($\varepsilon_{clad.}=1$), and out to infinity. Far away from the slab, these modes must closely resemble free-space plane waves with $\omega = c_0|\boldsymbol{k}| = c_0\sqrt{k_{//}^2 + k_{\perp}^2}$ for some perpendicular real wavevector component $k_{\perp}$. For a given value of $k_{//}$, there will be modes with every possible frequency greater than $c_0k_{//}$, because $k_{\perp}$ can take any value. Thus, the spectrum of states is continuous for all frequencies above the *light line* $\omega=c_0k_{//}$, which is marked with an orange line in Fig. 2.4. The region of the band structure with $\omega>c_0k_{//}$ is called the *light cone* (see shaded blue region in Fig. 2.4).

In addition to the light cone, the slab introduces new electromagnetic solutions that lie below the light line (see discrete blue curves in Fig. 2.4). Because ε is larger in the slab than in air, these modes have larger wavevectors relative to modes of the same frequency in free space, falling below the light-line; there, the only solutions in air are those with imaginary $k_{\perp} = \pm i\sqrt{k_{//}^2 + \omega^2/c_0^2}$, corresponding to fields that are confined within the slab and decay exponentially (are evanescent) away from it. We call these the *index-guided modes*, and we expect that for a given $k_{//}$ they form a set of quantized discrete frequencies, because they are localized in one direction [14]. Consequently, we obtain the discrete bands $\omega_m(k_{//})$ below the light line in Fig. 2.4.

Instead of relying on index-guiding there are also other ways to guide light. For instance, defects at the periodicity of the 1D PC, shown in Section 2.2, may permit localized modes to exist, with frequencies inside the photonic band gap. The multilayer films on both sides of the defect behave as 1D PCs with a gap; then if a mode has a frequency in the gap, it must stay confined in the defect and exponentially decay once it enters the PCs [Fig. 2.5(a)].

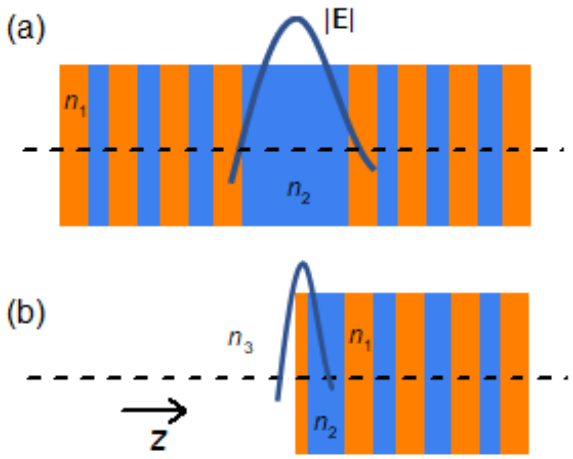

Fig. 2.5: Possible waveguiding structure examples: (a) A defect in a multilayer film, formed by doubling the thickness of a single low-index layer. Note that this can be considered to be an interface between two perfect multilayer films. The curve indicates the electric-field strength of the defect state associated with this structure (for on-axis propagation). (b) The electric field strength associated with a localized mode at the surface of a multilayer film.

Just like in planar waveguides, if we include off-axis wave vectors, any *z*-propagating light of such a frequency will be guided in the "defect waveguide".

Likewise, guided modes can be localized at the surface of a PC instead of a defect region. Previously, the mode was bound because its frequency was within the photonic band gap of the films on both sides. But at the surface, there is a band gap on only one side of the interface. The exterior medium (air, in our case) does not have a band gap. In this case, light is bound to the surface if it is index-guided, a phenomenon discussed earlier, which is a generalization of total internal reflection [Fig. 2.5(b)] [17].

Principally, surface guided waves can exist at any interface, i.e., dielectric-dielectric or metal-dielectric. However, there are surface waves that exist only at metal-dielectric boundaries. One example of this is the Surface Plasmon Polariton (SPP) modes that originate through the sustained coupling of photons with the conduction electrons at the metal surface (see Section 2.4) [20]. SPPs have been investigated for an abundance of applications [21–23] like the recently proposed SPP-based perfect absorbers exploiting the field enhancement at the metallic-dielectric interface [24–26].

Apart from planar 2D SPP guiding (i.e., SPP waves on an infinite planar metal/dielectric interface), many different 3D SPP guiding systems (multiple-interface systems) can be found. For instance, step and gradual index (V-groove), 3D plasmonic-slot-waveguides featuring lateral confinement in the

plane perpendicular to the propagation direction [27]. In such configurations, the lateral confinement can be achieved through an effective index contrast [28].

For the plasmonic-slot-waveguides, it is shown that for shorter wavelengths the mode is confined at the groove bottom, forming Channel Plasmon-Polariton (CPP) modes [29], while as wavelength increases the fundamental CPP mode shifts progressively toward the groove opening. It ceases to be guided at the groove bottom and becomes hybridized with Wedge (tightly confined at the groove edges) Plasmon-Polariton (WPP) modes.

Other important types of SPP interface modes are the plasmonic Surface Lattice Resonances (SLRs) arising from the coupling between the Localized Surface Plasmon Resonances (LSPRs) (see also Section 2.6) of periodically placed metal particles, with enhanced local field due to the high surface charge accumulation, and Rayleigh Anomalies (RAs), that is waves diffracted in the plane of the array [30]. Such diffractive states arise from arrays satisfying the Bragg scattering condition, i.e., the array period α and wavelength λ_0 obey the equation [31]:

$$\alpha\left(\sqrt{\varepsilon} \pm sin\theta\right) = m\lambda_0, \quad (2.11)$$

where ε is the dielectric constant of the optical medium of the incident light, m is the order of the RA and θ is the incident angle. SLR hybrid modes are flexibly tunable and can still have a strong near field enhancement just like the LSPRs, due to the forced resonance arising from the coupling of the scattered in-plane wavevectors with the LSPRs associated with individual particles [32].

2.4 BULK AND SURFACE PLASMON POLARITON

As mentioned in the previous section, SPPs are surface modes arising from the coupling of incident photons with the free charges of a conducting medium. In fact, the incident photons excite and couple to the collective oscillating modes supported by the free charges; such collective oscillations are called plasmons. Plasmons play a large role in the optical properties of metals essentially determining their optical response. For instance, the dispersion of silver's permittivity (ε_{Ag}), as a function of frequency, was calculated by modeling the metal as a free-electron gas (Drude model):

$$\varepsilon(\omega) = \varepsilon_\infty - \frac{\omega_p^2}{\omega^2 + i\omega\gamma}, \quad (2.12)$$

where ε_∞ is the high frequency permittivity of the material corresponding to the background from interband transitions, γ is the collision rate (in rad/s), and $\omega_p=\sqrt{Ne^2/(m^*\varepsilon_0)}$ is the plasma frequency, i.e., the resonant frequency of the free electrons, where $\varepsilon(\omega_p)$ is approximately zero and N, e, m^*, ε_0 are the free electron density, electron charge, effective mass and the permittivity of vacuum, respectively. Equation (2.12), with ε_∞, ω_p and γ obtained from Ref. [33], is plotted in Fig. 2.6(a). Silver's data (circles), obtained from Palik [34], are also drawn for reference. When a plane wave, with a frequency lower than ω_p, is incident upon a metal surface, the free carriers coherently oscillate in a direction opposing the incident EM field. As shown in Fig. 2.6(a), this results to a negative real part of permittivity (shaded area), i.e., the material does not "permit" the incident radiation. Above the plasma frequency, however, the external field oscillates too fast for the free carriers to follow and the metal losses its reflectivity. We note that for silver, the effect of interband transitions becomes clearly noticeable above ~750 THz (< ~0.4 μm) [see circles versus solid lines in Fig. 2.6(a)]. In this case, the Drude model is not sufficient to describe the actual metal permittivity and Lorentzian terms are typically incorporated to model the impact of interband transitions on the permittivity [35].

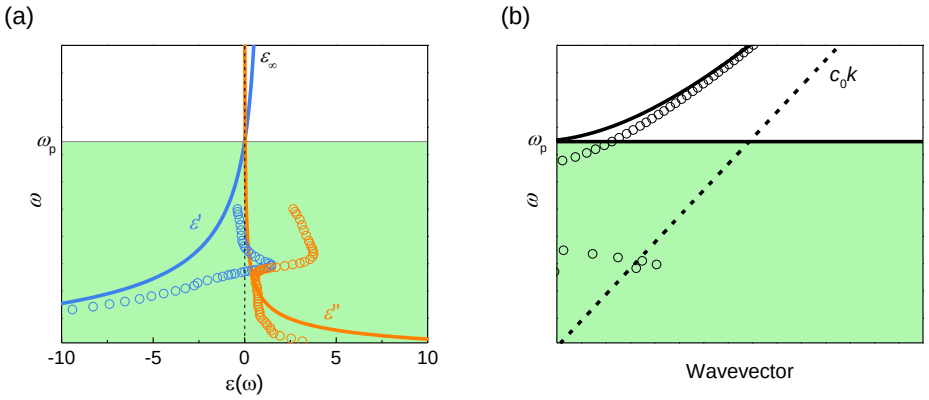

Fig. 2.6: (a) Dielectric function calculated from Equation (2.12) (solid lines) with data from Ref. [33]. *Silver's data (circles), obtained from Palik* [34], *are also drawn for reference. (b) Silver's dispersion curve. The solid lines indicate the bulk plasmon polariton branch and the plasma oscillations (longitudinal volume density fluctuations) at eigenfrequency, ω_p, respectively. The dashed line corresponds to the light line.*

From Equation (2.9), it follows that if an electromagnetic wave is propagating in such a medium, it will have the characteristic dispersion curve

shown in Fig. 2.6(b) (calculated through Equation (2.12) and data from Ref. [33]). This dispersion curve, denotes the interaction of collective oscillations of the free electron gas density with the incident electromagnetic wave. Such coupled states, resulting from coupling between an elementary excitation (plasmon) and a photon are called *polaritons*. Bulk plasmon polaritons [solid line, circles in Fig. 2.6(b)] are associated with purely transverse electromagnetic (TEM) waves, with the electric and magnetic fields perpendicular to the direction of propagation, and can only exist for $\omega>\omega_p$ (above the shaded area) [36]. Substitution of Equation (2.12) in (2.9), assuming no losses and $\varepsilon_\infty=1$, yields $k=\sqrt{(\omega^2-\omega_p^2)}/c_0$. Hence, when $\omega<\omega_p$, the wavenumber becomes imaginary ($k=i\kappa$) and the waveform becomes $e^{-\kappa z}e^{i\omega t}$. Thus, the transverse electromagnetic waves do not propagate and the disturbance damps (see $\omega<\omega_p$ in Fig. 2.6). At the eigenfrequency, ω_p, only longitudinal waves can be supported, i.e., the fundamental mode of the plasma is an oscillation that does not propagate [36].

The situation can be different though at the interfaces, such as, e.g. a metal-dielectric interface. EM radiation can be incident on the interface at an angle. If polarized parallel to the plane of incidence (TM-polarized), the electric field and incident wavevector can be decomposed into two components, parallel and perpendicular to that interface. The parallel wavevector component can then couple to a surface plasmon because it is now a longitudinal wave. Assuming appropriate coupling conditions (same frequency and wave vector of the photon and surface plasmon), a surface wave propagating along the interface is formed called *Surface Plasmon Polariton* (SPP). Such guided waves can exist at the interfaces between conductors and dielectrics and are tightly bound to the interface [see Fig. 2.7(a)].

The SPP mode is an eigenmode of the EM wave equation. In Fig. 2.7(b), the well-known dispersion relation for SPPs guided on planar metal-dielectric interfaces [see Fig. 2.7(a)], is plotted [20]. This relation, k_{SPP} versus ω reads as

$$k_{SPP} = \omega/c_0 \sqrt{\frac{\varepsilon_s \cdot \varepsilon_m(\omega)}{\varepsilon_s + \varepsilon_m(\omega)}}, \quad (2.13)$$

where ε_m is the metal dielectric constant, and ε_s the one of the dielectric (e.g. superstrate).

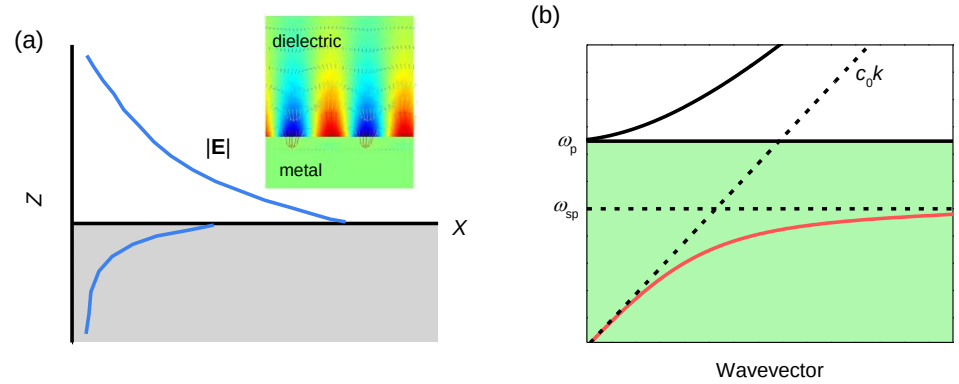

*Fig. 2.7: (a) XZ cross-section, |**E**| of the SPP at the metal (gray)-dielectric interface and the electric field distribution (real part of E_z component) (inset). (b) Plasmon polaritons at metals. The dispersion curves of the uncoupled surface plasmon and photon (light line, $k=\omega/c_0$ assuming air on top of metal) are shown by the dashed lines and those of the bulk (black) and the surface (red) plasmon polaritons by solid lines.*

The dispersion curves of the uncoupled surface plasmons (at eigenfrequency $\omega=\omega_{SP}$, the corresponding limiting frequency of SPPs, which satisfies the requirement: $\varepsilon_m(\omega)+\varepsilon_d=0 \Rightarrow \sim\omega_p/\sqrt{2}$ assuming an air superstrate [see Equation (2.13)]) and photons ($\omega=c_0k$) are indicated by the dashed lines, and those of the surface plasmon polaritons [calculated from Equation (2.13)] by the red solid line. SPPs show a significant dispersion; they can be viewed as hybrid modes, i.e., mainly TEM waves in dielectrics coupled to plasma oscillations in metals, which are primarily longitudinal. In the limit of low ω, the SPP dispersion curve approaches the light line, $\sim(\omega/c_0)\sqrt{\varepsilon_d}$, but remains higher. The associated fields have a more of a light-like behavior, i.e., they are not tightly confined at the interface, but they are nonradiative since the SPP is a guided mode, indicating that appropriate coupling mechanisms are required to outcouple it (see Section 2.5). At large wavevectors, the SPP dispersion curve becomes asymptotic to the surface plasmon frequency, ω_{SP}, which is the frequency of non-propagating collective oscillations of electron plasma near the surface, the surface plasmons [37].

2.5 LEAKY GUIDED MODES

Since the dispersion relation of SPP modes and, in general, guided modes is below the light-line ($\omega<c_0k_{//}$), they are evanescent in the direction perpendicular to the propagation plane (see Section 2.3). Due to their large wavevectors, such modes cannot be excited by the impinging radiation and

appropriate coupling techniques, which provide sufficient momentum, are required. One such technique is to incorporate in the system a periodic lattice.

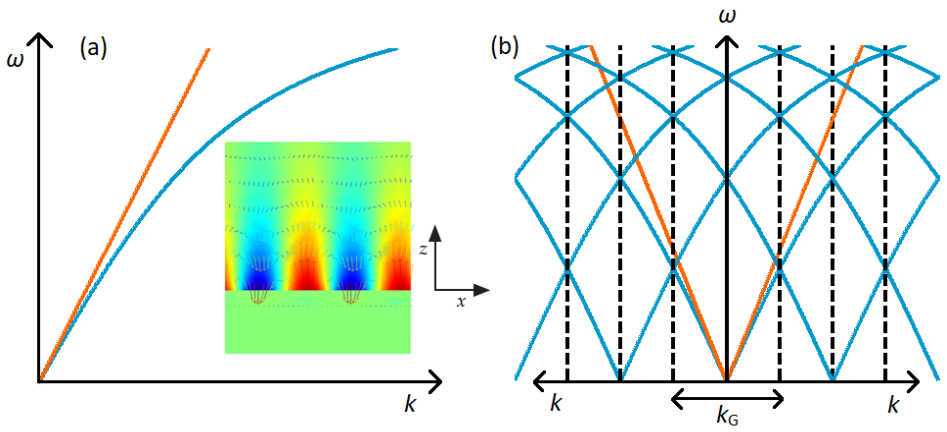

Fig. 2.8: (a) SPP guided mode dispersion relation (blue) and the light line $\omega=c_0k_{//}$ (orange). Inset: xz cross-section of the E_z electric field component of the SPP guided mode propagating in the x-direction on a flat metal-dielectric interface. (b) Periodicity effect on the SPP guided mode dispersion.

As described in Section 2.2, the Bloch theorem dictates that due to the discrete translational symmetry, assigning a periodicity effectively folds the dispersion diagram [$\omega(k)$] of the modes when they reach an edge. For this reason, appropriate crystal lattices can provide the sufficient momentum needed for a guided mode to couple with incident radiation, by effectively folding their dispersion curve into the radiative zone (i.e., inside the light cone, $\omega>c_0k_{//}$). We note that when the coupling of a guided mode with radiation is allowed, the term "guided" no longer strictly applies. However, such modes that can maintain their light-confinement and field-profile properties, sufficiently, are usually called “leaky”- or “quasi”-guided modes or resonances. Examples of realizing waveguiding by providing sufficient momentum are shown in Fig. 2.9.

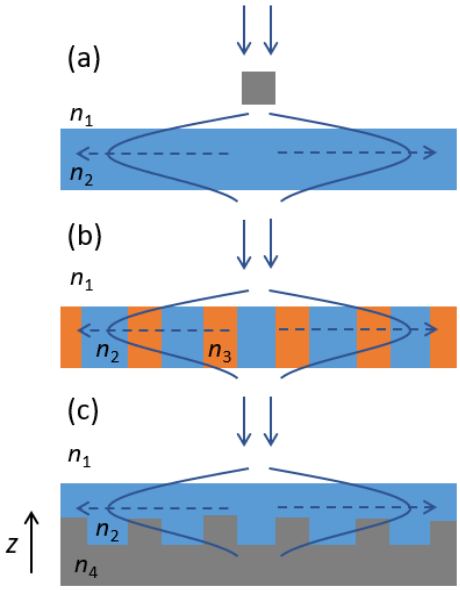

Fig. 2.9: (a) Coupling of incident radiation to guided modes by providing sufficient momentum with (a) single particle and (b), (c) periodic scattering structures.

Among the examples of Fig. 2.9, the latter one [Fig. 2.9(c)], where the planar interface is replaced by a grating, is preferred in solar cell applications to ensure a spatially homogeneous device/performance. Such grating structures [Fig. 2.9(c)], also known as *photonic-crystal slabs*, are not "one- or two-dimensional" photonic crystals, despite the resemblance: the finite thickness in the vertical (z) direction introduces qualitatively new behavior. Although k_z is not conserved, the crystal still has translational symmetry parallel to the surface. Another important advantage of such periodic patterns is that they are much easier to fabricate and can be experimentally realized using standard lithographic techniques for example.

Returning to the SPPs case, in the planar interface limit the SPP wavelength can be calculated from $k_{SPP} = k_{//} + mk_G$, where $k_{//}$ is the parallel component of incident radiation, m is an integer and $k_G=2\pi/\alpha$ is the reciprocal lattice vector due to the introduced lattice with periodicity α. This condition is often called Bragg condition, and employing it the SPPs dispersion relation [see Equation (2.13)] for normal incidence ($k_{//}=0$) leads to $(\omega/c_0)\sqrt{\varepsilon_s\varepsilon_m(\omega)/\left(\varepsilon_s+\varepsilon_m(\omega)\right)} = mk_G$. As shown in Fig. 2.8(b), the introduced periodicity folds the SPP dispersion above the light line and hence radiative coupling of incident light to the SPP may now be achieved. We note though that even if there is no momentum restriction on coupling to radiation, radiative coupling may still be unallowed or inefficient [38].

2.6 LOCALIZED SURFACE PLASMON RESONANCE

In metallic nanoparticles, unlike the SPPs in a flat surface, the closed geometrical boundaries can sustain a localized oscillation (see Fig. 2.10) of the charge density as they generate extra restoring forces up on an EM wave incidence [39]. The resonant coupling of this localized oscillation to the external field is commonly referred to as *Localized Surface Plasmon Resonance* (LSPR).

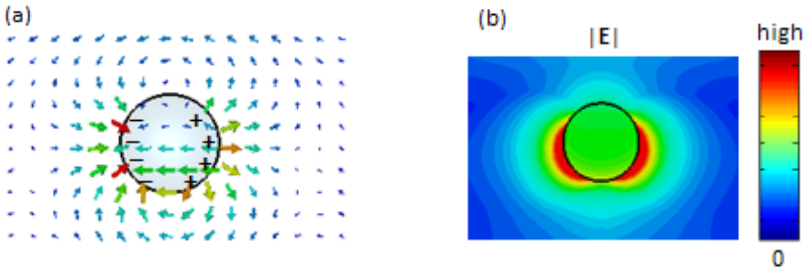

*Fig. 2.10: (a) Electric field and charge distribution (sketch) of a localized surface plasmon resonance (LSPR) excited by an incident plane wave coming from the top. (b) |**E**| field plot.*

The optical response of the LSPRs in a metallic particle can be described through particle's polarizability, α, that relates the incoming electric field, $\boldsymbol{E}_0$, with the induced electric dipole moment $\boldsymbol{p}=\alpha\boldsymbol{E}_0$. Assuming spherical particles with radius, r, smaller than the incoming wavelength, i.e., in the quasi-static approximation, the incoming field can be considered constant and the retardation effects do not play a role. Particle's dipole polarizability in this limit can be approximated by the static polarizability, given by

$$\alpha = 4\pi\varepsilon_0 r^3 \left(\frac{\varepsilon_m - \varepsilon_d}{\varepsilon_m + 2\varepsilon_d}\right), \quad (2.14)$$

Generally, as seen in Equation (2.14), α is a frequency-dependent quantity that depends on the dielectric constant of the metallic sphere, ε_m, and of the surrounding medium, ε_d. The LSPR resonance is associated with a pole of α as a function of frequency, i.e., is obtained by the condition $\mathrm{Re}[\varepsilon_m(\omega)]=-2\varepsilon_d$. Assuming that ε_m is given by Equation (2.12) and the surrounding medium is air, the resonance frequency is obtained as $\omega_{res}=\omega_p/\sqrt{3}$.

An important feature of plasmonic nanoparticles is that they behave as light nano-antennas associated with strong scattering at the LSPRs, and strong

local fields in their vicinity (due to the high surface charge accumulation). For spherical particles with radius smaller than the incoming wavelength, assuming no absorption from the surrounding medium, the scattering, C_{scat}, and the absorption cross-sections, C_{abs}, as a function of polarizability are given by [20,39]

$$C_{scat} = k^4/6\pi\,|\alpha|^2, \quad (2.16)$$
$$C_{abs} = kIm(\alpha), \quad (2.17)$$

where $k=\omega/c_0$ (air host). Hence, (when losses are small) a pole in the polarizability ($\omega_{res}=\omega_p/\sqrt{3}$) implies a maximum in scattering and absorption (see Fig. 2.11).

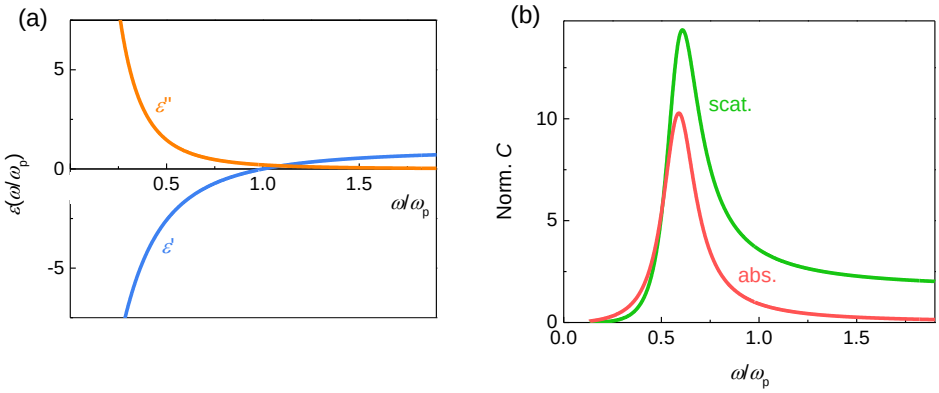

Fig. 2.11: (a) Real ε' and imaginary ε'' of a Drude-like dielectric function as a function of frequency normalized to the plasma frequency ω_p. (b) Normalized scattering and absorption cross-section of a small sphere. A damping of $0.2\omega_p$ has been used in both cases. The resonances are not maximum at the same frequency exactly, but for small damping, both are located close to $\omega_{res}=\omega_p/\sqrt{3}$.

In the case of solar cells, the strong far-field scattering offered by plasmonic nanoparticles can increase the absorption efficiency in thin film solar cells also by exploiting the effect of total internal reflection (see Sections 2.3 and 2.5). This has been already demonstrated in amorphous-silicon-based thin-film solar cells [40], in organic solar cells [41], and in perovskite solar cells [42]. Moreover, the high local fields in the vicinity of plasmonic nanoparticles overlap not only with metal but also with the surrounding absorbing material resulting in increased beneficial absorption, *A*. (This follows directly from Poynting's theorem for power dissipation [14] [$A\sim|\mathbf{E}|^2$].)

Metal spheres of higher radius (or particles of different shape) may support LSPRs of higher-order. By solving the Laplace equation (replacing Helmholtz equation in the quasi-static approximation [14]) and exploiting the

spherical symmetry, with the use of an expansion in spherical harmonics of order *l*, the frequency of the *l*-polar mode is given [for ε_d=1 and ε_m given from Equation (2.12)] by [43]

$$\omega_l = \sqrt{\frac{l}{2l+1}}\omega_p, \quad (2.14)$$

When the size of the particle becomes larger or as the wavelength becomes shorter, quasi-static approximation is insufficient to approximate the solution. Then one has to solve the full-wave EM problem, usually using Mie theory, including both electric and magnetic modes [44].

3

PASSIVE RADIATIVE COOLING

3.1 INTRODUCTION

Passive (i.e., no extra energy input needed) radiative cooling (PRC) is an appealing approach to radiatively dissipate waste heat from a terrestrial surface to outer space. This is possible since the thermal radiation of earth objects, with typical temperatures of ~300 K, overlaps with the atmospheric transparency window (8–13 μm) (see Fig. 3.1).

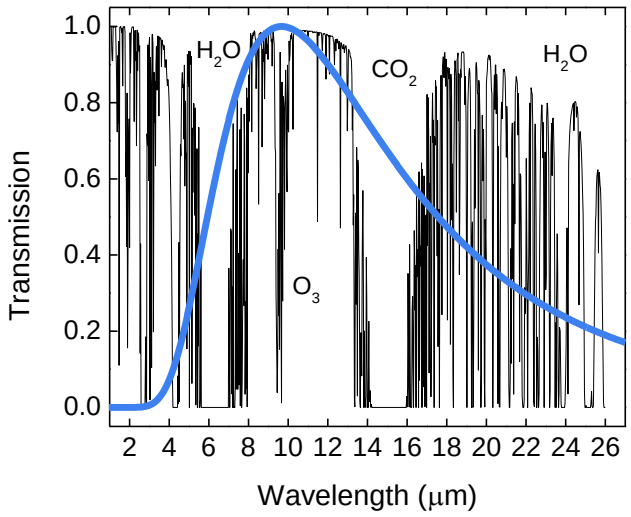

Fig. 3.1: Thermal wavelengths (~ >3 μm). Infrared transmission of the atmosphere (black line), normalized blackbody spectrum for 300 K (blue line) from 1-27 microns [45] *and the absorption bands (range of electromagnetic radiation that had been absorbed by an atom or molecule).*

Therefore, a device facing the sky has radiative access to the coldness of the universe, through this atmospheric transparency window, and therefore can

use the universe as a heat sink, with much lower temperature (~3 K) than that of the atmosphere (~300 K). During nighttime, earth objects could potentially reduce their temperatures much below the ambient temperature. Their cooling power could be limited by the blackbody radiation limit [46], the non-radiative heat transfer (e.g., through convection) and the weather conditions (clouds, humidity, etc.) [47]. The significance of radiative cooling and its potential applications were already emphasized a few decades ago and practical cooling during the nighttime operation was also demonstrated [48,49]. Bulk materials comprising mid-IR emissions at the thermal wavelengths (~ >4 μm, see Fig. 3.1) (see also Section 3.3) lowered device's temperature below ambient. Daytime cooling though below the ambient temperature was not achieved at that time, as the absorbed solar energy exceeded the emitted energy by thermal radiation.

Recent advances on daytime radiative cooling have revived the interest in this field. Sub-ambient radiative cooling of objects during daytime under direct sunlight has recently been achieved by utilizing nanophotonic coatings [50,51]. Raman et al. [51] in 2014 developed a passive radiative cooling system based on a photonic crystal. The photonic crystal was designed to reflect the solar heating power (~0.28–4 μm) and at the same time allow radiative cooling through thermal emission in the mid-IR, at the atmospheric transparency window of 8–13 μm. With this approach Raman et al. [51] demonstrated an impressive cooling, up to 5 K below ambient under direct sunlight, where the photonic crystal had a cooling power of 40.1 W/m^2 at ambient air temperature. Subsequently, appropriate passive radiative coolers, like multilayer thin film stacks [51], 2D photonic crystals [15] etc. as coating structures were designed, offering substantial cooling that could potentially reduce energy consumption significantly, for various applications.

Compared to nighttime, daytime radiative cooling is much more appreciated since it matches better with end-user's peak cooling load, in the case of cooling buildings for example [52]. More specifically, ~12% of building energy consumption in the US is for space cooling [53]. Building radiative cooling can be employed either in a passive way (with no energy input), having the advantage of simplicity and economy, or in a more active way, i.e., in conjunction with air- or water-based systems. Conventional passive systems utilizing regular roofing materials such as black or white shingle and paints [54] exhibit low solar reflectance though. Active systems such as cooling of a heat transfer fluid require a small percentage of energy input for pumping but their cooling power can be more easily regulated. Other applications that could benefit from daytime radiative cooling are photovoltaic (PV) applications. PVs operating under the sun inevitably generate heat, apart

from electrical power, easily exceeding 325 K on a sunny summer day; this has significant adverse consequences both for their performance [10] and lifetime [9]. A photovoltaic, by necessity, faces the sky. Therefore, it is of great importance to examine whether daytime radiative cooling could be incorporated in photovoltaic systems and the effects of such a cooling approach in the PV performance.

In the present chapter, we describe the principles of passive radiative cooling and we examine and discuss the requirements for cooling radiatively solar cells (Section 3.2). We further examine when a material can be considered as a radiative cooler (Section 3.3).

3.2 PASSIVE RADIATIVE COOLING PRINCIPLES AND REQUIREMENTS

When a structure (a cooler in our case) is exposed to a daylight sky, it is subject to both solar irradiance over solar wavelengths (~0.28-4 μm) [see Fig. 3.2(a)] and atmospheric thermal radiation (corresponding to ambient air temperature) [see Fig. 3.2(b)].

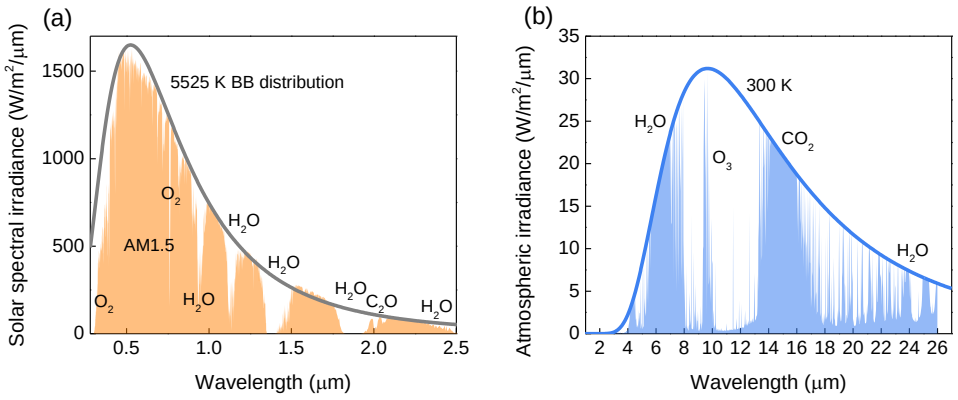

Fig. 3.2: (a)) A reference AM 1.5 solar irradiance spectra (air mass (AM) 1.5 [55]*) and a distribution of a 5525 K blackbody. (b) Atmospheric irradiance at an ambient temperature of 300 K and a 300 K blackbody for reference.*

Along with the effect of the incoming radiation, the cooling performance of such a structure/cooler depends on other factors too, such as, the nonradiative (conductive and convective) heat gain from the surrounding media and the thermal radiation emission profile. The net cooling power, $P_{net,cool}$, of the structure can thus be determined by summing the total power into and out of the device:

$$P_{net,cool}(T, T_{amb}) = P_{rad,cooler}(T) - P_{atm}(T_{amb}) + P_{cond,conv}(T, T_{amb}) - P_{solar,heat}, \quad (3.1)$$

In Equation (3.1), $P_{\mathrm{rad,cooler}}$ is the power density (in W/m^2) radiated from a surface, in our case from the surface of the cooler (mainly in the mid-IR, offering cooling to the device), P_{atm} is the power density absorbed from the atmospheric emission, $P_{\mathrm{cond,conv}}(T,T_{\mathrm{amb}})=h_{\mathrm{c}}(T-T_{\mathrm{amb}})$ [51] is the power density related to the nonradiative heat transfer, where T_{amb} is the ambient temperature and $h_{\mathrm{c}} = h_{\mathrm{cond}} + h_{\mathrm{conv}}$ is a combined nonradiative heat transfer coefficient that captures the collective effect of conductive and convective heating owing to the contact of the cooler with external surfaces and the air adjacent to its top surface. $P_{\mathrm{solar,heat}}$ is the absorbed solar power density that dissipates into heat.

Since the work of Kirchhoff (1860), Wien (1896), and in particular Planck (1906) thermal radiation is well accounted for [46]. The radiation emitted through a perfect thermal emitter into a hemisphere is black-body radiation and its spectral irradiance at temperature T is

$$\varphi_{BB}(\lambda, T) = \left(\frac{2hc^2}{\lambda^5}\right) \cdot \frac{1}{e^{hc/\lambda k_B T} - 1}, \quad (3.2)$$

where h is Planck's constant, k_{B} is Boltzmann's constant, c is the speed of light. With Kirchhoff's law this expression may be extended to the emission of thermal radiation from non-black bodies in terms of the absorptivity, $\alpha(\lambda)<1$, assuming no dependence of the absorptivity on temperature:

$$\varphi(\lambda, \theta, T) = a(\lambda, \theta) \cdot \varphi_{BB}(\lambda, T), \quad (3.3)$$

Hence, the power density radiated from the surface of the cooler is given by

$$P_{rad,cooler}(T) = \int d\Omega cos\theta \int_0^{\infty} \varphi_{BB}(\lambda, T)\varepsilon(\lambda, \theta)d\lambda, \quad (3.4)$$

Here, $\int d\Omega = \int_0^{\pi/2} d\theta \sin\theta \int_0^{2\pi} d\varphi$ is the angular integral over a hemisphere, and by using Kirchhoff's radiation law we replace the structure's spectral-directional absorptivity $\alpha(\lambda,\theta)$ by its spectral-directional emissivity $\varepsilon(\lambda,\theta)$ [56]. The emissivity is the most important parameter in Equation (3.4), and it is assumed independent of temperature because its variation in the temperature range of radiative cooling applications is negligible. Therefore, $\varepsilon(\lambda,\theta)$ has only

a spectral and angular dependence. To specify radiator's capability, the integrated average emissivity in the range $8<\lambda<13$ μm is often examined. The total hemispherical emissivity $\bar{\varepsilon}$ is also used, defined as the total energy emitted from a surface over all wavelengths and in all directions (for most materials the emissivity remains relatively stable and high for polar angles ~0-60°):

$$\bar{\varepsilon} = \frac{\int d\Omega cos\theta \int_0^\infty \varphi_{BB}(\lambda,T)\varepsilon(\lambda,\theta)d\lambda}{A\sigma T^4}, \quad (3.5)$$

where σ is the Stefan–Boltzmann constant, and A is the view factor (~1 for terrestrial, i.e., no tilting, solar modules). Based on the total hemispherical emissivity, Equation (3.4) can be rewritten as the Stefan–Boltzmann law:

$$P_{rad,cooler}(T) = \bar{\varepsilon}A\sigma T^4, \quad (3.6)$$

The absorbed by the cooler thermal radiation emitted from the atmosphere at ambient temperature (T_{amb}) is given by [15,51]

$$P_{atm}(T_{amb}) = \int d\Omega cos\theta \int_0^\infty \varphi_{BB}(\lambda,T_{amb})\varepsilon(\lambda,\theta)\varepsilon_{atm}(\lambda,\theta)d\lambda, \quad (3.7)$$

where $\varepsilon_{atm}(\lambda,\theta) = 1 - t(\lambda)^{1/cos\theta}$ is the angle-dependent emissivity of the atmosphere that incorporates the atmospheric transmittance [$t(\lambda)$ is the atmospheric transmittance in the zenith direction]. The last term in Equation (3.1), $P_{solar,heat}$, is given by [15,51]

$$P_{solar,heat} = \int_0^\infty \varepsilon(\lambda,\theta_{sun})\varphi_{AM1.5G}(\lambda)cos\theta_{sun}d\lambda, \quad (3.8)$$

where the solar illumination is represented by the measured sun's radiation $\varphi_{AM1.5G}(\lambda)$, the AM1.5 spectrum [55], and $\varepsilon(\lambda,\theta_{sun})$ is the cooler's absorptivity/emissivity. In Equation (3.8) we assume that the structure is facing the sun at a fixed angle θ_{sun}. Thus, the term $P_{solar,heat}$ does not have an angular integral, and the cooler's absorptivity/emissivity $\varepsilon(\lambda,\theta_{sun})$ is represented by its value at θ_{sun}.

Equation (3.1), in general, relates the cooling power of the cooler's surface, that is, the net power outflow of the surface, to its temperature. If there is a net positive power outflow at $T=T_{amb}$ under direct sunlight, that is, if the thermal emission rate is higher than the absorption rate, such a surface

becomes a daytime cooling device. In the absence of net outflow, a radiative cooler's temperature should reach a steady-state temperature below ambient. The solution of Equation (3.1) with $P_{net,cool}(T,T_{amb})=0$ defines the steady-state temperature T.

In practice, to achieve meaningful daytime radiative cooling, below ambient temperature, more than 94% of sunlight must be reflected, especially given the variation in atmospheric conditions across different geographic regions [51]. The parasitic heat due to convection and conduction should also be reduced. Additionally, the device must emit selectively and strongly only at 8-13 μm, where the atmosphere is transparent, and must reflect at all other wavelengths. These constraints are fundamentally thermodynamic in nature, meaning that the incoming non-radiative/radiative power rates that tend to achieve a steady-state thermodynamic non-equilibrium at higher temperatures than ambient, must be reduced.

The application of radiative cooling at PVs alters the above-mentioned requirements significantly. Here, the radiative cooler should be transparent at the beneficial solar wavelengths for the incident radiation to reach the cell, where the conversion of sun light to electricity takes place (see Fig. 3.3).

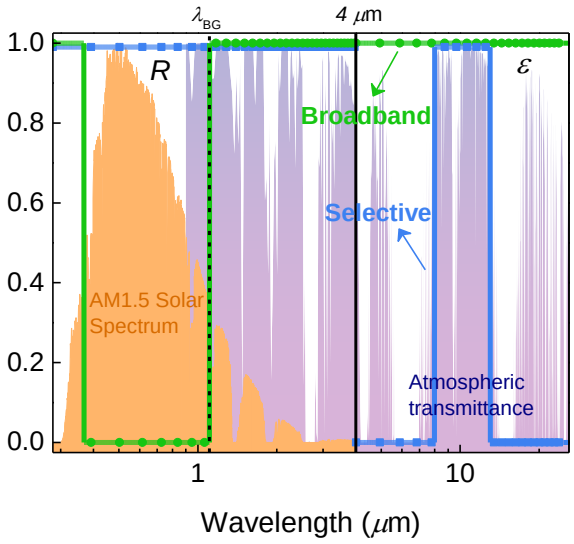

Fig. 3.3: Optimum reflectivity (R), at 0.28–4 μm, and emissivity (ε), at >4 μm, spectra (point-solid lines) for sub- (blue) and above-ambient (green) radiative cooling, together with the AM 1.5 solar irradiance spectra (orange shaded area – air mass (AM) 1.5 [55]*) and the infrared transmission of the atmosphere (blue shaded area)* [45]*. The green line corresponds to above-ambient radiative cooling in case of commercial silicon-based photovoltaics with a bandgap of λ_{BG}~1.107 μm.*

Moreover, a PV, unavoidably, has an increased thermal load. As it was explained by Shockley and Queisser in their seminal paper [57] in 1961 (see also Chapter 4), the highest fraction of the absorbed sunlight to be converted to electrical power remains unexploited. For a single-junction solar cell, the theoretical upper limit for incident solar to electrical power conversion efficiency is around 33% (assuming that it operates at a constant temperature equal to 300 K). In practice, the residual power dissipates mainly into heat [58,59], at the various parts of the PV, highly exceeding the 6% of sun's absorbed radiation that is vital for achieving meaningful daytime radiative cooling. In the absence of net outflow ($P_{net,cool}$=0), a PV's radiative cooler should reach a steady-state temperature much higher than ambient temperature. Such a structure cannot become a daytime radiative cooling device as defined in Ref. [51]. However, a net positive power outflow could be achieved at lower temperature if one enhances the thermal radiation emission and reflects the PV detrimental solar spectral regimes. Since for PVs $T>T_{amb}$, to further enhance radiative cooling, the structure's emission spectrum should also be broadband (>4 μm) and not selective (8-13 μm) (see green line at >4 μm in Fig. 3.3). In this way, a PV (T~325 K) can additionally exhibit significant radiative heat transfer to the atmosphere of lower temperature (T_{amb}~300 K).

Owing to the differences of application requirements and ideal absorptivity/emissivity spectra, the radiative coolers can be classified into three major types: (i) those designed for sub-ambient nighttime cooling, i.e., mainly comprise selective mid-IR emissions at 8–13 μm (the atmospheric window), (ii) radiators designed for sub-ambient daytime cooling i.e., highly efficient sunlight reflectors (see blue line in Fig. 3.3). Such coolers may be utilized for cooling buildings for example. (iii) Coolers operating above ambient temperature, designed purely for heat dissipation; i.e., broadband (~>4 μm) thermal radiators, mostly solar transparent, e.g., for cooling PVs (see green line in Fig. 3.3).

3.3 POLAR MATERIALS' BULK AND SURFACE PHONON POLARITONS

In reality, there is no body that produces no emission. However, for significant radiative cooling, the emission rate inside the atmospheric transparency window (8-13 μm) should be high enough. This is possible even with bulk (i.e., not structured) materials, acting as radiative coolers, such as polar dielectrics. In polar crystal media, an applied EM field can excite and couple

with strong transverse lattice vibrations (transverse optical phonons) resonant in the far- to mid-infrared, the so-called phonon-polariton excitations. This coupling results to strongly mixed vibrational/electromagnetic modes known as phonon-polariton modes, which propagate through the medium increasing the emissivity of the material. The large dipole moments, though, associated with the strong lattice vibrations, also result in the typically large splitting between longitudinal and transverse optical (LO and TO, respectively) phonon resonance frequencies, as a result of the long-range nature of the Coulomb interactions, i.e., charged particles [60], where electromagnetic propagation is forbidden, known as the *polariton gaps*, decreasing the emissivity [15].

The choice thus of a bulk homogeneous material as a radiative cooler depends on its emissivity profile associated to the coupling strength between the incident mid-IR photons with transverse lattice vibrations. There are also practical limitations, i.e., resistance to the outside conditions, optical properties, cost, etc. Silica, in particular, which is the main material employed in the current work has been extensively employed in passive radiative cooling applications. In its bulk form, it acts as a fairly acceptable broadband radiative cooler material due to its bulk phonon-polariton resonance, which also overlaps with the atmospheric transparency window (8-13 μm), and high mid-to-far-infrared absorption, resulting to a hemispherical emissivity estimated to be around ~0.73 [61]. It is also utilized in the case of PVs in the form of tempered glass (contains 70−80% silica and other additives, created by thermal or chemical means), acting as a transparent top surface that protects the bare cell and offers rigidity, providing also access to radiative cooling.

Utilizing conservation laws of energy and momentum, one can predict the resonance frequency of the phononic vibrational modes of a material in a Raman scattering experiment [62]. This resonance should also appear in the extinction spectrum. In addition to experimentally, the study of such media has also attracted great attention theoretically, due to the unique and well-understood frequency-dependent dielectric function. For fused silica, in the mid-IR (< ~11 μm), the coupling of the modes can be well-described by means of a single Lorentzian oscillator model that corresponds to the real system of the Si-O-Si antisymmetric stretching vibration, that is silica's strongest stretching vibration, with the TO phonon resonance frequency $\omega_{TO}=2.004\cdot10^{14}$ rad/s and oscillator strength $\Delta\varepsilon=0.663$ (proportional to the vibrational dipole moment and related to the TO-LO splitting) [63]. Through ω_{TO} and $\Delta\varepsilon$, the silica frequency dependent dielectric function can be written as

$$\varepsilon(\omega) = \varepsilon_\infty + \frac{\Delta\varepsilon\omega_{TO}^2}{\omega_{TO}^2 - \omega^2 - i\omega\Gamma}, \quad (3.7)$$

where ε_∞ denotes the asymptotic value of the dielectric function at very high frequencies (i.e., $\omega >> \omega_{LO}$). The magnitude of the losses is represented by Γ, the phonon damping. When damping is ignored, the dielectric response function has poles at ω_{TO} and zeros at ω_{LO}, the frequency of the LO phonon in the bulk [62]. The latter condition [$\varepsilon(\omega)=0$] gives the Lyddane-Sachs-Teller (LST) relation, $\omega_{LO}^2/\omega_{TO}^2=\varepsilon_0/\varepsilon_\infty$, where ε_0 is the low-frequency dielectric constant and $\Delta\varepsilon=\varepsilon_0-\varepsilon_\infty$. From LST, when $\varepsilon_0=\varepsilon_\infty$ the LO and TO modes are degenerate and we have no resonance ($\Delta\varepsilon=0$). This is the case of non-polar crystals. The maximum of the imaginary part of the negative inverse dielectric function, $\Im(-1/\varepsilon)$, or the energy-loss function, defines ω_{LO} [62].

Figure 3.4(a) shows the real and the imaginary part of fused-silica's permittivity (ε_{SiO_2}) as a function of frequency (in THz), calculated from Equation (3.7) (solid lines), with $\omega_{TO}=2.004\cdot10^{14}$ rad/s, $\Delta\varepsilon=0.663$, and $\Gamma=1.413\cdot10^{13}$ rad/s [63]. Corresponding experimental data (circles), obtained from Palik [34], are also drawn for reference, verifying very good agreement. To better understand Fig. 3.4(a), silica's characteristic phonon–polariton dispersion properties are plotted in Fig. 3.4(b). The dispersion curves of the uncoupled phonons (at $\omega=\omega_{TO}$) and photons ($\omega=c_0k/\sqrt{\varepsilon_\infty}$) are indicated by the dashed lines, and of the LO phonons [$\omega=\omega_{LO}$, $\varepsilon(\omega)=0$] and the polaritons (calculated from $\omega=c_0k/\sqrt{\varepsilon_{SiO_2}}$, see Chapter 2.1) by solid lines.

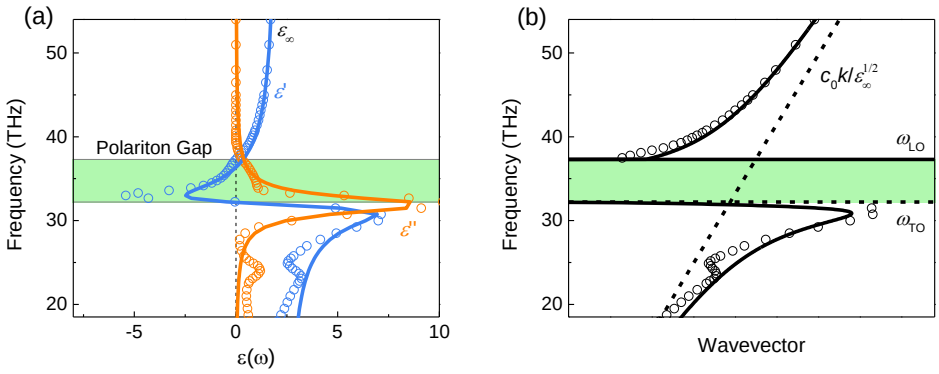

Fig. 3.4: a) Polariton dielectric function calculated from Equation (3.7) (solid lines) with data from Ref. [63]*. Fused-silica's infrared data (circles), obtained from Palik* [34]*, are also drawn for reference. b) Phonon–polariton dispersion curve. The solid lines indicate the upper and lower polariton branches and the LO phonon. The dashed lines describe the optical dispersion at high frequencies and the uncoupled phonons, respectively. The lower branch is primarily electromagnetic in character at low wavevectors, and primarily*

mechanical at high wave vectors. We also observe the LO–TO split [60] *that arises from long-range transverse electromagnetic fields driving longitudinal vibrations.*

Polaritons show a significant dispersion, i.e., there is a significant admixture of electric field and mechanical displacement in the mode, due to the strong coupling of the, transverse in nature, light with the transverse optical phonons [62]. As a consequence of the strongly coupled TO-phonon-photon mode, the degeneracy is lifted resulting to the LO-TO splitting or silica's characteristic gap at ~32.2–37.3 THz. This region is also known as the Reststrahlen band. In this spectral regime, the dielectric function has negative values [see blue line in Fig. 3.4(a)], i.e., the material does not "permit" the EM radiation, but it rather reflects it. In relation to metals (see Chapter 2.4), this reflectivity is connected to the coherent oscillations of the vibrating bound charges. In particular, as seen in Fig. 3.4(a), silica is a fairly acceptable broadband radiative cooler material due to its bulk phonon-polariton resonance, which results to high absorption at the thermal wavelengths [see orange line in Fig. 3.4(a)]. However, the polariton gap overlaps with the atmospheric transparency window (~37.5-23.1 THz or ~8-13 μm) increasing its reflectivity in that regime [see blue line in Fig. 3.4(a)] and lowering significantly its performance.

The infrared reflection spectra of a fused silica (data from Palik [34]) slab obtained by unpolarized incident light at different angles of incidence, θ, together with the atmospheric transparency window, are shown in Fig. 3.5.

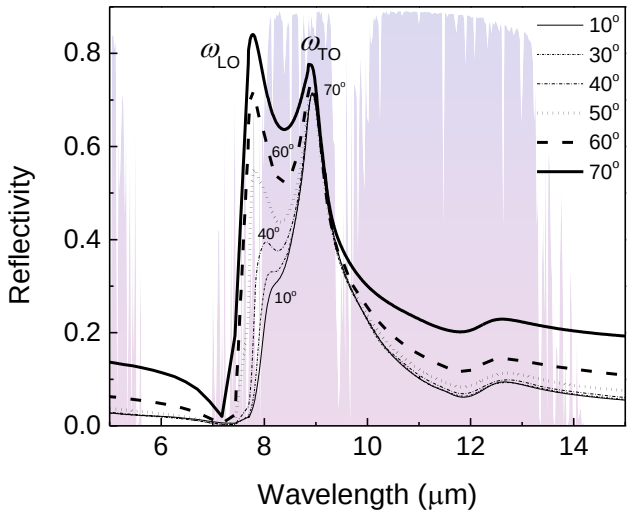

Fig. 3.5: Infrared transmission of the atmosphere (shaded area) and reflection spectra of a fused silica glass slab (lines). The data obtained from Palik [34] *for silica slab of semi-infinite thickness at different angles of incidence by means of unpolarized incident light.*

ω_{LO} and ω_{TO} denote the frequencies of the transverse and longitudinal phononic modes, respectively.

The reflection band near 9.3 μm is referred to as the main TO mode in the infrared range [63]. At near-normal incidence, the electric field vector is near-parallel to the sample surface. In this case, only a small part of the LO mode is excited as a result of its longitudinal nature [64]. At oblique incident radiation both TO and LO phonons are excited. These reflectivity peaks coincide with the transparency window of the atmosphere (shaded area in Fig. 3.5), and hence reduce silica's cooling capability. Therefore, eliminating them is of high importance.

Comparing Equation (2.12) (Fig. 2.6) and Equation (3.7) (Fig. 3.4), one can see that the optical response function, $\varepsilon(\omega)$, for plasmon polaritons is the same with that of phonon polaritons in the limit $\omega_{TO}=0$, where $\omega_p=\omega_{LO}$ (i.e., considering a simple case of no restoring force [33]). Therefore, polaritonic materials, for frequencies between ω_{TO} and ω_{LO}, exhibit optical properties similar to those of metals below the plasma frequency, without free carriers, like high reflectivity, but with reduced damping rates and vastly different electronic properties [65]. Similar to SPPs, *Surface Phonon Polaritons* (SPhPs) are collective excitations of the dipoles on the polar material surface coupled with the electromagnetic radiation [66]. Their dispersion relation [see Equation (2.13)] can only be satisfied in the Reststrahlen band (within $\omega_{TO}\leq\omega<\omega_{LO}$) because the dielectric function of a polar dielectric crystal is negative in this region (see Fig. 3.6).

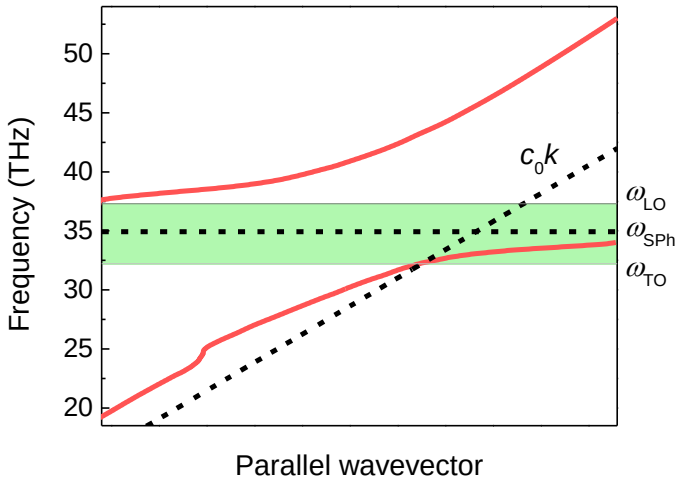

Fig. 3.6: Surface phonon polariton at polar media. The dispersion curves of the uncoupled surface phonon and photon (air light-line: $\omega=c_0k$) are shown by the dashed lines and of the surface phonon polariton by the red solid line within $\omega_{TO}\leq\omega<\omega_{LO}$.

Such states that exist within polar-materials' polariton gap are associated with high local field values and thus seem promising for enhancing their cooling capability. By ruling a grating on the surface of the polar material, the localized SPhP modes can be coupled to propagative waves in the far-field, hence enhancing the thermal radiation emission. We note also that polar particles, like polar spheres, may support localized surface resonances, equivalent to LSPRs, known as Frohlich resonances [67]. These surface phonon modes appear in a sphere with a radius smaller than the wavelength of the electromagnetic radiation. They are vibrational modes that have an homogeneous polarization throughout the spherical volume and a frequency, between the longitudinal ω_{LO} and transverse ω_{TO} resonance frequencies; such as $\mathrm{Re}[\varepsilon_m(\omega)]=-2\varepsilon_s$ (see also Section 2.6). Polar spheres of higher radius may support Frohlich resonances of higher-order, including both electric and magnetic modes [68].

Aside from silica, the IR absorption bands of numerous materials have been found to match the atmospheric window. A classification of those materials as radiative coolers in the scheme described in the last paragraph of Section 3.2, is not straightforward though. Their radiative properties (absorption, reflection, transmission) may be controlled by their size or design. Moreover, materials utilized for daytime radiative cooling may often utilized for nighttime radiative cooling successfully. In general, radiative cooling materials that have been investigated as candidates for nighttime radiative coolers mainly comprise selective mid-IR emitters, within the atmospheric window (~8-13 μm), and can be categorized into the following groups [69,70]: (i) polymer-based [Polyvinyl chloride (PVC), polyvinyl fluoride (PVF), polymethyl pentene (TPX), polymethyl methacrylate (PMMA), modified polyphenylene (PPO) resin], (ii) oxides [silicon monoxide (SiO), silicon dioxide (SiO_2), magnesium oxide (MgO)], (iii) nitrides [silicon nitride (Si_3N_4), silicon oxynitride (SiO_xN_y)], or even (iv) gas slabs [ammonia (NH_3), ethylene (C_2H_4), ethylene oxide (C_2H_4O)]. During nighttime, temperature reductions even higher than ~15 K below ambient were reported, that were also enhanced (up to ~2 K) compared to a blackbody cooler [48].

Daytime radiative cooling materials are primarily oxides and carbonates of titanium, aluminum, calcium, and zinc, due to their high reflectivity in the solar spectrum. Materials that could be employed effectively in photonic radiative cooler designs, e.g., photonic crystals, for operation during daytime at both above- and below-ambient temperatures are those with very low or no

solar absorption, like polymers [polydimethylsiloxane (PDMS), PMMA], oxides [SiO_2, aluminum oxide (Al_2O_3), zinc oxide (ZnO), titanium dioxide (TiO_2), hafnium dioxide (HfO_2)], nitrides [silicon nitrides (Si_3N_4, SiN)], ceramic materials [lithium fluoride (LiF)] or other inorganic thin-films [SiO, silicon carbide (SiC), magnesium fluoride (MgF_2)]. In particular, for daytime operation above ambient temperature, glasses such as Silica, Quartz or low iron Soda-lime silica (window glass) are often utilized [15,71–74], mainly, because of their ability to act as optically transparent and fairly acceptable blackbody-like thermal radiators, offering simplicity and reliability compared for example to the highly-efficient polymer, i.e., PDMS, radiative coolers [75–78]. We note that in cases where sunlight optical transmission should be blocked the transparent radiative cooling materials are usually placed on top of silver or aluminum substrates which do not add significant unwanted absorption in the visible or outside the atmospheric window.

Composite material coolers consisting of two or more different materials, as an alternative to bulk and gaseous material radiative coolers, were also reported. For instance, it was found that the two IR absorption bands of SiO_2 and SiC nanoparticles match the atmospheric window and are complementary to each other [50,79]. When SiO_2, SiC nanoparticles are mixed in a polyethylene (PE) binder, a 25 K temperature drop below ambient can be achieved if there is limited non-radiative heat transfer and no sunlight [79]. Moreover, paints based on a polymeric binder with various pigments [TiO_2, zinc sulfide (ZnS)] [80,81] or carbon-based nanomaterials in an acrylate (AC) emulsion [82] are some examples of above-ambient radiative coolers with composite materials. Appropriate polymeric binders are PVF, PE, PVDF, PMMA and especially TPX due to its excellent solar transmittance.

Even though the energy benefits from daytime radiative cooling are obvious, there are many important challenges such as reliability, manufacturing scalability and cost. Apparently, manufacturing scalability is an important factor for which polymers and paints show advantages [68,77]. However, a polymer's degradation reduces a cooler’s reliability. Ultraviolet (UV) radiation, specifically, is a critical degradation factor. A common approach for blocking UV light is employing UV absorbers, having though finite lifetimes and resulting also in significant heat dissipation at ~0.3–0.4 μm that is disadvantageous, especially for below-ambient radiative cooling. Glasses as alternatives increase cooler’s reliability. Additionally, their high transparency in the optical regime is vital for effectively adding radiative cooling in the case of solar energy harvesting applications (solar cells, thermophotovoltaics, etc.). However, just like polymers, in applications where optical reflection is required, they are often placed on top of metallic

substrates, which are prone to oxidation by oxygen and moisture. Moreover, the solar absorption at wavelengths 0.3–0.4 μm is still high due to the absorption in metal (e.g. for silver reflectors). A way to avoid the metal layers and at the same time to strongly reflect sunlight, including UV radiation, has been proposed recently [77,83]. Through a phase inversion method, a porose poly(vinylidene fluoride-co-hexafluoropropene) [P(VdF-HFP)] coating was prepared with light-scattering pores on the micro- and nanoscale [83]. Cooler's reliability though related to dust or moisture should be examined. Alternatively, our proposed UV reflector described in Ref. [84] is a one-dimensional multilayer film stack that is relatively simple in fabrication, composed of common non-absorbing materials in the optical regime that are already widely utilized, i.e., in the solar cell industry, offering reliability.

4

COUPLED OPTO-ELECTRO-THERMAL MODEL FOR PHOTOVOLTAICS

4.1 INTRODUCTION

Increased heating in photovoltaic devices has significant adverse consequences on both their efficiency and life-time. Daytime radiative cooling may provide an alternative to the common approaches to dissipate waste heat, and thus achieve temperature reduction in PVs [15,16,72,85–87], having the important advantage that it is passive, i.e., no input energy is required for its operation. Most of the existing studies examining radiative cooling in PVs, though, treat them as solar absorbers and not as quantum devices, i.e., they do not consider the effect of the electrical power generation [15,16,72,85]. In particular, most present studies take advantage of the well-known linear temperature-PV-yield relation to calculate the output power change as a function of the operating temperature change. Optimizing radiative cooling in PVs though, unavoidably results in changes in the optical response of the system; for example, a radiative cooler placed at the top surface of a PV may affect the system transparency at solar wavelengths considerably and, hence, the efficiency. Consequently, the critical interplay between the requirements for transparency in the optical spectrum (0.28-4 μm) and the enhanced, broadband thermal emission in mid-IR cannot be weighed.

The few existing studies treating PVs as quantum devices [86,87], in their radiative cooling examination do not incorporate all the major temperature-dependent recombination mechanisms of the photon-generated carriers that reduce the current output. Doing so, the temperature dependence of the PVs performance is not well-established. Depending on the operation conditions, this may lead to an underestimation of the efficiency increase related to the temperature reduction that could be provided by a radiative cooler.

To overcome these problems, we developed and present in the current chapter a coupled thermal-electrical model, which takes into account all the major intrinsic processes affected by the temperature variation in a PV device, to examine the physical mechanisms on how a radiative cooler affects the overall efficiency of commercial photovoltaic modules. The impact of a photonic cooler in each spectral regime, either over solar (0.28–4 μm) or thermal wavelengths (~4–33 μm), and the resulting final PV performance enhancement, can now be distinguished and quantified, as well as the contribution of each principal mechanism (see Section 4.2), on the temperature sensitivity and PV performance.

4.2 ELECTRICAL PROPERTIES

To convert sunlight to electricity there must be firstly a generation of electron-hole pairs (opposite charges) at the expense of absorbed photons. With an appropriate mechanism, these generated carriers should be separated and forced to recombine only through an external circuit to produce current. In most solids, though, various (radiative or non-radiative) mechanisms of electron-hole recombination, before carriers being able to contribute to an external current, limit the current output. Moreover, for a device to produce significant power, even if it generates current, the output voltage, affected by the energy each carrier has as it goes to the external circuit, should be high enough. In most solids, high energy carriers would quickly lose their energy as heat (lattice vibrations or phonons) due to collisions with their surroundings. This process, often called thermalization, occurs in a very short timescale (0.1–10 ps), and could limit the voltage output of a solar cell as the charge carriers would be left with a lower potential energy.

These two requirements (ensuring carrier separation and sufficient voltage) can be met by appropriate semiconductor structures. The energy loss in semiconductor materials would be lower as carriers would fall to the bottom of the conduction band. However, care must be taken since a much higher energy bandgap would forbid photons of lower energy to excite carriers, resulting to lower current. Additionally, a semiconductor *p-n* junction can be utilized to achieve charge carrier separation. These features and possibilities made semiconductor-based solar cells a popular option.

In the present chapter we mainly focus on highly efficient mono-crystalline silicon-based solar cells such as the ones that are currently on the market of solar cell technology [88]. Selected PV technologies were preferred, on the one hand to simplify the theoretical model, without the study to lose its

physical significance, and on the other hand to exploit the impact of passive radiative cooling on optimized photovoltaics that are close to a performance saturation level [89].

Crystalline silicon-based solar cells are basically *p*-*n*-homojunction diodes, that is a junction of a *n*-type and *p*-type doped silicon which possess an excess of free electrons and holes in their carrier concentrations, respectively. The importance of the *p*-*n* junction arises by the carrier separation and the selective transport needed for the photo-generated electron and hole carriers to reach the appropriate contact to produce an electrical current. The forces acting on the photo-generated electron and hole carriers are the gradients introduced by the quasi-Fermi energy level splitting (qV) in both the *n*- and *p*-type material [90] under steady-state non-equilibrium illuminated conditions, since the free electron (n) and hole (p) carrier concentrations strongly depend upon illumination. These, however, are not sufficient to cause selective carrier transport. Functional separation and selective transport of electrons and holes to different contacts in real solar cells is only possible (if not an external voltage is present) via an additional property, i.e., by establishing different conductivities for each of them required in the different regions of the device [90]. Otherwise, both increased recombination of electrons and holes reaching the same contact, known as surface recombination, as well as bulk recombination of photogenerated carriers within the bulk of the *p*- and *n*-type materials before reaching the appropriate contact, result to decreased efficiency of the solar cell structure.

To better understand the electronic behavior of an electrically homogeneous solar cell, we depict in Fig. 4.1 an electrically equivalent one-diode circuit model based on discrete ideal electrical components.

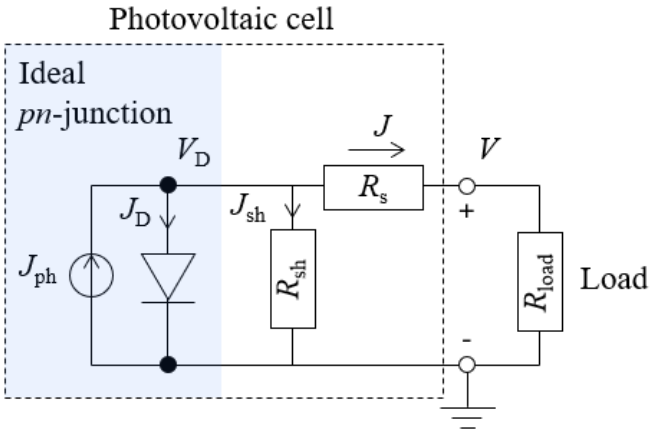

Fig. 4.1: Equivalent circuit model of a photovoltaic cell with load, discussed in the main text.

The solar cell can be modelled by a current source that represents the current of the photo-generated carriers (J_{ph}), in parallel with a diode (D) that represents the *p-n* junction, and an ohmic resistor called series or contact resistance, R_s, that considers how efficiently the contacts collect the carriers. A shunt resistance, R_{sh}, is also added and represents the adverse alternate current path due to the manufacturing defects. V represents the output voltage, arising by the separation of the quasi-Fermi levels of the *p-n* junction under illumination that also takes into consideration the voltage drop due to R_s. A resistive load (R_{load}) is varied between short circuit (R_{load}=0) and open circuit conditions ($R_{load}\rightarrow\infty$), while measuring the voltage (V) across the solar cell terminals and the current density (J) out of these terminals. The characteristic internal resistance of a solar cell is its output resistance at its maximum power point, i.e., at $max(JV)=J_{mp}V_{mp}$. Thus, if R_{load} equals this characteristic resistance, then the maximum power is transferred to the load. The characteristic internal resistance is a property mostly related to the materials out of which the solar cell is made. However, it has not a fixed value; it is affected by several variables, including temperature and the amount of light incident on the solar panel [91]. Consequently, when examining passive radiative cooling in solar cells, identifying which of the above parameters (R_s, R_{sh}, surface or bulk recombination, etc.) are mostly affected by the temperature variations and how is of great importance to accurately describe PVs' temperature sensitivity.

Two of the main assumptions of the theoretical modeling developed in this work are that we neglect the effect of how efficiently the contacts collect the photo-generated carriers and the impact of the PV defects. Such assumptions are quite valid for calculating the absolute efficiency, η, of mono-crystalline silicon-based solar cells, since their internal quantum efficiency (IQE) (i.e., number of charge carriers collected versus the number of incident photons absorbed) is near-unity [92]. Primarily, since we are mostly interested on the efficiency changes owing to the operating temperature variations, studies have shown that the decrease of η with increasing temperature is mainly controlled by the reduction of V_{OC} with T, where V_{OC} is the output voltage at open circuit conditions ($R_{load}\rightarrow\infty$), $\eta=J_{mp}V_{mp}/P_{inc}$ and P_{inc} is the total incident power density of the incoming sun radiation. For relatively highly-efficient cells the V_{OC} change usually constitutes the 80 to 90% of the η change, with a rather small dependence on R_s [93,94]. Moreover, for photovoltaic cells with relatively high current densities the effects of shunt resistance can also be neglected [95]. Therefore, the temperature impact on both the contact and shunt resistance, as well as on J_{SC} is neglected in the

present study, thus leaving the efficiency dependence with temperature to be mainly controlled by the intrinsic material properties of the semiconductor of the solar cell. In our model, besides radiative recombination, we further take into consideration the only fundamental nonradiative loss mechanism in mono-crystalline silicon (assuming no defects in the crystalline structure), the Auger recombination. Regarding the impact of the PV defects and the defect originated recombination, in the case of PVs with high surface passivation the prevailing defect-based recombination mechanism is the bulk-defect recombination. Thus, in the case of low bulk defect concentrations [high Shockley-Read-Hall (SRH) life-times] the Auger recombination becomes dominant [96,97]. Hence, in highly-efficient cells with minimum power-temperature coefficients the Auger recombination mechanism prevails over the other possible non-radiative recombination mechanisms [98], justifying the assumptions of our modelling.

The detailed balance method described by Shockley and Queisser [57] which governs the solar cell operation relates the current density, J [in A/m^2], in ideal (and electrically homogeneous) solar cells, i.e., in the radiative limit assuming full collection of all generated carriers, to the output voltage, V [in V], by balancing the particles entering and exiting the device. To this extent, the limiting efficiency, for every temperature, of such solar cells is due to the balancing of the number of photons absorbed by the solar cell with the number of carriers exiting the cell either to produce electrical power or to result to emission through radiative recombination of electron-hole pairs. As described above, in the present work, we further take into consideration the non-radiative-Auger recombination loss mechanism. Following Shockley's and Queisser's method, the current density obtained in an electrically homogeneous mono-crystalline silicon-based solar cell under illumination can be calculated by

$$J(V,T) = J_{0,rad}(T)\left(e^{qV/k_BT} - 1\right) + J_A(V,T) - J_{SC}, \quad (4.1)$$

where q is the elementary charge of an electron, k_B is Boltzmann's constant [in eV/K], T is the operating temperature [in K] and J_A is the nonradiative recombination current density due to Auger recombination. The term

$$J_{SC} = q\int_{0.28\ \mu m}^{1.107\ \mu m} \alpha_{cell}(\lambda,\theta_{sun})\Phi_{AM1.5G}(\lambda)d\lambda, \quad (4.2)$$

is the current density flowing at short-circuit conditions under the illumination of the sun. $\Phi_{AM1.5G}$ is the photon flux density [in photons·m^{-2}·s^{-1}·nm^{-1}] of the

"AM 1.5G" standard sunlight spectrum [55] reaching the Earth's surface, which is universal when characterizing solar cells. This term is simplified to equal the photocurrent since in Equation (4.2) the external quantum efficiency (EQE) of the solar cell (i.e., number of charge carriers collected versus the number of incident photons) is replaced by its absorptivity, $\alpha_{cell}(\lambda,\theta_{sun})$, owing to the near-unity internal quantum efficiency in mono-crystalline silicon-based solar cells [92]. θ_{sun} is the solar incidence angle. The first term in Equation (4.1) represents the voltage-dependent radiative recombination current density in the dark. It is a product of the energy distribution of carriers, at a specific operating temperature of the solar cell, that have enough energy to flow through the junction, in the opposite direction from the photogenerated current, and recombine [90]. The energy distribution of carriers and consequently the dark current density follow the Fermi statistics, which, if the Fermi level is lying within the band gap (as in our case), corresponds to Maxwell-Boltzmann statistics. The term qV characterizes the quasi-Fermi energy level splitting, i.e., the difference in the quasi-Fermi levels of electrons and holes [the term "quasi" is due to the non-equilibrium (i.e., under-solar-illumination) steady state]. Lastly, $J_{0,rad}$ is the saturation radiative current density which is independent of bias and it is determined by the thermal excitation level of carriers quantified by the temperature-dependent blackbody (BB) spectrum (Φ_{BB}, see Equation 4.4):

$$J_{0,rad}(T) = q\int_{0.28\ \mu m}^{1.107\ \mu m} \alpha_{cell}(\lambda,\theta_{sun})\Phi_{BB}(\lambda,T)d\lambda, \quad (4.3)$$

Following Planck's formulation, the photon flux (Φ_{BB}) of a blackbody at a temperature T can be well accounted by

$$\Phi_{BB}(\lambda,T) = \left(\frac{2\pi c}{\lambda^4}\right)\cdot\frac{1}{e^{hc/\lambda k_B T}-1}, \quad (4.4)$$

where h is Planck's constant and c is the speed of light.

The Auger recombination rate, which is specific to the chosen semiconductor material, under Boltzmann's approximation and assuming equal electrons, holes number ($n = p$) and $np >> n_i^2$, is given by [99,100]

$$J_A(V,T) = q\cdot 2A_r(T)\cdot n_i^3(T)\cdot e^{3qV/2k_BT}\cdot W, \quad (4.5)$$

where W is the thickness of the silicon layer. In Equation (4.5), the temperature-dependent Auger coefficient, $A_r(T)$, is extracted from Ref. [101]

and it describes solar cells with lowly doped silicon base, such as today's optimum crystalline silicon solar cells [96,102]. The temperature-dependent intrinsic carrier concentration, $n_i(T)$, is the commonly accepted value, by Refs. [103,104]. As proven in Ref. [104], at 300 K, at lower doping densities ($<10^{16}$ cm^{-3}, relevant for the optimum crystalline silicon solar cells) and low carrier injection levels (as in solar cells of typical resistivities), the impact of silicon bandgap narrowing with temperature-increase is not significant; hence it is neglected in our study.

Equation (4.1) assumes that the dark current density remains the same during illuminated conditions and the net current density is driven to negative current direction by the short-circuit current J_{SC} (that flows in the opposite direction from the dark current) which, at least for silicon-based solar cells, is independent of the bias [105]. In such cases, the superposition [see Equation (4.1)] of the dark and illuminated *JV* characteristics of a diode is valid. The efficiency, η, of the solar cell is given by

$$\eta = \frac{P_{ele,max}}{P_{inc}} = \frac{J_{SC}V_{OC}FF}{P_{inc}} = \frac{J_{mp}V_{mp}}{P_{inc}}, \quad (4.6)$$

where $P_{ele,\,max} = \max(-JV) = J_{mp}V_{mp}$ is the electrical power density output of a solar cell operating at the maximum power point [91], P_{inc} is the total incident power density of the incoming sun radiation and $FF = J_{mp}V_{mp} / J_{SC}V_{OC}$ is the fill factor. The term V_{OC} is the maximum voltage, usually referred as the open-circuit voltage, and results from Equation (4.1) by setting the total current $J = 0$ and solving for *V*.

As discussed above, the limiting efficiency of a solar cell depends upon balancing of particles entering and exiting the device for a specific operating temperature of the system. More specifically, assuming only radiative recombination, if the cell operates at high temperature (thus the current $J_{0,rad}$ becomes higher) the quasi-Fermi energy level splitting (qV) must be reduced to maintain a balance between the number of absorbed photons and the number of the emitted photons (see Fig. 4.2) [94,106]. This results to lower V_{OC} and V_{mp} and lower efficiencies.

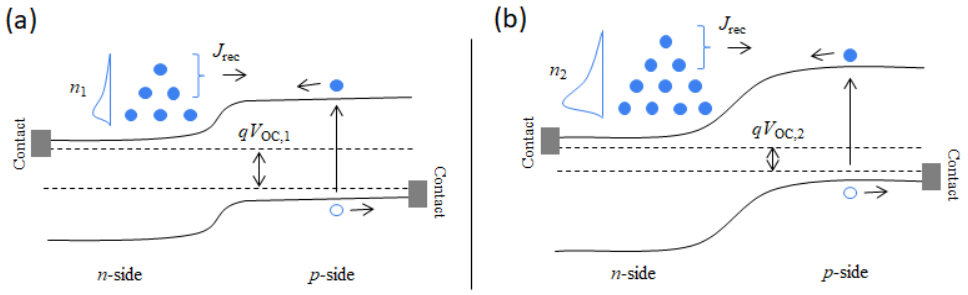

Fig. 4.2: Simplistic photovoltaic cell under open-circuit conditions, showing energy band diagrams and the path of carriers through a pn-junction under illumination and different device temperatures (T); T_1 in (a) and $T_2>T_1$ in (b). Voltage is lower in (b) case compared to (a) to maintain a balance between the number of absorbed photons and the number of recombined photons, where n is the energy distribution of carriers that depends on the thermal excitation, and J_{rec} is the recombination current density.

Regarding the nonradiative Auger recombination process, J_A scales with the intrinsic carrier concentration cubed [see Equation (4.5)]. Therefore, at elevated temperatures the Auger recombination rate is higher, due to the increased thermally generated carrier concentrations, as a result of the "multiple-particle-interaction" nature of the Auger effect [101].

Typically, any recombination process has a dual impact: it results both to a current loss, because some excited charges don't make it to the external circuit, and to a voltage loss, because the generation-recombination balance is diminished. Still, the energy losses (upon energy conversion) in a solar cell are distinguishable. Even though all energy loss mechanisms stem from the same physical process, i.e., carrier recombination, they are distinguished to those that reduce the current and those that reduce the voltage [94]. Such a distinction is important when examining the temperature effect on the efficiency. Improving the generation-recombination balance, for example, implies improved temperature sensitivity of the device. Open-circuit voltage is a good indicator of the generation-recombination balance (see Fig. 4.2). Therefore, the energy loss mechanisms that limit open-circuit voltage should be identified.

Following a thermodynamic analysis of losses in ideal solar cells [107], the open-circuit voltage generated by the usual *p-n* junction cell is limited on account of entropy generation in the conversion process. In the ray optics limit and assuming full collection of all generated carriers, qV_{OC} is smaller than the bandgap energy E_g according to

$$qV_{OC} = E_g\left(1 - \frac{T_c}{T_s}\right) - k_B T_c\left[-\ln\left(\frac{\gamma_s(E_g, T_s)}{\gamma_c(E_g, T_c)}\right) + \ln\left(\frac{\Omega_{emit}}{\Omega_{abs}}\right) + \ln\left(\frac{4n^2}{I}\right) - \ln(QE)\right], \quad (4.7)$$

The first term describes the Carnot limit for conversion of thermal energy into work, where T_c and T_s are the temperature of the cell and the sun, respectively. The second term results from the mismatch between Boltzmann distributions at T_c and T_s. Specifically, the first and the second term describe the entropy generation by "photon cooling", from temperature T_s to temperature T_c, due to the thermalization of photogenerated electron-hole pairs by the interaction with lattice. Energy loss due to thermalization represents one of the two fundamental losses in the Shockley-Queisser theory of ideal solar cell efficiency [57]. Aside from heat, entropy is also transferred to the lattice, in this cooling process, decreasing the entropy of the excited carrier population, recoupling some of the loss [108]. The third term is the voltage loss due to the entropy generation as a result of a mismatch between the emission solid angle, Ω_{emit}, of the cell and the absorption solid angle, Ω_{abs}. This term declines by focusing the incident sunlight to maximum concentration, for example [109]. The fourth term describes the effect of incomplete light trapping inside the solar cell, where n is the refractive index (of Si in our case) and I is the light concentration factor [110]. Finally, the last term is the voltage loss owing to the non-radiative exciton recombination, where $QE=R_{rad}/R_{rad}+R_{nrad}$ is the quantum efficiency and R_{rad}, R_{nrad} are the radiative and non-radiative recombination rates, respectively. The last two terms can be enhanced through optical means by increasing the local density of optical states, which in turn leads to an improved R_{rad} outcoupling and an improved light incoupling or light trapping [111]. However, although crystalline silicon has a relatively large absorption coefficient at ~0.28-0.8 μm (~6000-800 cm^{-1} at ~0.55-0.8 μm), yet the absorption coefficient is ~10^4 times weaker at its indirect band edge (~1.1 μm). The probability of emission at open circuit is also very low. Indicatively, its probability for internal emission is well-below 10% compared to a high-quality direct-bandgap GaAs material for example with a probability of internal emission that has been experimentally tested to be 99.7% and 72% externally [112]. This highly-quenched internal emission, as a result of the indirect bandgap property, prevents crystalline silicon-based PVs from achieving an enhanced external fluorescence to reduce voltage loss and hence approach the SQ limit, despite the high J_{ph} [89].

The previously discussed energy losses impact the balance between absorption and emission rates, therefore are often called balance losses [94]. Equation (4.7) indicates their temperature dependence, resulting to the temperature sensitivity of the cell. We plot this temperature dependence in Fig. 4.3, in the case of a crystalline silicon-based PV with E_g=1.12 eV, constant QE=5% (in practice R_{rad}, R_{nrad} depend on T, V [113]), assuming 90% light-trapping and T_s=5525 K.

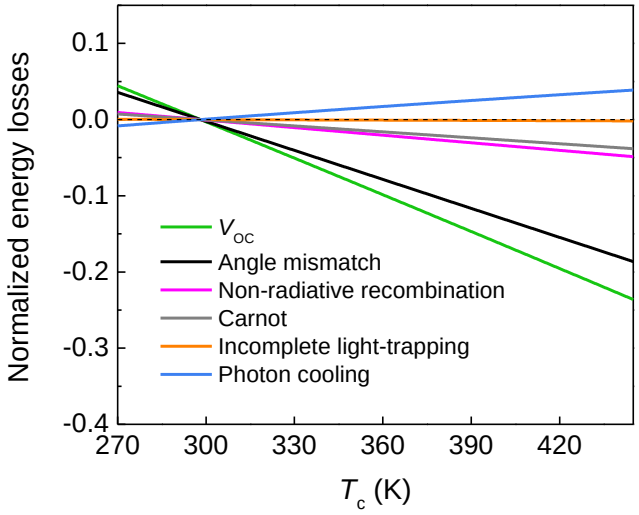

Fig. 4.3: Temperature-dependent balance losses [see Equation (4.7)] for a realistic crystalline silicon-based PV (i.e., E_g=1.12 eV, QE=5 %, 90% light-trapping). The different lines show the contribution of different terms of Equation (4.7). The green line corresponds to the resulting temperature dependent V_{OC} output.

In this simplistic case, the "balance losses" are shown to be sensitive to temperature and vary approximately linearly (see Fig. 4.3). This explains the generally observed linear temperature-PV-yield relation. For that reason, temperature sensitivities of solar cells are often described by a single value of temperature coefficient and are usually normalized at Standard Test Conditions (STC), i.e., 1000 W/m² irradiance, AM 1.5G, T_c=298.15K), expressed in %/K (see Section 4.3). Typically, because of this normalization, any mechanism affecting the efficiency of the cell modifies its output-power-temperature coefficient. Moreover, the "balance losses" result to a negative temperature impact on the V_{OC} output (see green line in Fig. 4.3). This implies that the temperature sensitivity may improve by eliminating them. For instance, modifying the radiative/nonradiative recombination rates or optimizing the light in/out-coupling, may decrease the adverse temperature effect in PVs [111]. This can be seen, in Fig. 4.3, by the near-zero, negative-

valued slope of the orange line, corresponding to the penultimate term in Equation (4.7) for the case of optimized crystalline silicon-based PVs, i.e., assuming 90% light-trapping.

4.3 POWER– AND VOLTAGE–TEMPERATURE COEFFICIENT

To evaluate/validate our approach, of properly determining the temperature sensitivity of a solar cell, we initially calculated the efficiency and the open circuit voltage changes with respect to the operating temperature variations. Then, we compared our calculated power-temperature and voltage-temperature coefficients (i.e., the slopes of the $P_{ele,max}$-T, V_{OC}-T curves) with those of commercial PVs measured and provided by the manufacturers (the slopes of the $P_{ele,max}$-T, V_{OC}-T curves are normalized at % compared to a PV operating at Standard Test Conditions (STC) [i.e., 1000 W/m² irradiance, AM1.5G, T_{cell}=298.15K]). In particular, we calculated, for our theoretical PV (with silicon data obtained from Refs. [101,103], see Section 4.2), a constant power-temperature coefficient equal to -0.293%/K and a voltage-temperature coefficient equal to -0.244%/K, confirming that the efficiency changes with temperature are linear. As expected, the above values of power-temperature and voltage-temperature coefficients, despite being lower compared to the mainstream, multicrystalline silicon-based modules (with power-temperature coefficients around -0.45%/K to -0.40%/K), they match the data of well-optimized and highly-efficient IBC PVs, such as the SunPower's Maxeon Gen III or LG's IBC solar cells (see Fig. 4.4) [114–116].

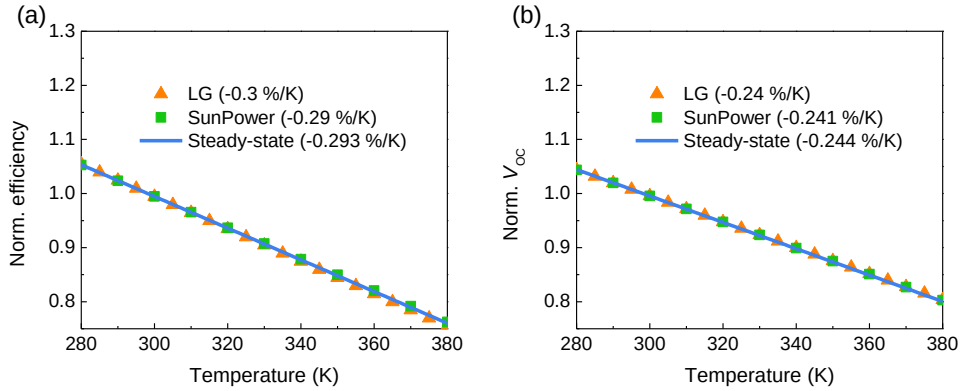

Fig. 4.4: (a) Steady-state efficiency and (b) V_{OC} change normalized at %, compared to a PV operating at STC, and plotted against temperature, in comparison with the power-temperature, V_{OC}-temperature curves plotted from the temperature coefficients (i.e., slopes

of the normalized $P_{ele,max}$-temperature V_{OC}-temperature curves) obtained from manufacturers [114,115].

For highly efficient PVs (η~22.8 %) our calculations showed that the efficiency changes are mainly controlled by the voltage changes with temperature; as shown in Figs. 4.5 and 4.6, this is a consequence of the increased carrier concentrations, n_i, at elevated temperatures and hence increased carrier recombination in the bulk [96,117], further supporting the validity of our assumptions. Consistent with Refs. [59,96], Fig. 4.5(b) shows that the impact of the radiative recombination current density, J_{rad}, is much lower than the non-radiative, J_{nrad}, [first two terms in the r.h.s, of Equation (4.1)], a consequence of the indirect bandgap property of c-Si.

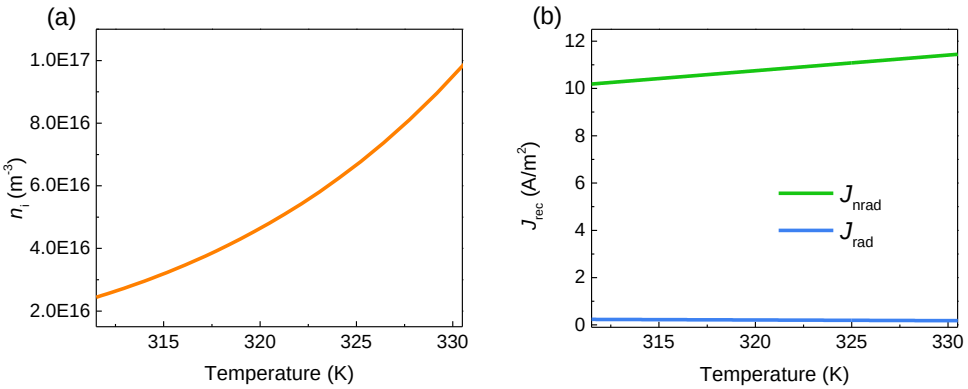

Fig. 4.5: (a) Intrinsic carrier concentration, n_i, dependence on temperature. As the temperature increases n_i increases leading to increased recombination current, J_{rec}, as shown in (b). (b) Nonradiative, J_{nrad}, (green line) and radiative, J_{rad}, (blue line) recombination current density vs. temperature, for an IBC PV described in Chapter 4.

The open-circuit voltage, V_{OC}, is limited on account of entropy generation in the conversion process (see Section 4.2). As seen in Fig. 4.5(b), as the temperature increases, the nonradiative Auger recombination increases which in turn reduces the quantum efficiency [see Fig. 4.6(a)], defined as $QE=J_{rad}/(J_{rad}+J_{nrad})$. The entropic factor, $k_BT\ln(QE)$ [last term in Equation (4.7)], gains a steeper slope, compared for example to the case corresponding to a fixed QE value of ~2.23%, [see Fig. 4.6(b)], arising by the temperature dependent QE, which in turn increases the voltage losses with temperature or the voltage-temperature coefficient. Since we assume no other nonradiative recombination process to be present in the device, the voltage-temperature coefficient sets at ~-0.244 %/K due to the Auger recombination effect, matching the temperature coefficients obtained from manufacturers of IBC solar cells (see Fig. 4.4).

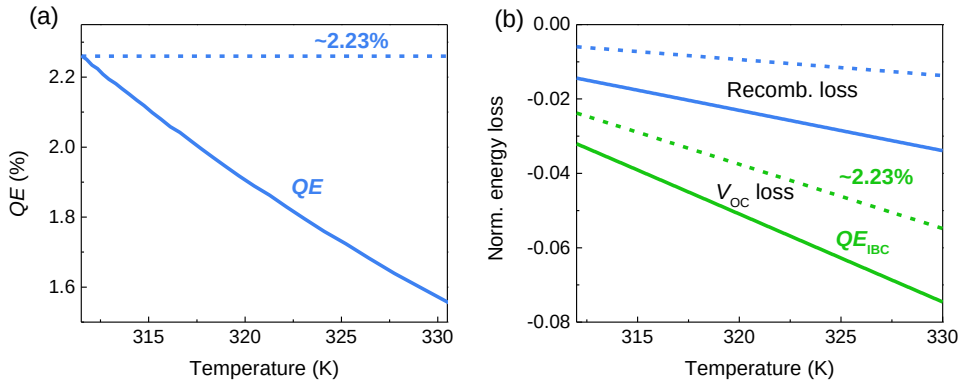

Fig. 4.6: (a) Quantum efficiency, QE, dependence on temperature for an IBC PV described in Chapter 4 (solid line), compared to a PV of fixed QE~2.23% (dashed line). (b) Temperature-dependent recombination energy loss calculated by $k_BTln(QE)$, and the resulting normalized (to $V_{OC,298.15\ K}$) temperature dependent V_{OC} output, for a fixed QE~2.3% (dashed lines) and for the QE shown in (a) (solid lines).

In general, the minimum power-temperature coefficients imply that only the intrinsic radiative and the Auger recombination mechanisms [98] are considerable. Indicatively, assuming only radiative recombination, the power-temperature and voltage-temperature coefficients are reduced almost down to the half (-0.168%/K, -0.117%/K), implying a significant underestimation of the efficiency increase related to the temperature reduction that could be provided by a radiative cooler. Alternatively, as one optimizes the PV performance, the temperature coefficients reduce, implying enhanced PV yield, since Standard Testing Conditions are rarely met in the field. The excellent agreement of our theoretical calculations with the experimental data of Refs. [114–116] provided by the PV manufacturers allow us to examine the radiative cooling impact on the efficiency assuming PVs which operate outdoors.

4.4 THERMAL ANALYSIS

To consider the effect of heating in solar cells, and thus to be able to calculate the extracted electrical power or efficiency in respect to the operating temperature at typical outdoor conditions, we perform a thermal analysis. The SQ efficiency limit assumes a solar cell operating at a constant temperature, usually at 300 K. In reality, the solar cell heats up considerably above the ambient temperature. The operating temperature of the cell of a photovoltaic module can be accurately described by treating the PV as a uniform device by

using appropriately combined conduction-convection heat transfer coefficients. A thermal analysis for the PV can thus be performed by balancing the total power into and out of the device following Planck's blackbody formalism and Kirchhoff's law, i.e., the spectral-directional absorptivity equals the spectral-directional emissivity. This strategy (passive radiative cooling strategy), described in Section 3.2, was firstly proposed by Fan [50,51] for calculating the radiative cooling of solar absorbers and has been shown to exhibit highly accurate results [15]. According to Fan, when a structure operates outdoors exposed to a daylight sky, it is subject to both solar irradiance and atmospheric thermal radiation (corresponding to ambient air temperature T_{amb}) (see Fig. 4.7).

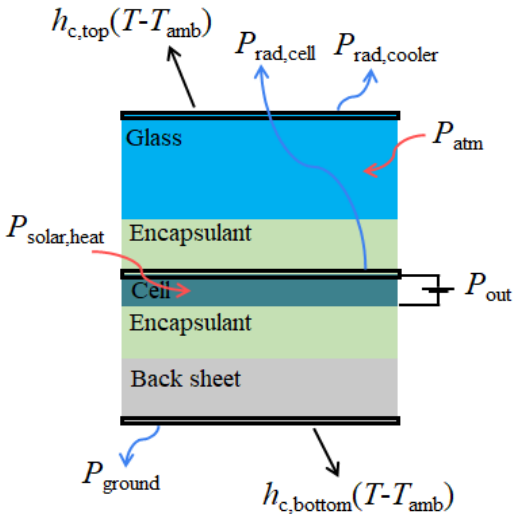

Fig. 4.7: Schematic of the material stacking of the encapsulated crystalline silicon-based PV and power "into" and "out of" the device. The different power terms shown are described in the text. The different PV layers and their role are analyzed in more detail in the next section.

In the case of a PV instead of a solar absorber, the operating temperature or the steady-state temperature (T) is calculated by employing a non-equilibrium steady-state power-balance described by Equation (4.8), which is determined by summing the total power "into" and "out of" the cell [106]:

$$P_{rad,cooler}(T) - P_{atm}(T_{amb}) + P_{cond,conv}(T,T_{amb}) + P_{ground}(T,T_{amb}) - P_{solar,heat}(V,T) = 0, \quad (4.8)$$

In Equation (4.8), $P_{cond,conv}(T,T_{amb})=h_c(T-T_{amb})=h_{c,top}(T-T_{amb})+h_{c,bottom}(T-T_{amb})$ is a power density loss (since in our case $T>T_{amb}$) due to conduction and

convection owing to the contact of the cooler with external surfaces and the air adjacent to its top and bottom surface. $P_{rad,cooler}(T)$ [see Equation (3.4)] is the power density (W/m^2) radiated from PV's surface and PV's cooler, and $P_{atm}(T)$ [see Equation (3.7)] describes the absorbed by the cooler thermal radiation emitted from the atmosphere. $P_{ground}(T,T_{amb})=P_{rad,bottom}(T) - P_{earth}(T_{amb})$ represents the cooling due to radiative energy transfer to the ground from the back-side. The ground temperature is assumed to be the same as the ambient temperature (in practice, it could be slightly lower than T_{amb}).

The last term, $P_{solar,heat}(V,T)$, is the absorbed solar power density that dissipates into heat which incorporates the electrical part and formulates as follows:

$$P_{solar,heat}(V,T) = P_{sun} - P_{ele,max}(V,T) - P_{rad,cell}(V,T), \quad (4.9)$$

The first term in Equation (4.9), P_{sun}, is the total solar absorption power density by the cell [see Equation (3.8)] that either dissipates into heat or results to beneficial electrical power (calculated using the method of detailed balance by Shockley and Queisser [57] described previously) or radiated power by the cell (via radiative carrier recombination). The power radiated by the cell is given by

$$P_{rad,cell}(V,T) = \int d\Omega cos\theta \int_{0.28\ \mu m}^{1.107\ \mu m} \varphi\left(\lambda,T,qV_{mp}\right)\varepsilon_{cell}(\lambda)d\lambda, \quad (4.10)$$

where the angular integration is over a hemisphere. $P_{rad,cell}(V,T)$ is also known as the non-thermal radiation emitted by the solar cell as a consequence of the bandgap of the semiconductor material [118]. Consequently, it depends on both the quasi-Fermi energy level splitting (qV), and the operating temperature. Following generalized Planck's law [118], the emitted spectral irradiance, $\varphi(V,T,\lambda)$, under the applied bias voltage V (for $E - qV >> k_BT$, where E is the photon energy in eV), is given by:

$$\varphi(V,T,\lambda) = \varphi_{BB}(T,\lambda)e^{qV/k_BT}, \quad (4.11)$$

where $\varphi_{BB}(T,\lambda)$ is the spectral irradiance of a blackbody at a temperature T:

$$\varphi_{BB}(T,\lambda) = \left(\frac{2hc^2}{\lambda^5}\right)\cdot\frac{1}{e^{hc/\lambda k_BT}-1}, \quad (4.12)$$

In Equation (4.10) we assume that the solar cell is operating at the maximum power point (V=V_{mp}). Finally, $\varepsilon_{cell}(\lambda) = \alpha_{cell}(\lambda,\theta_{sun})$ is the emissivity of the silicon layer that is assumed independent of polar angle θ, even if the front surface of silicon is flat, because of its high refractive index that refracts the incident light very close to perpendicular inside the solar cell.

In this way, the electrical power of a PV exposed to the outside at a corresponding operating temperature (defined as the steady state temperature or operating temperature) is self-consistently determined by obtaining the solution of Equation (4.8) [combined with Equation (4.9)] for a PV operation at the maximum power point (V=V_{mp}). We note that in cases that PV's optical response, within the absorption band of silicon, is not affected by the incorporation of a top coating/cooler for example, the power-, voltage-temperature coefficients given from PV manufacturers can be incorporated in Equation (4.8) in addition to the absorption properties of PV's architecture in the last term of Equation (4.8) [although less information is extracted related to the current-voltage (J–V) PV characteristics]. Equation (4.8) then reduces to:

$$P_{rad,cooler}(T) - P_{atm}(T_{amb}) + P_{cond,conv}(T, T_{amb}) + P_{ground}(T, T_{amb}) - P_{sun} + P_{ele,max}(T) = 0, \quad (4.13)$$

where $P_{ele,max}(T)$ is given by:

$$P_{ele,max}(T) = P_{STC}(298.15\ K) \times [1 + \beta \times (T - 298.15\ K)], \quad (4.14)$$

where P_{STC}(298.15 K) is PV's output power at Standard Test Conditions and β=dP/dT(%) is the power-temperature coefficient normalized at % compared to the PV operating at STC.

4.5 OPTICAL PROPERTIES

In the present work we focus on crystalline silicon-based solar cells such as the ones that are currently on the market of solar cell technology [88]. A typical state-of-the-art silicon-based photovoltaic module along with each interlayer is shown in Fig. 4.8(a).

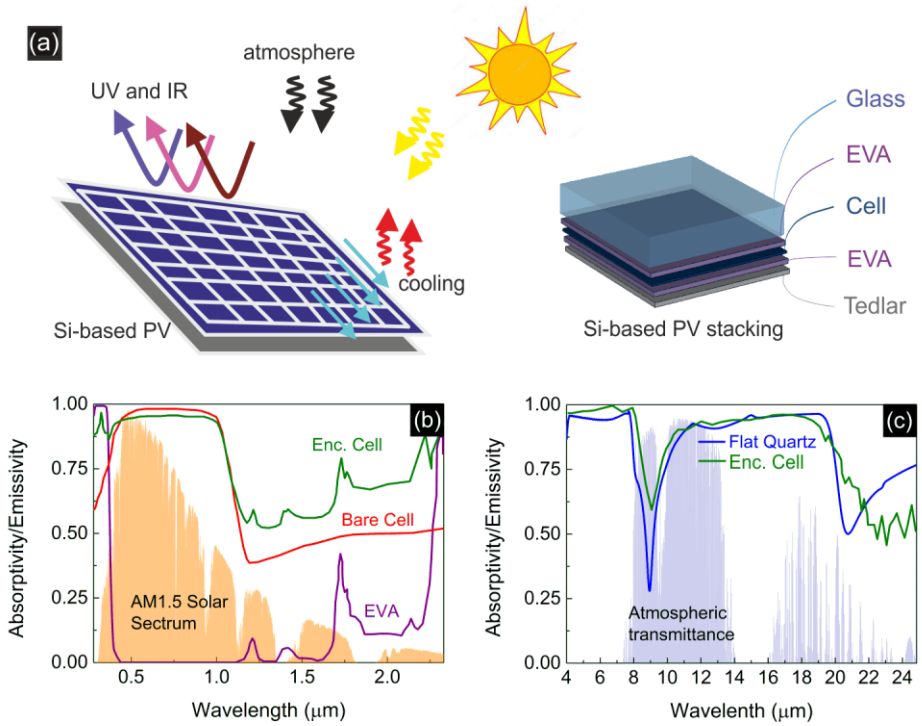

Fig. 4.8: (a) Schematic of the cooling approaches for the radiative thermal management of PVs and material stacking of the encapsulated crystalline silicon-based solar cell. The thickness and role of the different layers of the PV module are discussed in the main text. (b) Absorptivity of the bare cell (red line), encapsulated cell (green line), and of a 0.46 mm thick EVA wafer (purple line). Data are extracted from Refs [16,34,119]. *(c) Emissivity spectra in the thermal wavelengths (mid-IR) of a 3.2 mm thick glass (fused Quartz) layer (blue line), compared to the emissivity of the encapsulated cell (green line).*

These cells utilize thick Si wafers, reaching around 200 μm in the case of typical commercial c-Si cells. We assume that our cell involves a mono-crystalline silicon wafer with interdigitated state-of-the-art type back contacts (IBC) responsible for collecting the photogenerated carriers [120]. Highly-efficient IBC cells, besides being available in the market, match well the electrical-thermal analysis of our modeling (see Chapter 4.2) due to their highly crystalline structure, better surface passivation, relatively low base doping density and intrinsic carrier concentration [96]. All remaining layers, other than the cell, are required for its stable operation. More specifically, the transparent top surface, most often a 3.2 mm thick glass (contains 70−80% silica in addition to other materials like Al_2O_3, Na_2O, CaO, etc.) protects the exposed solar cell system from the outside conditions and provides mechanical strength and rigidity. The most common encapsulant, the EVA (ethylene-vinyl acetate), is used as a 0.46 mm thick joint that provides adhesion between the cells, the top (glass) and the rear (substrate: made of a 0.5 mm thick Tedlar: polyvinyl fluoride) rough surfaces of the PV module.

The main requirements of both the glass and the encapsulant are stability at elevated temperatures and high UV exposure, low thermal resistivity and optical transparency for the incident radiation to reach the cell.

A basic schematic of light propagation through a solar panel is shown in Fig. 4.9.

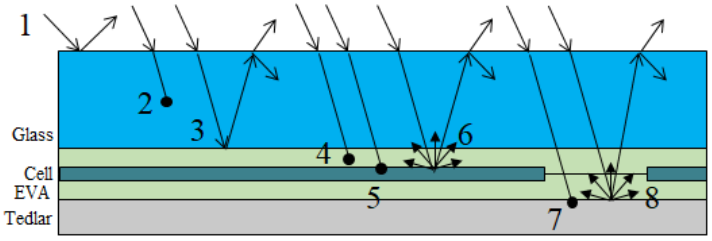

Fig. 4.9: A cross section of a solar panel showing 8 different cases of light propagation. This diagram is reproduced from Ref. [119]. *The arrows indicate the path of incident light and the dots the absorbed rays.*

Multiple layers with various optical properties and thickness affect the incoming light differently. For each wavelength and angle of incidence, the final light absorption inside the cell is affected by several optical mechanisms such as reflection at the interfaces (cases 1, 3, 6, 8), transmission and absorption in each layer (cases 2, 4, 5, 7) and the light-trapping effect (cases 3, 6, 8). Reflection at 6 and 8 (EVA–cell, EVA–Tedlar interface, respectively) is often modified in conventional solar cells to being diffuse to increase the light-trapping effect inside the cell, while antireflection (ARC) coatings at the cell's surface further reduce reflection at the EVA–cell interface. Glass ARCs are often utilized usually made of MgF_2 or porous glass thin layers (~100 nm).

Despite the high optical transparency of both glass and EVA, inevitably the solar absorption spectrum of the encapsulated solar cell [structure shown in Fig. 4.8(a)] differs from that of the bare cell, including unwanted absorption losses, as shown in Fig. 4.8(b), where the absorption for a bare cell (red line), an encapsulated cell [16] (green line) and a single 0.46 mm EVA wafer [119] (purple line) is shown. It is clear that EVA strongly absorbs UV radiation (~< 0.375 μm) reducing thus the available photo-carriers reaching the cell at this regime, while for the wavelength range within the absorption band of silicon (indirect bandgap of ~1.107 μm) the absorption is slightly reduced mainly due to the reflection (~0.04) introduced from the top surface of the glass. Moreover, unexploitable sub-bandgap absorption, beyond 1.107 μm, up to 4 μm, is still very high, for both the bare and the encapsulated cell, despite that intrinsic silicon does not absorb in this regime. The reason is the non-zero absorption from the highly doped silicon regions, the metal contacts, the EVA

and the thin antireflection layers (usually made of SiN or SiO_2) usually placed on top of silicon, together with the light-trapping effect [15,16]. Consequently, sub-bandgap and UV radiation (of intensity ~150 W/m^2 according to our calculations) not only remain unexploited but also dissipate into heat, which further reduces the efficiency of the solar cell.

In the mid-IR/thermal wavelength range (4-33 μm), where we require the solar cell to emit (reducing thus the cell temperature), the emissivity spectrum of the encapsulated cell is mainly determined by the 3.2 mm thick top glass layer (see Chapter 3.3). This emissivity is shown in Fig. 4.8(c) for the encapsulated IBC cell (green line) and is compared with that of a flat fused quartz (blue line) with permittivity data as given by Palik [34]. We see that both cases of Fig. 4.8(c) exhibit strong phonon-polariton resonances at ~9 μm and ~21 μm that allow to achieve relatively strong absorptivity/emissivity in the thermal wavelength range of 7-27 μm. On the other hand, around the wavelengths of the phonon-polariton resonances (in the ranges of 8-13 μm and 19-30 μm) there is a strong impedance mismatch between glass and air leading to large reflectivity, associated with dips in absorptivity/emissivity. These emissivity dips coincide with the transparency window of the atmosphere [see Fig. 4.8(c)], and as a result they lead to reduction of the cooling capability of the system. Therefore, eliminating them is of high importance and has been extensively studied nowadays.

Comparing the two cases of Fig. 4.8(c) (blue vs. green line) considering that the encapsulated cell emissivity comes almost exclusively from its top glass layer, we see that the emissivity of the typical PV glass is slightly enhanced compared to that of quartz. To take into account quartz's inferior thermal emission and, since for the cover glass of the encapsulated IBC cell [green line in Fig. 4.8(c)] there are no available emissivity data with polar angle (note that the realistic radiative cooling through the atmosphere is affected by both the glass real spectral emissivity and by the decline of glass emissivity with polar angle), the soda-lime glass permittivity data are obtained from Ref. [121] (similar to the realistic soda-lime glass cover at passivated emitter and rear cells (PERC) or with Al-back-surface-field (Al-BSF) back reflectors [98,121,122]).

In the current work, we calculate the absorptivity/emissivity, $\varepsilon(\lambda,\theta)$, of a top-coating/radiative-cooler (formed on the flat PV glass [see Fig. 4.8(a) right]), as well as the reflectivity, $r(\lambda)$, by performing full-wave electromagnetic simulations, using the commercially available software CST Microwave Studio, for wavelengths from 4 up to 33 μm with a 5^o angular resolution for $\varepsilon(\lambda,\theta)$, and from 0.28 up to 4 μm for $r(\lambda)$. Moreover, the absorptivity/emissivity, of the cell, $\varepsilon_{cell}(\lambda)$, is determined by $r(\lambda)$ and the data

deduced from Fig. 4.8(b) from Refs [16,34,119]. We note that $\varepsilon_{cell}(\lambda) = \alpha_{cell}(\lambda, \theta_{sun})$ is the emissivity of the silicon layer that is assumed independent of polar angle θ, which is clearly valid for a randomly textured surface like that of commercial solar cells.

5

OPTICS-BASED COOLING METHODS AND HEAT GENERATION REDUCTION

5.1 INTRODUCTION

As highlighted in Refs. [16,98,123,124], there are currently two major photonic approaches for the thermal management of PVs, focusing on controlling either (i) the solar absorption by reflecting parasitic UV, sub-bandgap radiation and further enhancing the beneficial optical absorption, or (ii) the thermal radiation emission. In the present chapter, employing the thermal-electrical modeling approach described in Chapter 4, we examine how a photonic cooler on top of a realistic PV system operating outdoors affects its overall efficiency and we distinguish and evaluate the impact of each of the previously mentioned photonic approaches [16,98] on the PV efficiency. In particular, in Section 5.2 we examine the physical origin of heating and power losses in commercial PVs. In Section 5.3 we analyze the radiative cooling potential and evaluate the gains [i.e., temperature reduction, relative efficiency increase, $\Delta\eta(\%_{rel})$] from improving the emissivity in the thermal wavelengths in mid-IR assuming the PV as a blackbody emitter (broadband, ideal thermal radiator). We further analyze the physical mechanisms of the efficiency enhancement related to the temperature reduction in PVs. In Section 5.4 we examine the potential and effects of mitigating thermal losses by either filtering sub-bandgap radiation (~1.107–4 μm), for different PV back-reflector technologies, or reducing the texture steepness at the front and rear surfaces of the cell. Finally, in Section 5.5, we evaluate in detail the total effect of the UV radiation on the operating temperature and PV efficiency.

The investigation presented in this Chapter is performed for two state-of-the-art encapsulated solar cells: a mono-crystalline silicon-based cell with interdigitated state-of-the-art type back contacts (IBC) [120], with an

electrical-power-temperature coefficient of ~-0.29 %/K, and a screen-printed silver front and aluminum rear contacts cell with Al-back-surface-field (Al-BSF) reflector technology [125], with an electrical-power-temperature coefficient of ~-0.45 %/K (which is the dominant technology in present production), with data obtained from [16,34,123].

5.2 PHYSICAL ORIGIN OF HEATING AND POWER LOSSES

In the present section, we discuss the opto-electro-thermal behavior of commercial, highly efficient, mono-crystalline silicon-based PVs with interdigitated state-of-the-art type back contacts (IBC) [120] that operate outdoors, by utilizing the theoretical model described in Chapter 4. Figure 5.1 shows the calculated steady-state [by solving Equation (4.8)] reflected, absorbed, in each layer of the encapsulated IBC cell, and electrical-output light fractions (power density and spectra). (Corresponding environment conditions are described in the caption of Fig. 5.1.)

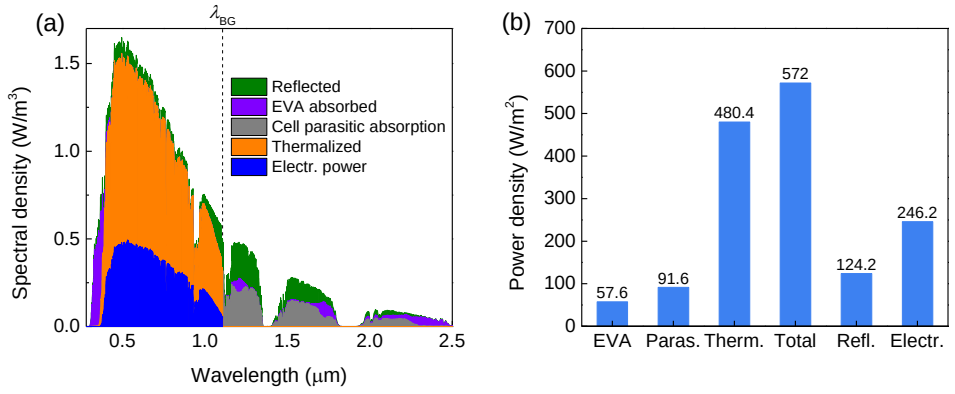

Fig. 5.1: Absorbed, reflected light results and power output for the IBC solar cell examined here, assuming operation under the AM1.5G spectrum, T_{amb}=300 K, $h_{c,top}$=10 W/m^2/K (υ_{top}~1.25 m/s wind speed [126]*), $h_{c,bottom}$=5 W/m^2/K (υ_{bottom}~0.75 m/s wind speed). Since, the wavelength-dependent emissivity of the back sheet is not available, $P_{ground}(T,T_{amb})=\sigma\varepsilon_{Tedlar}A(T^4 - T^4_{amb})$ was calculated using the Stefan–Boltzmann law, where ε_{Tedlar}=0.85 is the hemispherical emissivity of Tedlar* [123]*, σ is the Stefan–Boltzmann constant, and A~1 is the view factor. (a) Spectral density reflected (green) or parasitically absorbed by the encapsulant-EVA (violet) and the cell (gray), as well as that thermalized (orange) or extracted in the form of electrical power (blue) at steady-state conditions. (b) Power density spectra of (a) integrated, acting as heat sources and the reflected, electrical power density output.*

We assume that the parasitic absorption inside the absorption bands of c-Si (0.28–1.107 μm) stems only from the encapsulant-EVA [since there is no front side metallization in IBC cells – see vertical dashed line in Fig. 5.1(a)]. Hence, cell's parasitic absorption [see gray area in Fig. 5.1(a)] is related only to the sub-bandgap parasitic absorption, i.e., ~1.107–4 μm (plotted till 2.5 μm because ~99% of solar irradiance is between 0.28-2.5 μm). Sub-bandgap and UV parasitic absorption (see Section 4.5) account for ~13.7% and ~3.4% of PV's absorbed solar power, respectively, acting as a heat source. In addition to the sub-bandgap and parasitic absorption losses, there are also thermalization recombination losses to consider, constituting ~54.8% of the total absorbed power.

For the previously described environmental conditions, we find (applying the model described in Chapter 4) that the increased thermal load results to a module's steady-state temperature of ~320 K (typical PV operating temperature under peak solar irradiance [123,127]), ~20 K above ambient. In the case of an IBC solar cell (with a power-temperature coefficient of ~0.3 %/K [114,115]), such a temperature rise results to a ~6.6 % power drop compared to a PV operating at Standard Test Conditions (~298.15 K). Finally, about ~5.2 % of reflection losses inside the absorption band of c-Si further decline the power output of the device.

Results of Fig. 5.1 indicate the worthiness of further optimizing both PVs' optical and the thermal response, even in the case of highly-efficient commercial PVs. In the next parts of Chapter 5, we seek to address these issues by utilizing photonic concepts, and we examine their potential on PV's.

5.3 RADIATIVE COOLING

Although a PV cover glass, the traditional protective and cooling PV layer, is highly emissive in mid-IR, it is still not perfect especially within the atmospheric transparency window (8-13 μm). To illustrate that we calculate and plot in Fig. 5.2 the spectral and average emissivity between 8 and 13 μm as a function of polar angle, θ, for the soda-lime glass (3.2 mm thick, – considered herein as the conventional radiative cooler) in comparison with fused quartz (3.2 mm thick), the bare cell (for two cases: the highly efficient IBC cell and a cell with screen-printed silver front and aluminum rear contacts with Al-back-surface-field (Al-BSF) back reflector technology [125], being the dominant technology in present production, with data obtained from [16,98]) and a blackbody cooler (ideal).

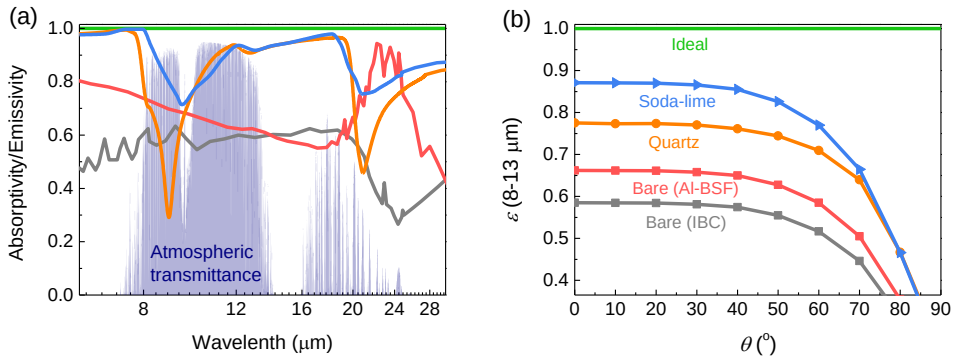

Fig. 5.2: (a) Emissivity spectra of the soda-lime glass (blue) in comparison with fused quartz (orange), a bare IBC cell (gray), a bare screen-printed silver front and aluminum rear contacts cell and Al-BSF back reflector technology (red) and a blackbody cooler (green) over the thermal wavelength range in mid-IR and (b) the average emissivity for the structures of (a) between 8 and 13 μm (the atmospheric transparency window) as a function of polar angle, θ.

As seen in Fig. 5.2(a), an encapsulated solar cell provides enhanced radiative cooling compared to the bare cells, since both soda-lime and fused quartz glasses in their bulk form act as fairly acceptable broadband (above-ambient) radiative coolers, the most the soda-lime PV glass due to its weak bulk phonon-polariton resonance compared to fused quartz. This is mainly because of the additives in the raw material that produce increased absorption especially in the atmosphere transparent wavelength range at the bulk phonon-polariton resonance [128]. Thus, soda-lime glass is a good reference to elaborate with radiative cooler designs considering also its reliability and technological impact (solar cells, windows, etc.). The emissivity of soda-lime glass remains higher for all angles below ~60° [see Fig. 5.2(b)], while for both glasses the emissivity reduces rapidly beyond ~60°. Overall, the averaged emissivity (over 8-13 μm – at θ=0°) of soda-lime glass equals to ~0.86 [very close to a commercial solar glass ($\bar{\varepsilon}$~0.84) [129], also in agreement with Ref. [72] (i.e., $\bar{\varepsilon}$~0.85)] compared to the less efficient fused quartz emitter ~0.77 [very close to Ref. [130] ($\bar{\varepsilon}$~0.73)], i.e., both have room for improvements. When considering the entire thermal IR spectrum (~4-33 μm), the soda-lime and fused silica glasses have a considerable averaged thermal emissivity of ~0.88 and ~0.83, respectively.

Following Equation 4.8, we present, in Fig. 5.3 the radiative cooling results (i.e., operating temperature and efficiency) for the same structures as in Fig. 5.2 and for typical environmental conditions, described in Fig. 5.1, as a function of the heating power, i.e., assuming constant $-P_{sun}+P_{ele,max}$ values in Equation (4.13). The efficiency is calculated by Equations (4.6) and (4.14) at steady-state temperature.

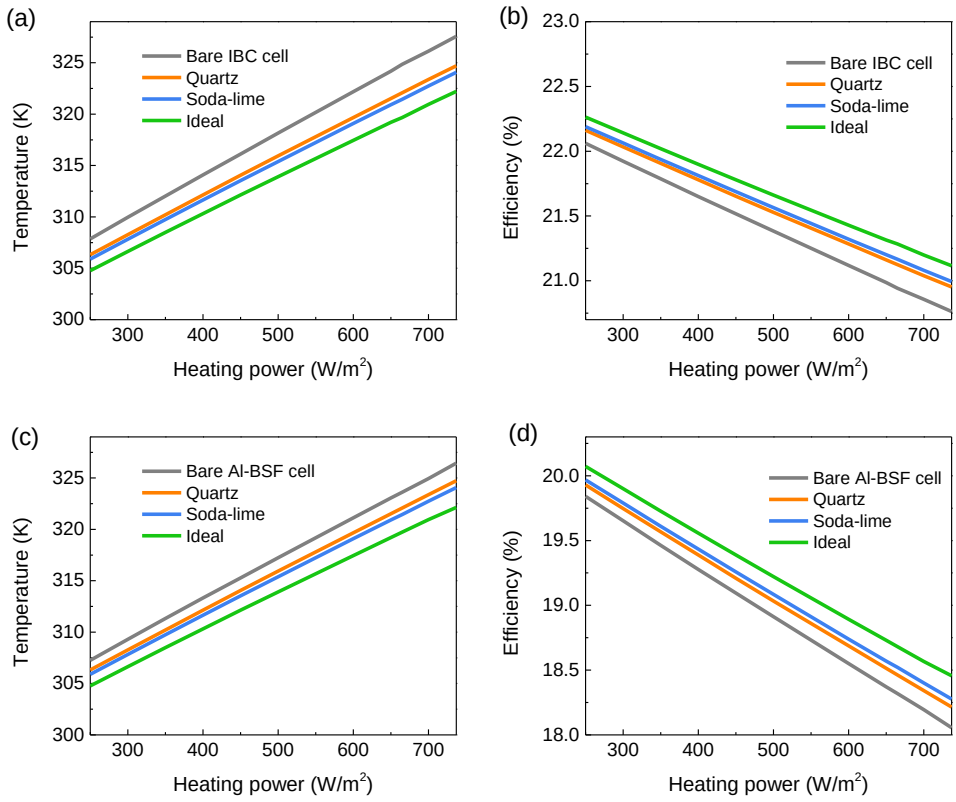

Fig. 5.3: Operating temperature (a), (c) and efficiency (b), (d) of IBC (a), (b) and Al-BSF (c), (d) solar cells with the thermal emitters in Fig. 5.2, as a function of heating power. We assume operation under the AM1.5G spectrum, T_{amb}=300 K, $h_{c,top}$=10 W/m^2/K (υ_{top}~1.25 m/s wind speed [126]*), $h_{c,bottom}$=5 W/m^2/K (υ_{bottom}~0.75 m/s wind speed), ε_{tedlar}=0.85.*

Without any glass on top, the bare cell heats up considerably above ambient temperature (T_{amb}=300 K). On a clear day, under peak (unconcentrated) solar irradiance 1000 W/m^2, corresponding approximately to a heat output of 650-750 W/m^2 (depending also on PV's architecture), the bare cells operate at ~24.1 K (IBC), ~25.8 K (Al-BSF) above ambient. We note that in the case of the bare "Al-BSF" cell, despite its higher hemispherical emittance compared to IBC's (see Fig. 5.2), the increased operating temperature is a consequence of the increased parasitic absorption at 0.28-4 μm. The effect of the increased heat load in Al-BSF cells can be seen in Fig. 5.3 by the increased difference in temperatures in the case of the encapsulated cells (assuming conventional soda-lime glass covers) that operate at ~21.4 K (IBC), ~24.1 K (Al-BSF) above ambient. Moreover, As can be concluded from Fig. 5.3, the impact of a radiative cooler linearly scales up with the solar heating power. Thus, the radiative PV cooling is expected to play a significant role in thermal management of concentrated PV systems (more than 1 sun).

By taking into account the steady-state heating power, i.e., by solving Equation (4.8), for non-concentrated systems, the solar cell with the ideal cooling layer operates at ~5.2 K and ~4.3 K lower temperature compared to the bare IBC and Al-BSF cells, respectively, ~2.4 K (IBC), ~2.6 K (Al-BSF) compared to the encapsulated cells with a fused quartz glass cover, and ~1.8 K (IBC), ~1.9 K (Al-BSF) lower temperature compared to encapsulated cells with the conventional soda-lime glass cover. Corresponding calculated relative efficiency increase $\Delta\eta(\%_{rel})$ equals to ~1.6% compared to the bare–IBC (bare–IBC), ~2.2% (bare–Al-BSF), ~0.8% (quartz–IBC), ~1.3% (quartz–Al-BSF) and ~0.6% (soda-lime–IBC), ~1.0% (soda-lime–Al-BSF). For the "Al-BSF" cell, increased efficiency gain, for almost the same temperature reduction with IBC, arises due to the higher $\beta_{Al\text{-}BSF}$=-0.45%/K (the standard value for the mainstream crystalline silicon cells) compared to β_{IBC}=-0.29%/K (corresponding to commercial IBC solar cells).

The weather conditions are included in our model by considering different combined conduction-convection nonradiative heat transfer coefficients, $h_{c,top}$, in the $P_{cond,conv}$ term of Equation (4.8) and different T_{amb} in the P_{atm} term. For example, in windy conditions $h_{c,top}$ increases. Figure 5.4 shows the outdoor PV operating temperature as a function of T_{amb} and $h_{c,top}$ ($h_{c,bottom}$=5 W/m^2/K, υ_{bottom}~0.75 m/s [126]), as well as the thermal gains [temperature change, ΔT, and relative efficiency increase, $\Delta\eta(\%_{rel})$] arising by the implementation of a blackbody cooler (ideal) compared to the conventional case, i.e., PVs with soda-lime glass covers. The dashed vertical lines in Fig. 5.4 correspond to the most common occurring natural convection conditions that is a wind speed of 0.75 to 4.3 m/s.

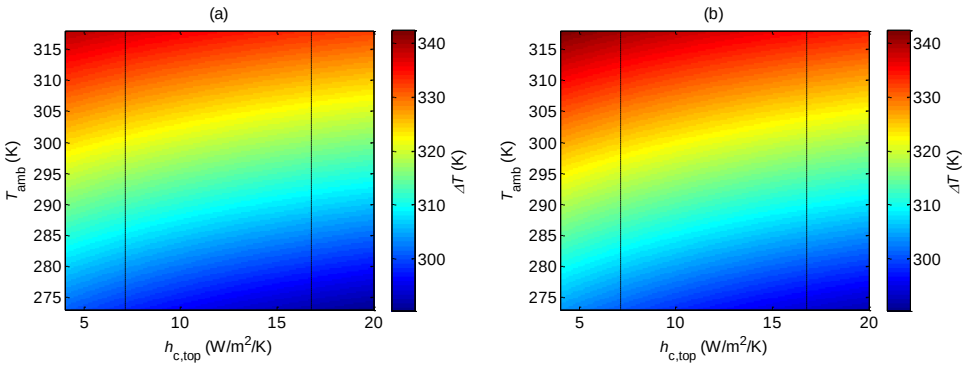

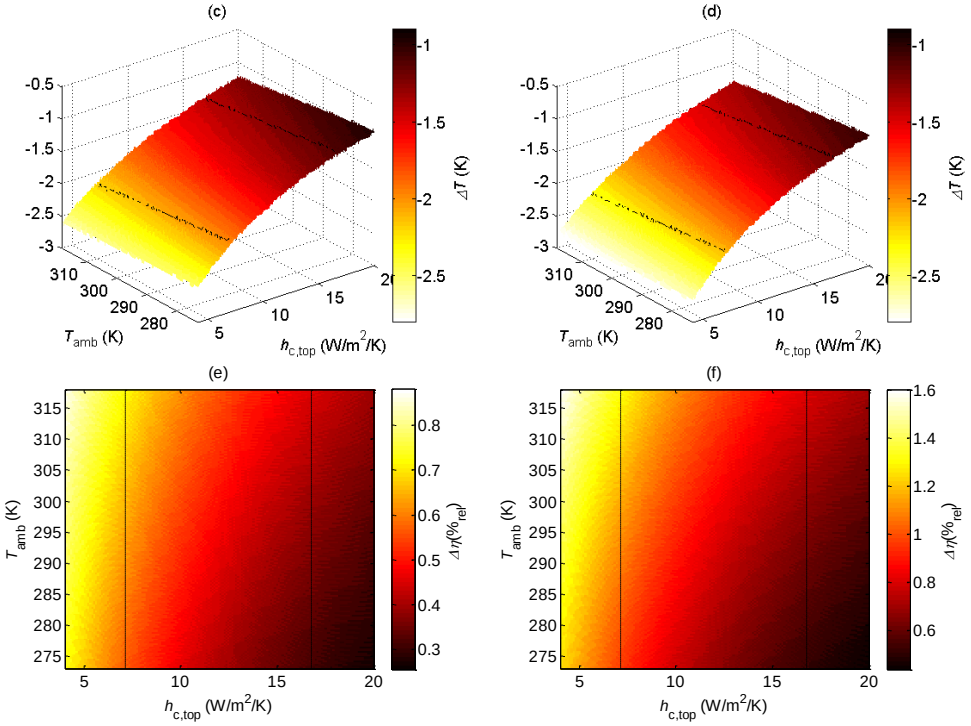

Fig. 5.4: Encapsulated (with EVA, Tedlar and soda-lime glass cover) IBC- (a), (c), (e), Al-BSF-based (b), (d), (f) cells' operating temperature (a), (b), and the corresponding temperature, ΔT, (c), (d) and relative efficiency, $\Delta\eta(\%_{rel})$, change (e), (f) with the implementation of a blackbody cooler (ideal), as a function of the combined conduction-convection nonradiative heat transfer coefficient, $h_{c,top}$, and the ambient temperature, T_{amb}. The dashed vertical lines indicate the most common occurring natural convection conditions that correspond to wind speeds of 0.75-4.3 m/s (where $h_{c,bottom}$=5 W/m^2/K, v_{bottom}~0.75 m/s [126]*).*

It is clear that at severe environmental conditions (high ambient temperature, and low wind speed levels) the PV temperature is expected to reach values even higher than ~330 K [see Fig. 5.4(a) and (b)]. We note that the long-term damage to the polymer EVA-encapsulant during its useful life often occurs at temperatures above 323 K [131]. Providing no further cooling approaches may accelerate EVA damage and thus PV's power degradation significantly. For instance, from Figs. 5.4(c) and 5.4(d), it is also clear that adding radiative cooling with the implementation of the blackbody (ideal) cooler may be particularly important in the case of severe environmental conditions. The positive cooler impact on PV's operating temperature increases as outdoor temperature increases and further increases in a nonlinear manner as h_c decreases. With the ideal cooler the PV temperature reduction may reach values up to ~2.8 K. Indicatively, as discussed in Refs. [132,133], every degree of temperature drop can delay PV module failure, due to thermally activated degradation, by 5-15% depending on the conditions (temperature,

UV light absorption, etc.). Interestingly, efficiency gains are always observed [Fig. 5.4(e) and 5.4(f)], in particular when convective cooling tends to be inadequate. When adding radiative cooling, the efficiency gains reach values of ~0.44 to ~1.6% and ~0.26 to ~0.88% for the Al-BSF and the IBC cell, respectively.

The detailed role of the blackbody cooler in silicon PV modules, was then demonstrated through current-voltage (*J*–*V*) calculations [see Equations (4.1)–(4.5)], and is shown in Figs. 5.5, 5.6 and 5.7.

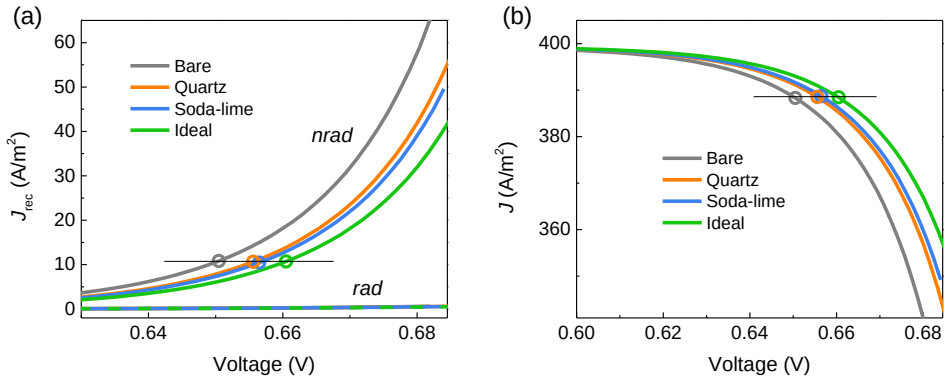

Fig. 5.5: (a) Nonradiative (nrad), radiative (rad) recombination current density (J_{rec}) and the (b) output current density vs. output voltage of IBC PVs that incorporate a fused quartz glass cover (orange) and a conventional soda-lime glass cover (blue) (both 3.2-mm-thick), in comparison with the bare cell (gray line) and the ideal case assuming a blackbody cooler (green line). The circles denote the nonradiative (Auger) recombination current density at the maximum operating power point, V_{mp}, of the solar cell.

In particular, the recombination current density [first two terms in the r.h.s, of Equation. (4.1)] is shown in Fig. 5.5(a), and the output current density in Fig. 5.5(b), for an operating temperature equal to the steady-state temperature arising by solving Equation (4.8), assuming T_{amb}=300 K and a nonradiative heat transfer coefficient equal to $h_c=h_{c,top}+h_{c,bottom}=10+5=15$ W/m^2/K to mimic typical outdoor conditions. The corresponding thermal power radiated by the cooler and the output electrical power are presented in Fig. 5.6(a) and Fig. 5.6(b), respectively. Notice that as the electrical power, of each case, increases the thermal power radiated drops due to heating reduction and the corresponding temperature reduction [see Fig. 5.6(b)]. The lowest radiated power of each case occurs at the maximum power point of the PV. Moreover, at the steady-state the blackbody cooler, as expected, results in operating temperature reduction compared to the bare cell and the two photovoltaic modules, with quartz and soda-lime (conventional) glass covers.

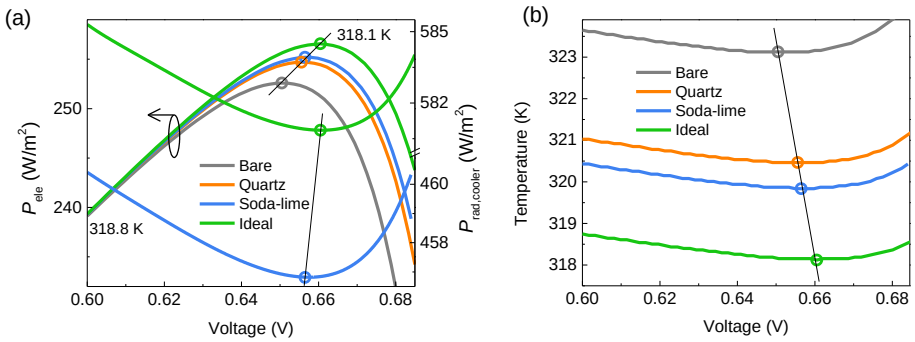

Fig. 5.6: (a) Electrical power output, thermal power radiated and (b) the operating temperature of the device vs. output voltage of IBC PVs that incorporate a fused quartz glass cover (orange) and a conventional soda-lime glass cover (blue), in comparison with the bare cell (gray line) and the ideal case assuming a blackbody cooler (green line). Both (a) and (b) are calculated for the steady-state by solving Equation (4.8). Maximum operating point Vs are marked with circles.

As seen in Fig. 5.6(b), the temperature reduction provided by a blackbody cooler, at the maximum operating point of the PV (*V*s marked with circles in Fig. 5.5 and Fig. 5.6), is equal to 5.0 K, 2.3 K and 1.7 K compared to the bare cell, the quartz-covered and the soda-lime glass covered, respectively. This results in the increase of the open-circuit voltage, V_{OC}, by 1.27%, 0.6% and 0.43%, respectively. The reason behind the V_{OC} enhancement is the higher quantum efficiency, $QE=J_{rad}/(J_{rad}+J_{nrad})$, (see Fig. 5.7). As the temperature decreases, i.e., with the implementation of each cooler, nonradiative (Auger) recombination (J_{nrad}) decreases [see Fig. 5.5(a)], leading to an enhanced V_{OC} and efficiency.

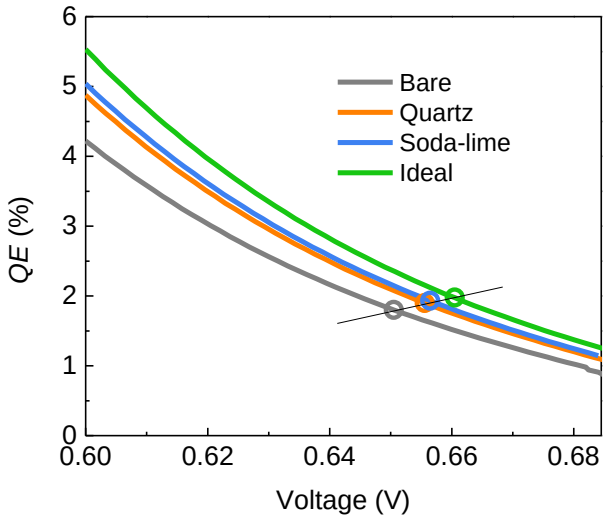

Fig. 5.7: Quantum efficiency, QE, dependence on the output voltage at steady-state [by solving Equation (4.8)] for IBC PVs that incorporate a fused quartz glass cover (orange) and a conventional soda-lime glass cover (blue), in comparison with the bare cell (gray line) and the ideal case assuming a blackbody cooler (green line). Maximum operating point Vs are marked with circles.

Notice also that the impact of the radiative recombination current density (J_{rad}) is much lower than the non-radiative in all cases, in consistence with Refs. [59,96], further validating our assumptions in Section 4.2. We note that any recombination process has a dual impact (see Section 4.2). It results both to a voltage loss (see circles in Fig. 5.5 and Fig. 5.6), because the generation-recombination balance is diminished, and to a current loss (see Fig. 5.5). For this reason, the fill factor *FF* also increases by 0.30%, 0.13%, 0.10%, when we optimize the cooling capability of the PV by employing the blackbody cooler instead of the bare cell, quartz and soda-lime glass cover, respectively. Eventually, the corresponding conversion efficiency is increased by 1.57%, 0.73% and 0.53% in relative terms [see circles in Fig. 5.6(a)].

5.4 FILTERING SUB-BANDGAP RADIATION

Aside from the mid-IR spectral regime, the choice of a cell's architecture has an impact on PV's radiative properties also in the optical sub-bandgap regime, i.e., beyond semiconductor's absorption band ~>1.107 μm, as it is clearly shown in Refs. [16,98,122]. Absorbed sub-bandgap energy photons (from the other than c-Si parts of the cell) increase the thermal load of the device significantly, reducing the efficiency. For c-Si-based PVs, the main factors that affect PV's sub-bandgap reflection is cell's back reflector technology [Fig. 5.8(a)] [98] and the texture steepness both at the usually textured front and rear surfaces of the cell [Fig. 5.8(b)] [122]. Ways for minimizing sub-bandgap absorption are its direct reflection by incorporating photonic structures for example, or the texture steepness reduction. In the second case though, care must be taken since the beneficial absorption in silicon also declines.

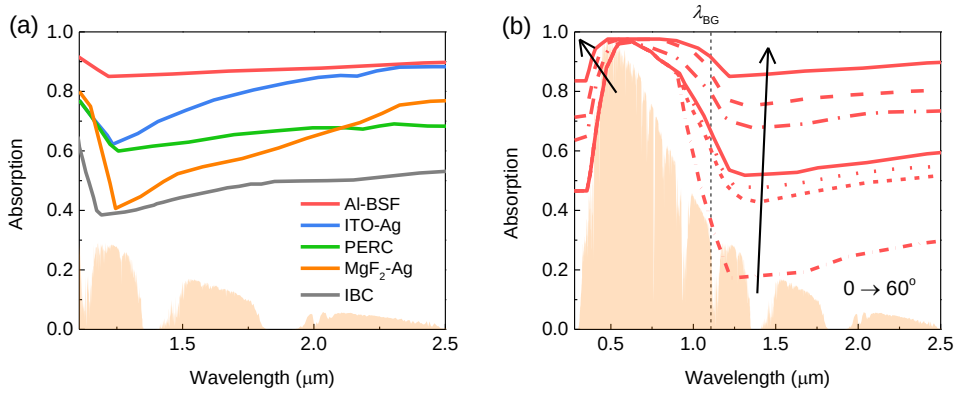

Fig. 5.8: (a) Spectral sub-bandgap absorption of current state-of-the-art solar cells with four different back reflectors [Al-BSF (red), ITO-Ag (blue), PERC (green), MgF_2-Ag (orange)] compared to the IBC cell. Data obtained from [98]. *(b) Dependence on the texture steepness (texture angle: 0–60°) of both front and rear cell surfaces for the first case (Al-BSF) in (a). Data obtained from* [122].

To investigate the detailed impact of sub-bandgap radiation we consider state-of-the-art PV cells and we reduce the heat load firstly by reflecting sub-bandgap radiation and calculate the gain $\Delta\eta(\%_{rel})$ with respect to the operating temperature reduction at typical outdoor conditions (see Fig. 5.9). The results shown in Fig. 5.9 concern the two extremes, i.e., IBC and Al-BSF cells, where we assumed encapsulation with EVA, Tedlar and soda-lime glass covers. The thickness of each of those layers is as discussed in the caption of Fig. 4.8 and in Section 4.5 also shown in Fig. 5.11(a).

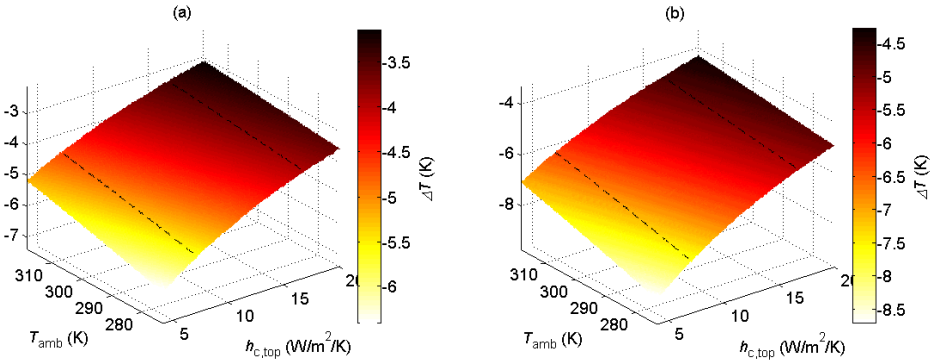

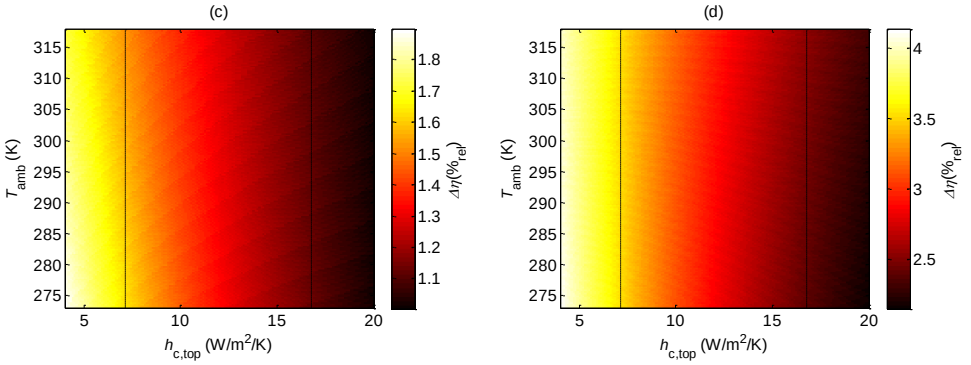

Fig. 5.9: Encapsulated (with EVA, Tedlar and soda-lime glass cover) IBC (a), (c), Al-BSF-based (b), (d) cells and the corresponding operating temperature, ΔT, (a), (b) and relative efficiency , $\Delta\eta(\%_{rel})$,change (c), (d) with the addition of sub-bandgap reflection (1.107-4 μm) (compared to the conventional case without filtering sub-bandgap radiation), as a function of the combined conduction-convection nonradiative heat transfer coefficient, $h_{c,top}$, and the ambient temperature, T_{amb}. The dashed vertical lines indicate the most common occurring natural convection conditions that correspond to wind speeds of 0.75-4.3 m/s (where $h_{c,bottom}$=5 W/m^2/K, υ_{bottom}~0.75 m/s [126]*).*

It is clear that the reflection of sub-bandgap radiation is a highly efficient approach for reducing the operating temperature in crystalline silicon-based PVs, due to the relatively high parasitic absorption from the PV modules at that regime, consistently with Refs. [16,98,134]. Specifically, the temperature reduction and gain reach values of ~3.2-6.4 K and ~1.0-1.9%, respectively, for the IBC cell case, and ~4.3-8.7 K, ~2.1-4.1%, respectively, for the Al-BSF cell. These results indicate that there is still room for improvements in the solar cell technology, taking into account that STC conditions (T=298.15 K) are rarely met in the field. Therefore, the decreasing PV module efficiency with higher temperatures needs to be taken into account when calculating its performance, especially, when considering new technologies like the promising passivated emitter and rear cells (PERC) [135].

Interestingly, contour plots of Fig. 5.9 depict an opposite tendency compared to that of Fig. 5.4 (showing the impact of a blackbody cooler). The impact from adding sub-bandgap reflection slightly declines with increasing ambient temperature. Reflecting sub-bandgap radiation increases the intercept term $-P_{atm}(T_{amb})-P_{solar,heat}$ (assuming a constant $P_{solar,heat}$) in Equation (4.8). When h_c increases, the impact of temperature reduction and gain decreases in a non-linear manner, which is consistent for both cases.

Reducing the texture steepness resulted to a device temperature reduction by ~1 to 10 K but the absolute efficiency also declines by ~0.1 to 2.4% due to the absorption degradation also at the beneficial spectral wavelength range (~≤1.107 μm). The related results are shown in Fig. 5.10.

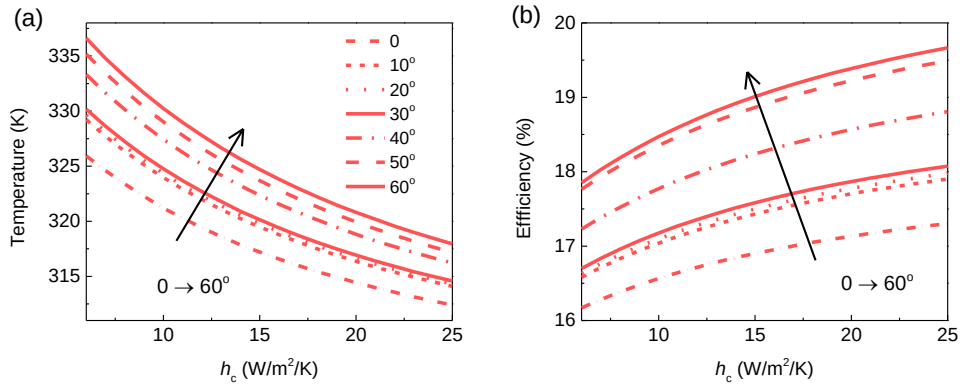

Fig. 5.10: (a) Temperature, (b) efficiency dependence on the texture steepness (texture angle: 0–60°) of both front and rear cell surfaces for the encapsulated Al-BSF cell case at T_{amb}=300 K.

5.5 FILTERING ULTRAVIOLET RADIATION

Photovoltaics are currently the fastest-growing solar technology [6]. Still, to be economically viable, they need to operate consistently at outdoor conditions and to be reliable for at least 25 years [136,137]. A commercial PV's degradation is mainly attributed to the degradation of the eminent polymer encapsulant ethylene-vinyl-acetate (EVA) copolymer, employed as adhesion layer/layers between the cells [see Fig. 5.11(a)]. The photochemical processes caused by light, such as photodegradation, lead to the alteration of the primary structure of the polymer, due to the breaking of the chemical bonds in its main chain, initiating unwanted reactions [131]. Such photochemical processes are a major material-degradation factor resulting even to reduced transmission from the EVA (yellowing) and thus harming PV's performance significantly [138]. As with most photochemical processes, the reaction rates depend on the wavelength, intensity of incident light, as well as the temperature.

Ultraviolet (UV) radiation has been identified as the most critical factor for the degradation of photovoltaics [131,138,139]. High energy UV photons (0.28–0.4 μm) can break chemical bonds in the main chain of the EVA-polymer as well as cause damage to the front surface of the silicon layer (i.e., defects, acting as recombination traps). As such, UV-originated cell and encapsulant degradation comprise the highest fraction (up to an even ~70%) of the 25-year power degradation [139] of PVs (assuming a standard 25-year warranty of less than 20% power loss).

Moreover, high energy UV photons (~0.28-0.4 μm) result in significant heat dissipation (often called thermalization losses [94], see also Section 4.2) that increases the PV temperature and thus decreases its efficiency, at least for silicon-based PVs; this is due to the excess of the UV photon energy relative to the semiconductor's bandgap energy.

Therefore, several approaches have been emerged for blocking UV light. The most common approach is employing UV absorbers which are either photoactive chemicals (having though finite lifetimes due to photothermal oxidative degradation), or low iron (Fe) glasses [140] doped with cerium (Ce) (which are subject to oxidation, leading to absorption also of other beneficial parts of the spectrum and thus to PV performance reduction [131]). A more direct solution, by Kempe et al. [140] and Li et al. [16], is the utilization of antireflection coatings to reflect UV light.

However, reflecting UV light leads also to reduced light transmission inside the cell resulting in less photocurrent and thus to a negative impact on the PV efficiency. Given the above, it is essential to examine and evaluate the currently unexplored total impact of the UV spectrum (wavelengths from ~0.28-0.4 μm) on the efficiency of a solar cell considering all UV associated and competing effects, i.e., the increase of the photocurrent and the increase of the temperature (due to the high thermalization losses in the cell and the high parasitic absorption from EVA encapsulant).

In this respect, in the present study we consider realistic commercial crystalline silicon IBC PVs (among the ones that are currently in the market of solar cell technology [88]) and evaluate in detail the total impact of the UV radiation on the PV efficiency, as we have thoroughly discussed also in Ref. [84]. For this evaluation we employ the thermal-electrical co-model described in Chapter 4, which calculates the solar cell steady-state temperature (for a given incident power, materials, and environmental conditions), as well as its efficiency as a function of temperature, taking into account all the major intrinsic processes affected by the temperature variation. These processes include the material-dependent radiative and non-radiative-Auger recombination of electron-hole pairs, which is a major cause for the voltage decline and the subsequent efficiency decrease of PVs operating at elevated temperatures. Employing our model, we explore the impact of the UV radiation (on the PV temperature and efficiency) by gradually reflecting it (by 100%), starting from a wavelength equal to 0.28 μm - where the highest thermalization losses occur, up to a given, critical wavelength λ_r, and we evaluate the critical wavelength λ_r as to achieve maximum temperature reduction and maximum efficiency.

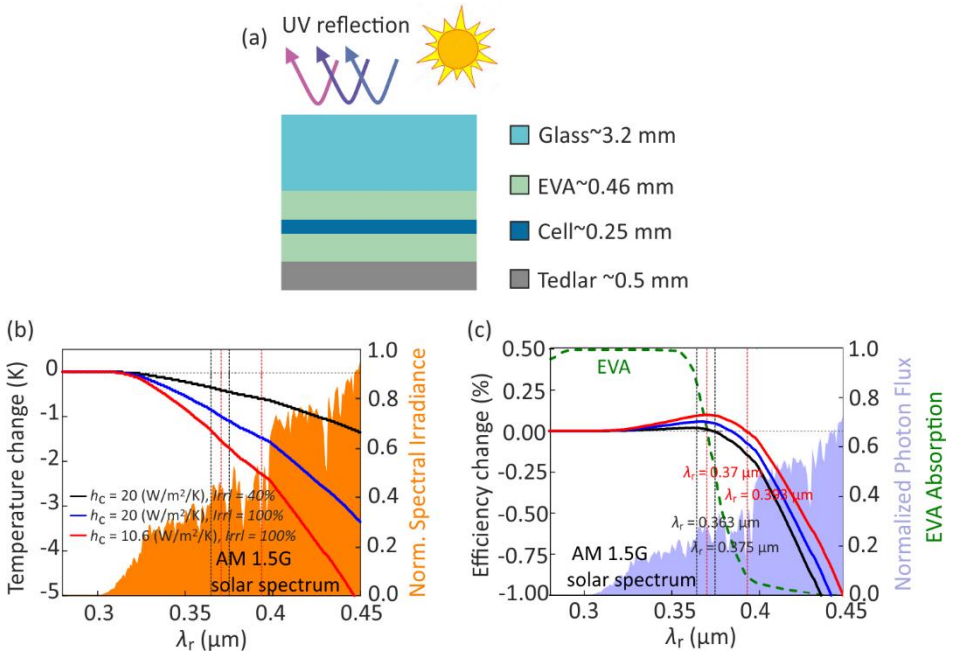

Fig. 5.11: (a) Schematic of the silicon-based PV module investigated in this work showing the different layers along with their thickness. The material parameters and the absorptivity/emissivity data of the PV module in the optical spectral range are the same as in Ref. [141]. *(b) PV temperature and (c) efficiency change associated with the reflection of the incident UV radiation for the system of (a), for a reflection wavelength range from 0.28 μm to* λ_r. *For all cases, the ambient temperature is equal to 298 K. To mimic typical outdoor conditions, we assume an irradiance level (Irrl) of 40% (of the "AM 1.5G" standard sunlight spectrum* [55]*) and a combined nonradiative heat transfer coefficient,* h_c, *equal to 20 W/m*^{2}*/K (black lines), Irrl=100%,* h_c*=20 W/m*^{2}*/K (blue lines), and Irrl=100%,* h_c*=10.6 W/m*^{2}*/K (red lines). The green dashed line in (c) indicates the EVA absorption. The two black/red dashed vertical lines correspond to two different* λ_r *of 0.363/0.37 μm and 0.375/0.393 μm, where we observe the maximum efficiency improvement and the limiting point, where the efficiency remains unharmed for the conditions of the black/red curve case. The orange and blue filled areas in (b) and (c) correspond to the normalized "AM1.5G" standard sunlight spectral irradiance and photon flux, respectively.*

Figure 5.11 shows the PV temperature change [Fig. 5.11(b)] and the PV efficiency change [Fig. 5.11(c)] resulting from total reflection of the solar energy from 0.28 μm to a parameter (critical) wavelength λ_r, as λ_r varies from 0.28 μm to 0.45 μm, i.e., covers all the emitted by the sun UV spectrum. For the temperature and efficiency calculations, we assumed that the PV operates at outdoor conditions, with T_{amb}=298 K. To capture the effect of the variant environmental conditions we assume three different cases, (i) an irradiance level (*Irrl*) of 40% (of the "AM 1.5G" standard sunlight spectrum [55]) and a combined conduction-convection nonradiative heat transfer coefficient, h_c, equal to 20 W/m^2/K (black curves), a value corresponding to strong wind climates, (ii) *Irrl* =100%, h_c=20 W/m^2/K (blue curves), and (iii) *Irrl* =100%,

h_c=10.6 W/m^2/K (red curves), i.e., weak wind climates. The orange and blue areas in Fig. 5.11(b) and Fig. 5.11(c) correspond to the normalized "AM1.5G" standard sunlight spectral irradiance and photon flux respectively and the green dashed curve in Fig. 5.11(c) indicates the EVA absorption.

As seen in Fig. 5.11(b), reflecting incident radiation always leads to a temperature reduction (compared to the primary PV, i.e., without UV reflection), as expected. Interestingly though, reflecting UV radiation up to a specific wavelength leads to an increase (~0.1%) rather than a decrease of the PV efficiency, despite the reduction of potential carriers. For instance, in Fig. 5.11(c), for 0.28–0.39 μm, the efficiency change obtains positive values in the red curve case. In other words, the detrimental impact of the high EVA absorption [green dashed line in Fig. 5.11(c)] in this regime and of the thermalization losses seem to overcompensate the positive impact of the additional potential carriers generated by the UV [see the blue area in Fig. 5.11(c)].

Moreover, the impact of reflecting certain UV wavelengths on the device's temperature and efficiency varies for each of the different cases depicted in Fig. 5.11, due to the alteration of the environmental conditions that affect the power-temperature relation and thus the steady-state operating temperature (see Section 4.2) [141]. Climates with lower wind speeds, e.g., h_c <13 W/m^2/K, are expected to allow higher cut-off wavelength λ_r and hence higher temperature reduction. For instance, assuming a broader reflection wavelength range, with λ_r =0.393 μm [see right vertical red line in Fig. 5.11(b) and Fig. 5.11(c)], the PV could operate at an up to ~2.3 K lower temperature compared to λ_r =0.37 μm, but its performance is not sacrificed only for the h_c =10.6 W/m^2/K, *Irrl* =100% case [where the efficiency change remains positive as seen in Fig. 5.11(c) - red curve]. In implementing a practical approach, though, to cut parts of the UV spectrum, given that λ_r can be specified only during the manufacturing procedure, it is essential to calculate a λ_r which will be robust in respect to the variant environmental conditions as well as the various characteristics of commercial PVs.

Next, we calculate such a constant/fixed cut-off reflection wavelength, λ_r, for T_{amb}=298 K, h_c =20 W/m^2/K, and a lower irradiance level (40% of the "AM 1.5G" standard sunlight spectrum [55]), which is the worst-case scenario studied (black curves of Fig. 5.11). Calculating λ_r by requiring maximum temperature reduction (without harming efficiency) we obtain λ_r =0.375 μm; requiring the maximum possible efficiency increase (for the above-mentioned environmental conditions) the resulting cut-off reflection wavelength is λ_r =0.363 μm.

Figure 5.12 presents the impact of the UV reflection on temperature [Fig. 512(a)] and efficiency [Fig. 5.12(b)] for a PV operating outdoors for different, typical environmental conditions, i.e., as a function of the combined conduction-convection coefficient. The UV reflection is the total reflection (i.e., 100%) in the wavelength range from 0.28 μm up to the two cut-off reflection wavelengths λ_r specified above (solid curves correspond to λ_r =0.363 μm, assumed for maximum efficiency, and dashed-dotted curves correspond to λ_r =0.375 μm, assumed for maximum temperature reduction). Additionally, in Fig. 5.12 we examine the impact of the UV reflection on the PV temperature and efficiency for thicker silicon layer (W=500 μm – black), higher T_{amb} (313 K - purple), and an irradiance level 100% (*Irrl*=100% – red) and a much lower one (*Irrl*=40% – orange).

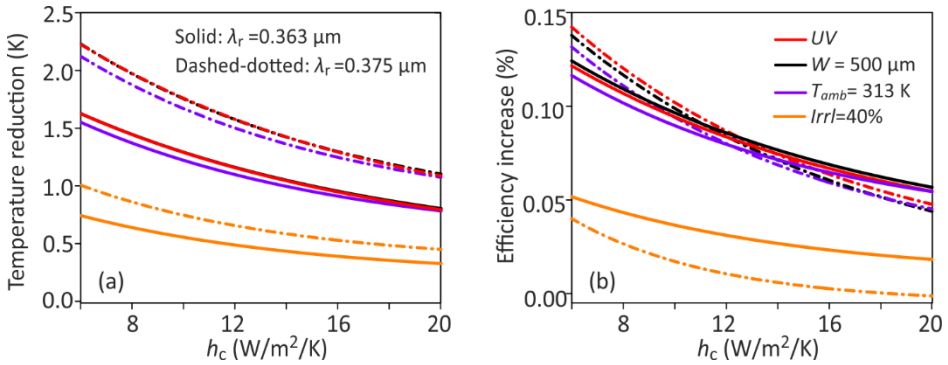

Fig. 5.12: (a) PV temperature reduction and (b) efficiency increase associated to the reflection of the incident UV radiation for a wavelength range from 0.28 μm up to λ_r=0.363 μm (solid lines) and λ_r=0.375 μm (dashed-dotted lines) for ambient temperature T_{amb}=298 K, in respect to the nonradiative heat transfer coefficient, h_c, for the system of Fig. 5.11(a). The figures show the impact of the UV reflection for an irradiance level (Irrl) 100% (UV – red lines), and a much lower one (Irrl=40% – orange lines), and for different PV characteristics, like higher silicon thickness (W=500 μm – black lines), T_{amb}=313 K (purple lines).

As seen in Fig. 5.12, reflecting UV radiation up to λ_r =0.375 μm leads to an efficiency increase by up to ~0.15% [dashed-dotted red in Fig. 5.12(b)]. Additionally, the temperature reduction compared to the primary PV, i.e., without UV reflection, can reach values up to ~2.2 K [dashed-dotted red in Fig. 5.12(a)]. Assuming a narrower reflection wavelength range (λ_r =0.363 μm) results in slightly higher efficiency [compared to the λ_r =0.375 μm case - see solid and dashed-dotted lines in Fig. 5.12(b)] for more windy climates (h_c >13 W/m^2/K), but with slightly (up to ~0.5 K) higher operating temperature [see solid and dashed-dotted curves in Fig. 5.12(a)]. Moreover, as seen in Fig. 5.12, the results are robust, even for different PV or environment characteristics met in commercial PVs operating outdoors. The PV operating

temperature can be reduced by up to ~2.2 K [see Fig. 5.12(a)], taking into account all cases, due to the UV reflection, without decreasing the efficiency [see Fig. 5.12(b)]. We expect an even higher impact from UV reflection in PVs with high electrical-power - temperature coefficients (common value of ~-0.45 %/K), as well as in top contact solar cells, where there is additional parasitic absorption from the metallic top contacts (thus higher room for heat elimination), in concentrated systems and space photovoltaics, and in PVs with lower than unity internal quantum efficiencies [142] (collected carriers - absorbed photons ratio) in UV.

6

TOWARDS REALISTIC IMPLEMENTATIONS

6.1 INTRODUCTION

Following the first demonstration of photonic daytime radiative cooling, by Raman et al. [51] in 2014, appropriate passive radiative coolers were designed compatible with PV systems, mainly Si-based PVs, that allowed above-ambient radiative cooling through enhanced thermal emission in the mid-IR [15,71–73], but at the same time increased the visible light transmission towards the PV cell. Zhu et al. [73] theoretically examined a relevant microphotonic design; a two-dimensional (2D) square lattice of silica pyramids (20 μm depth, 4 μm periodicity) and a 100-μm-thick uniform silica layer, on top of a bare undoped silicon wafer. This photonic thermal emitter nearly approached the maximal radiative cooling capability for solar cells, resulting to a temperature reduction of 17.6 K compared to the bare silicon and 4.5 K compared to a silicon covered by a 5-mm-thick uniform silica. Moreover, due to its small thickness compared, e.g., to the 5-mm-thick silica cooler, the pyramid does not reduce solar absorptivity in silicon (related to the non-negligible amount of absorption in the solar wavelength range for a realistic thick glass). Later, Zhu et al. [15] fabricated a 2D photonic crystal (PC) on top of a solar absorber (with a structure that emulated the behavior of a real silicon solar cell) which consisted of periodically placed air holes (~10 μm depth, ~6 μm periodicity – using photolithography) of non-vertical sidewalls in silica. The nonvertical sidewalls of the holes resulted in a gradual refractive index change which provided effective impedance matching between silica and air over a broad range of thermal wavelengths that persisted even for large angles of incidence. Moreover, this visibly transparent thermal black-body led to the increase of the absorbed solar power in silicon due mainly to the enhanced transparency from the top surface. A temperature

reduction of 1.3 K was reported compared to the flat silica. Assuming no increase of solar absorption with the implementation of the photonic cooler, the temperature reduction could reach values of ~2.8 K on average.

Both photonic coolers described above demonstrated remarkably enhanced emissivity in the mid-IR compared to flat silica; still, their manufacturing scalability may be an issue. Jaramillo-Fernandez et. al [72], in 2019, proposed an inexpensive solution for the cooling of buildings, helping to reduce the global-energy consumption due to refrigeration. A novel method of sedimentation based on vertical deposition was used to grow a scalable, thin, 2D colloidal cooler comprised of silica microspheres (~8 μm diameter) self-assembled on a soda-lime glass. This above-ambient radiative cooler on top of a silicon slab was placed inside a polystyrene box to minimize conduction losses and lateral convection, and temperature measurements were conducted outdoors. The temperature of the silicon wafer was found to be 14 K lower during daytime when covered with the cooler, reaching an average temperature difference of 19 K when the structure is backed with a silver layer. In comparison, the soda-lime glass reference used in the measurements lowered the temperature of the silicon by just 5 K. The results of Ref. [72] indicate the significance of passive radiative cooling and the potential for reducing the global-energy consumption by utilizing scalable radiative cooling approaches; however, despite the use of silicon, they are not directly related to solar cells where air convection is vital due to the increased thermal load. In addition, the reflection introduced by the closely packed silica spheres slightly reduced the transparency in the optical range, implying reduced photocurrent and hence potentially deteriorated efficiency in the case of solar cells.

To address this issue, Linshuang Long et. al [74] proposed a photonic cooler comprising of well-designed silica pillar-micro-gratings with a simplified structure as solar-transparent and radiatively cooling thin coating for solar cells. The well-designed grating, with a total thickness of 3.1 μm (2.3 μm pillar height – fabricated with plasma-enhanced chemical vapor deposition, photolithography, and reactive ion etching processes) when placed on top of a doped silicon wafer increased Si absorptivity through anti-reflection, yielding a ~18.7 % absorption enhancement in the optical regime. Additionally, spectrometric measurements showed that the SiO_2 micro-gratings atop doped silicon wafer could remarkably enhance the infrared emittance within the atmospheric window. The maximum temperature decrease provided by the micro-grating coating compared to the bare doped silicon was approximately 2 K, despite the increased solar absorption, and ~0.5 K compared to the silicon covered with a flat silica film case. Recently,

Cho et al. [143] proposed a scalable, on-chip, thin radiative cooler. To achieve high and broadband thermal emission, they fabricated hexagonally arrayed (8 μm pitch) holes (7 μm deep, 6 μm diameter), realized by submicron-thick (0.5/0.3 μm) SiO_2/AlO_x double shells resulting to a hollow cavity film. When placed on top of a silicon wafer, the film exhibited a large emissivity, of ~0.8 at omnidirectional incidence (0−80°), as well as >0.73 Si absorptivity, yielding a ~19 % solar absorption enhancement compared to a bare Si wafer. Finally, Wei Li et al. [16] proposed a 1D photonic crystal consisting of 45 alternate Al_2O_3, SiN, SiO_2, TiO_2 thin-film layers that could be implemented as a retrofit to current photovoltaic modules. This photonic coating layer was designed to be placed on top of a PV and simultaneously reflect part of the solar spectrum that does not contribute to the photocurrent, i.e., the UV, sub-bandgap parasitic absorption, and further enhance the beneficial optical absorption and the thermal emission in the mid-IR. This combined approach is particularly important, since the infrared performance of common antireflection coatings that only increase PV's transmissivity [122], and hence do not provide sub-bandgap reflection, may have detrimental thermal effects [123]. With the structure of Wei Li at al., the perspective of PV-coolers with a double-role has been demonstrated; both increasing the solar cell optical absorptivity and also reducing the operating temperature of the device up to ~5.7 K [16].

As concluded from the above, despite the fact that radiative cooling strategy seems appealing to lower the PV temperature, still its impact on realistic PVs is not clear and quantified. Previous studies described examine solar absorbers emulating the behavior of a silicon solar cell rather than actual commercial PVs, where also the transformation of part of the solar energy to electrical energy or its loss via other mechanisms or in other PV encapsulants has to be taken into account. Moreover, the enhanced thermal emittance of soda-lime glass (often utilized as a cover glass in PVs) compared to silica is not taken into account, neither a photonic-cooler's impact on the efficiency rather than on only the temperature of a commercial PV. Several studies conclude that the key to achieve economically feasible radiative cooling and performance enhancement in PVs is to pursue additional improvements, e.g., to employ cost-friendly materials with high hemispherical emittance and optical transparency [16,61,144]. Yet, not many studies examine this direction and provide quantitative results [145,146], i.e., towards efficiency enhancement in realistic commercial solar cells. Additionally, most currently proposed radiative coolers consist of a micro-structuring that is often sub-optimal for other spectral regimes besides 8-13 μm, such as 0.3–1.1 μm, where a much smaller structuring size is required.

In this chapter, we apply the theory presented in previous chapters in the case of realistic photonic coolers to evaluate their impact on realistic commercial crystalline silicon-based PV architectures. In doing that, exploiting the proposed coupled electro-thermal modeling described in Section 4.2, we quantify and distinguish the thermal and optical efficiency gains and the negative heat impact on PVs' efficiency by implementing each of the proposed radiative coolers. The main aims of the photonic coolers' design optimization process were the reduced complexity and fabrication feasibility on one hand, and on the other hand to enhance the cooling gain that arises by the photon management both at the optical regime (i.e., by reflecting sub-bandgap and UV radiation and further enhancing beneficial optical absorption) and at the thermal mid-IR wavelengths (~4-33 μm).

With the above goals in mind, in the first part of this chapter (Sections 6.2 and 6.3), we seek to improve the radiative cooling through the utilization of 2D photonic crystal (PC) slabs (i.e., 2D periodic structures of finite height - see Chapter 2). This way, the complexity of the experimental realization may be reduced (compared for example to more complex 2D or 3D PCs) as well as a variety of fabrication techniques (i.e., photolithography and reactive ion etching processes, direct ultrafast laser nano/micro-structuring, plasma-enhanced chemical vapor deposition) may become available, providing structures even with an increased durability [15,73,74,85,147,148]. Both of these requirements (reduced complexity and increased durability) are essential for the potential implementation in PVs. The 2D PCs employed here consist of three promising radiative cooling materials, namely fused silica, soda-lime glass and polydimethylsiloxane (PDMS).

In the second part of this study (Section 6.3), we incorporate at the PV systems one-dimensional PC (i.e., multilayer) solar (UV/sub-bandgap) reflectors, which also enhance the beneficial optical absorption by increasing the visible light to go through and reach the PV cells at ~0.367-1.107 μm. To maintain simplicity, the maximum 1D PC layers' number is ≤20, demonstrating even an efficient radiative cooler/reflector consisting of only 10 layers. An advantage of the 1D PCs is that they can be implemented as a PV coating and hence do not require any modification of the standard encapsulated cells. The chosen materials comprising the 1D PCs are common non-absorbing materials in the optical regime (~0.367-2.5 μm), already utilized in solar cell applications, with a high index contrast (see Section 6.3).

Finally, in the last part of this chapter (Section 6.4), we demonstrate a thin, simple, single-material (glass), scalable photonic scheme/cooler design, comprising of properly superimposed 2D micro- and nano-gratings. This thin radiative cooler when placed on top of a doped Si wafer results to both

enhanced solar absorption efficiency and enhanced thermal radiation emission, considerably larger compared to that achievable through the previously reported approaches in literature. Cooler's impact on realistic solar cells was also examined, surpassing any previously reported results in the literature.

6.2 PHOTONIC/PHONONIC BACKGROUND: THE ORIGIN OF THE EMISSIVITY ENHANCEMENT

The aim of this section is to study the physical mechanisms related to the emissivity enhancement that can be provided by the periodic patterning of the glass surface of the encapsulated cell, i.e., the formation of a grating. As already discussed in Section 3.3, for bulk polar materials the electromagnetic propagation inside the polaritonic bandgap (between ω_{LO} and ω_{TO}) is forbidden. Taking advantage of the flexible tunability of the lattice resonances in gratings (for the appropriate choice of the grating's periodicity [see Equations (2.12) and (2.14)]), surface states at frequencies within polar-materials' polariton gap (surface phonon polaritons) can couple to propagative waves in the far-field, hence enhancing the thermal radiation emission.

To analyze and illustrate the emission enhancement by periodic gratings imprinted on glass we employ gratings of 1D periodicity for simplicity. The simplest grating case that can be considered is a surface with a pure sinusoidal modulation, that is $f(x) = hsin(k_{gx}x)$ (see Fig. 6.1), where h is the amplitude (or height) of the modulation, and $k_{gx} = 2\pi/\alpha$ is the primitive reciprocal lattice vector. Following the dispersion relation of SPhPs (surface phonon polaritons) [for the unperturbed case (in the planar surface limit), see Equations (2.12) and (2.14)] and RAs (Rayleigh anomalies) the optimal periodicity was set at 8 μm for which the surface states, i.e., the resonances provided by the periodic patterning/grating, were located inside the polariton gap. (We note though that even if there is no momentum restriction on coupling to radiation, radiative coupling may still be unallowed or inefficient [38].) Figure 6.1(a-e) shows the emissivity for TM-polarized light (incident electric field perpendicular to the grooves) for varying amplitudes of 0 (flat case), 0.3, 0.6, 0.75 and 1.0 μm of the sinusoidal grating, respectively, as a function of incident photon frequency and of the component of the wavevector parallel to the surface in the x-direction (see top left inset of Fig. 6.1). The parallel wavevector is given by $k_{//} = (2\pi/\lambda_0)sin\theta$ where θ is the angle of incidence from the normal. To elucidate the emissivity changes when we

apply the surface modulation, we also plot the dispersion relation of the SPhP (white dashed lines – m=±1,2, where m is the number of the relevant spatial harmonic) and RA modes (red dashed lines – m=±1), given by Equations (2.12) and (2.14).

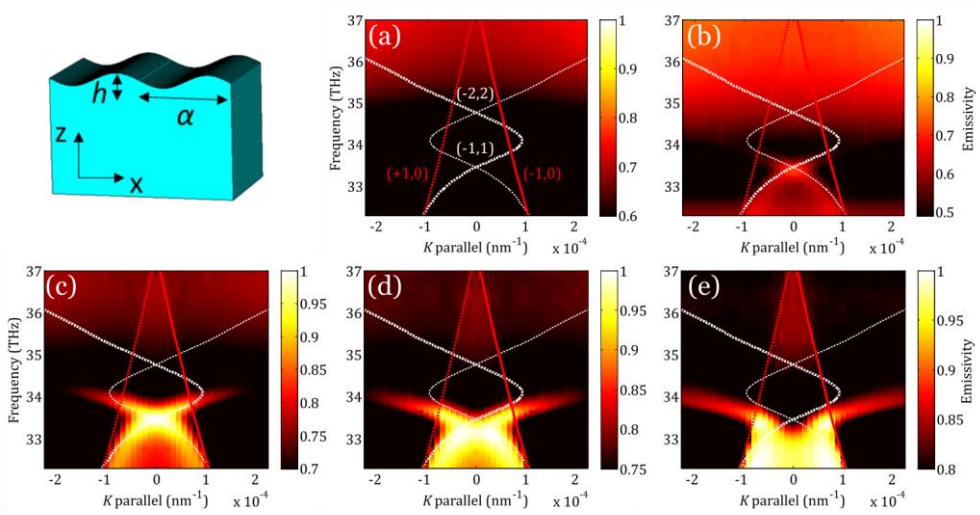

Fig. 6.1: (a) Calculated emissivity for (a) h=0 μm (flat), (b) h=0.3 μm, (c) h=0.6 μm, (d) h=0.75 μm, (e) h=1.0 μm as a function of frequency in THz and in-plane wavevector. The top-left inset shows the picture of the grating that is a surface with a pure sinusoidal modulation.

For the case of flat silica [Fig. 6.1 (a)] there is no coupling to any surface mode, as it is expected, since, there is not enough momentum. For h=0.3 μm up to even h=0.75 μm [Fig. 6.1(b-d)], the grating can be considered a slight perturbation of the planar interface. This can be verified by the electric field distribution (real part of E_z component) shown in Fig. 6.2(a) where the characteristic SPhPs' electric field oscillations parallel to the interface are depicted. As a result, the resonant SPhP wavelengths that manifest as an absorptivity/emissivity peak inside the polariton gap are very close to those calculated from Equation (2.13).

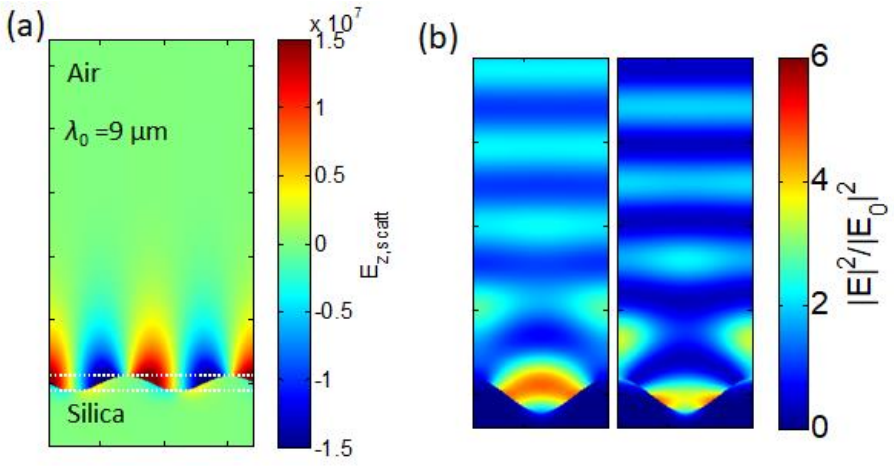

Fig. 6.2: (a) Scattered field at λ_0=9 μm and θ=0° for the h=0.6 μm case in Fig. 6.1. (b) Normalized (relative to the incident field, $\mathbf{E}_0$) distribution of the squared amplitude of the electric field, at λ_0=9.3 μm and θ=0° (left), λ_0=9.0 μm and θ=0° (right) for the h=1.0 μm case in Fig. 6.1.

We note that the required scattering of the second order (m=±2) SPhPs must be a $2\cdot k_{gx}$ event. On purely sinusoidal gratings, which possess no $2\cdot k_{gx}$ Fourier component in their grating profile, this scattering process is mediated by multiple scattering events, which are very weak. Since this scattering amplitude is so weak, no emissivity enhancement (compared to the flat) takes place for the ±2 scattered SPhPs. Furthermore, as the grating's amplitude gradually increases, the coupling of the localized edge modes associated to the individual microgrooves [see the localized fields at the microgrooves edges in Fig. 6.2(b) (right)] to the two RAs yields the left and right resonances (see red lines in Fig. 6.1). (We note that the amplitude dependence is also related to the conducting substrate influence which may introduce coupling between the microgrooves, suppressing both LSPhRs and RAs [149].)

The results in Figs. 6.1, 6.2 highlight the existence and hybridization of two types of resonances in silica gratings, which have been identified in the literature for the case of the similar in behavior metallic gratings in the optical regime [150]. One type of resonance is primarily an SPhP with the E-field as shown in Fig. 6.2(a) for example. The second type concerns localized resonances with fields confined at the array elements' edges [see Fig. 6.2(b) (right)]. When these resonances are tightly confined and do not hybridize with the SPhP-type resonances, they are characterized by flat (dispersionless) bands in the ($k_{//}$, ω) photonic band diagram of the periodic structure [150]. In other words, the position of the corresponding spectral emissivity feature does not depend on the incidence angle. Intermediate scenarios where the localized modes hybridize with the SPP-type resonance leading to dependence of the

emissivity peak on the incidence angle are seen in Fig. 6.1(c-e) for example. As a result, the low emissivity at ~8-9.5 μm (polariton gap), associated to silica's phonon-polariton excitation [see, e.g. Fig. 6.1(a)], is significantly suppressed even with a simple sinusoidal modulation due to the multi-resonance excitation and coupling of the surface modes [see Figs. 6.1(d-e)].

Aside from periodic patterns that sustain waveguide-type modes, deep subwavelength periodic structures may also be important for passive radiative cooling, depending also on the material properties. The main reasons are that: i) they sustain localized modes associated with high local fields in the vicinity of the array elements, resulting in increased absorptivity/emissivity (see also Section 2.6). This follows directly from Poynting's theorem for power dissipation [14] [$A \sim |\boldsymbol{E}|^2$]. ii) Localized modes are characterized by flat (dispersionless) bands, i.e., they show no dependence on polar angle (note that the realistic radiative cooling through the atmosphere is affected by both the glass real spectral emissivity and by the decline of glass emissivity with polar angle). iii) Lossy localized modes may provide broadband wavelength coupling (many radiative loss routes, i.e., scatter light to various directions).

6.3 COMPARATIVE STUDY

In this section, we propose and evaluate realistic photonic coolers and examine how close the realistic implementations can come to the maximum potential of the radiative thermal management in commercial solar cells, i.e., how close to the ideal implementation of simultaneously all the cooling approaches described in previous chapters. Several photonic cooler designs suitable to solar cell applications have been analyzed. Here, for our comparative analysis we discuss the five most promising ones, which we name as *S1* (S: silica), *G1* (G: soda-lime glass), *P1* (P: PDMS), *S2* (S: UV, sub-bandgap), *U2* (U: UV), and we highlight and distinguish the gain that arises in one case mostly by the photon management at the mid-IR [i.e., case (1): *S1*, *G1*, *P1*] and in the other case at the optical regime [i.e., case (2): *U2*, *S2*].

S1 cooler is a 2D photonic crystal slab on top of the PV [i.e., on top of the encapsulated cell with the EVA (0.46-mm-thick) and glass (3.2-mm-thick) wafers] which consists of 2D periodically placed stripes in silica (2.2 μm depth, 2.0 μm width, 8 μm periodicity) [see left top structure of Fig. 6.3(a)]. The 2D crystal lattice diffracts the SPhPs into the far field for both TM and TE polarizations (see Section 6.2), resulting to a high emissivity window at 8-13 μm [see Fig. 6.3(c)] that persists even for large angles of incidence [see Fig. 6.3(d)]. This visibly transparent thermal black-body leads also to a slight

increase of the absorbed solar power in silicon due mainly to the reduced reflectivity from the top PV surface [see Fig. 6.3(b)]. Moreover, the sparse periodic placement of silica stripes suppresses detrimental scattering effects that could increase PVs reflectivity in the optical range.

G1 cooler consists of deep-sub-wavelength periodically placed cylindrical pillars in soda-lime glass on top of the PV (2.2 μm depth, 65 % filling factor, 1.2 μm periodicity) [see right top structure of Fig. 6.3(a)]. The high local fields associated to the sub-wavelength pillars in conjunction with soda-lime glass enhanced absorption result to an almost ideal emissivity enhancement and to a much better angular response than *S1*. The optical response is also improved compared to *S1* [see red versus green line in Fig. 6.3(b)]. The presence of the micron-pillars induces a gradual transition of the effective index from air to soda-lime glass that yields an improved impedance matching [147,151].

P1 is a two-layer polymeric structure that could potentially constitute a very promising PV radiative cooler due to its simplicity [see bottom structure in Fig. 6.3(a)] [145]. A thicker polymeric layer (~100 to 200 μm thickness) is responsible for the thermal emission in mid-IR and is made of PDMS, a very efficient radiative cooling material [75]. Its impact on the thermal wavelengths in the mid-IR was demonstrated in Ref. [145]. To enhance the optical impact of the cooler on the cell efficiency, we place on top of PDMS (n~1.429) a second layer, that is a thin-film polymeric layer (~0.12 μm thickness) with a refractive index of n~1.39, acting as an antireflection layer in the optical regime [see gray line in Fig. 6.3(b)]. A common inorganic material with a similar refractive index (n~1.38) is MgF_2, however, its utilization results to a slightly lower emissivity in mid-IR, which is attributed to material's polariton gap at ~>16 μm. We note that discovering rigid polymeric thin-films of lower refractive index would result to a more efficient antireflection property. Indicatively, for PDMS or glass covers the optimal refractive index for the thin index-matched layer is n~1.225 and the optimal thickness is ~0.12 μm.

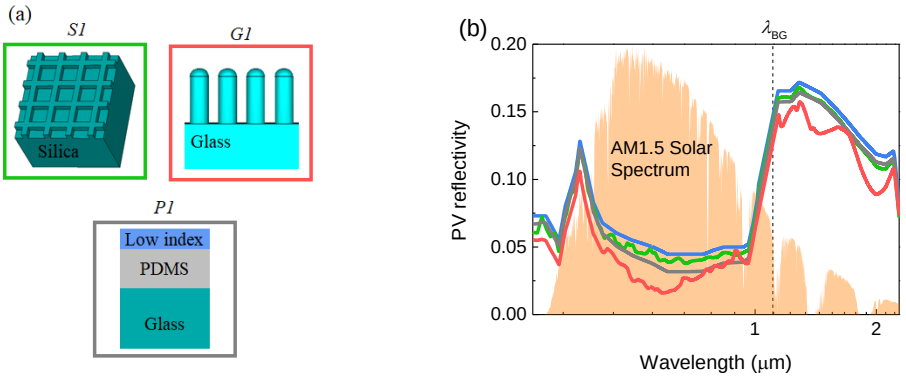

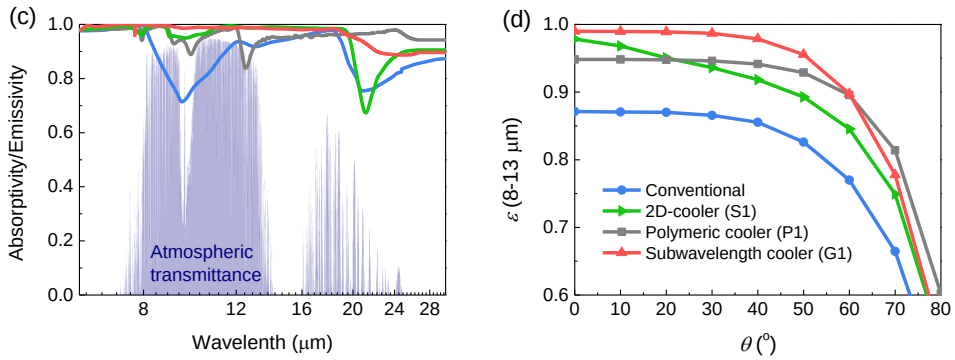

Fig. 6.3: (a) Illustrations of a 2D-PC-slab cooler (S1) consisting of silica (top left), a subwavelength cooler (G1) consisting of soda-lime glass (top right) and a two-layer polymeric cooler (P1) consisting of PDMS (n~1.43) and a thin antireflection layer on top (n~1.39) (bottom middle). (b) PV reflectivity spectra of the S1 (green line) and G1 (red line) photonic coolers in comparison with the polymeric cooler, P1, (gray line) and the conventional case (soda-lime glass - blue line) (λ_{BG} noted vertical dashed line indicates Si absorption band edge) and (c) their emissivity spectra over the thermal wavelength range in mid-IR. (d) Average emissivity between 8 and 13 μm (the atmospheric transparency window) plotted as a function of polar angle, θ (°), for the S1 (green line) and G1 (red line) photonic coolers in comparison with the polymeric cooler, P1, (gray line) and the conventional case (blue line).

The other two cases considered here (*S2*, *U2*) concern PV devices covered by UV and/or sub-bandgap reflectors, which are one-dimensional photonic crystals (PCs) [see Fig. 6.4(a)]. These 1D PCs consist of alternating thin layers of common, i.e., already utilized in solar cell applications, non-absorbing materials in the optical regime (~0.367-2.5 μm), with high index contrast; such reflectors can be placed on top of the PV without requiring further modifications in the standard encapsulated solar cell geometry. Following the pioneering works of Refs. [16,134], layer thicknesses and materials are applied with aperiodic arrangement, since aperiodicity compared to periodic structures effectively suppresses reflection oscillations at the beneficial spectral wavelengths, which is vital for solar cells. Specifically, *S2* consists of 9 alternating SiO_2 – TiO_2 thin layers and a single Al_2O_3 layer on top for anti-reflection purpose. As shown in Fig. 6.4(b) (see cyan versus blue line), this 1D PC acts as an efficient antireflection coating at ~0.36-1.107 μm, providing also significant UV and sub-bandgap reflection. This approach is particularly important, since the common antireflection coatings that only increase PV's transmissivity, and hence do not provide UV or sub-bandgap reflection, may have detrimental thermal effects [123]. Moreover, the materials selected for *S2* maintain higher emissivity compared to the conventional soda-lime glass at the atmospheric window [Fig. 6.4(d)].

The last photonic cooler discussed here [*U2* – see Fig. 6.4(a) right] was designed also taking into account that a properly designed UV reflector may also provide PV gains and temperature reduction (see Section 5.5) [84]. Effectively reflecting (i.e., up to a certain wavelength) UV radiation may be particularly important for conventional PVs with UV-absorbing encapsulants [see Fig. 4.8(b)], since the UV reflection increases considerably the lifetime of the PV, which is one of the main goals of the photonic cooling studies. UV-reflector coolers may also be particularly important for 2nd and 3rd generation solar cells consisting of sensitive materials like perovskites, polymers, etc., and for solar cells that exploit the sub-bandgap radiation, like tandem solar cells or up-conversion layer-solar cell systems. The proposed UV reflector (*U2*) [84] consists of 18 alternating Si_3N_4 – MgF_2 thin layers, of 13–105 nm thickness, respectively, and a single top layer of MgF_2 with 155 nm thickness for antireflection purpose. The materials selected maintain higher emissivity compared to the conventional soda-lime glass at the atmospheric window [Fig. 6.4(d)] and optimal UV reflection, increasing at the same time PV's transmissivity at the beneficial wavelengths [see orange versus blue line in Fig. 6.4(b)].

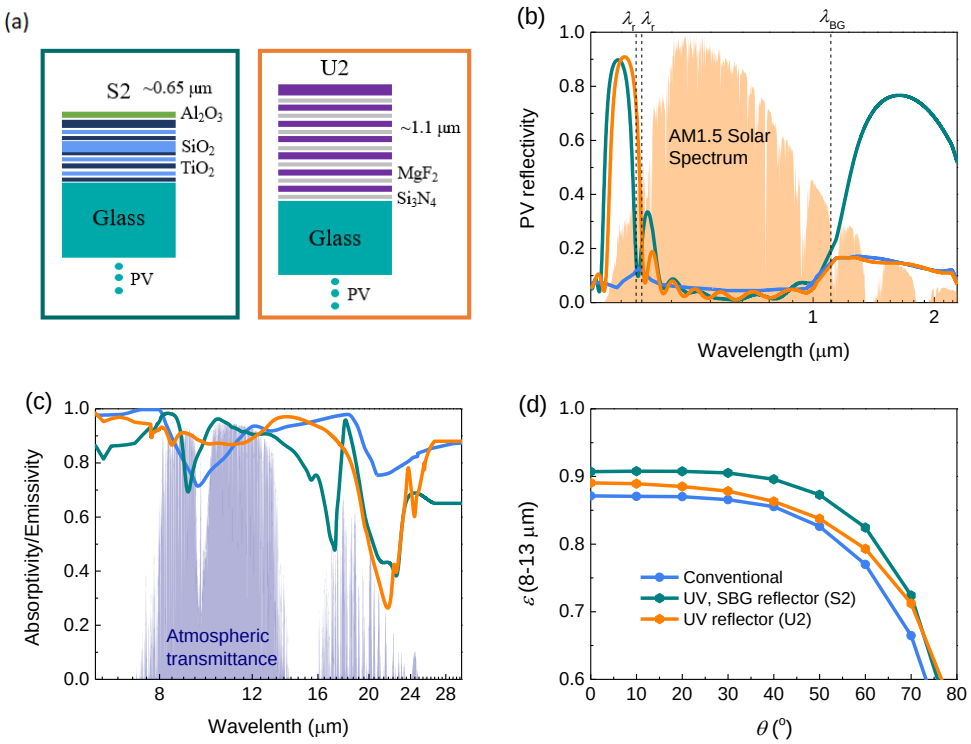

Fig. 6.4: (a) Illustrations of two 1D photonic crystals for reflection of UV and sub-bandgap radiation. S2 (left structure, in a cyan rectangle) consists of alternating SiO_2 – TiO_2 thin layers and a single layer of Al_2O_3 on top. U2 (right structure, in an orange rectangle)

consists of 19 alternating Si_3N_4 – MgF_2 thin layers. (b) PV reflectivity spectra when integrating S2 (cyan line) and U2 (orange line) on the top surface of the PV, in comparison with the conventional case (flat soda-lime glass on top PV surface - blue line) and (c) their emissivity spectra over the thermal wavelength range in mid-IR. The two black dashed vertical lines correspond to two different λ_r of 0.363/0.375 μm where we observe the maximum efficiency improvement and the limiting point, where the efficiency remains unharmed (see Section 5.5). (d) Average emissivity between 8 and 13 μm (the atmospheric transparency window) plotted as a function of polar angle, θ (°), for the S2 (cyan line) and U2 (orange line) in comparison with the conventional case (blue line).

As seen in Figs. 6.3(c), (d) and 6.4(c), (d) the 1D PCs exhibit lower emissivity than the 2D PC (*S1*), the subwavelength (*G1*) and the polymeric (*P1*) coolers at the thermal mid-IR wavelength range for all polar angles. On the other hand, the 1D PCs provide a direct heat extraction, calculated as ~94.4 W/m^2 (~49 %) (*S2*), ~18.9 W/m^2 (~65%) (*U2*) out of ~192.9 W/m^2, ~29.2 W/m^2, respectively, through the reflection of the parasitic UV and sub-bandgap solar absorption in optical [see Fig. 6.4(b)].

Further, we investigate the impact of the above discussed photonic "cooling" structures on the efficiency of the encapsulated silicon PV modules; this is done through current-voltage (*J*–*V*) calculations [see Equations (4.1), (4.2) and (4.6)]. To illustrate this impact, we present here the thermal, optical and total gains for the structures of Fig. 6.3 and 6.4, calculated from $\Delta\eta_{thermal}(\%_{rel})=\Delta\eta_{VOC}(\%_{rel})+\Delta\eta_{FF}(\%_{rel})$, $\Delta\eta_{optical}(\%_{rel})=\Delta\eta_{JSC}(\%_{rel})$, $\Delta\eta_{total}(\%_{rel})=\Delta\eta_{thermal}(\%_{rel})+\Delta\eta_{optical}(\%_{rel})$, respectively. The calculation was done by solving Equation (4.8) assuming T_{amb}=273, 300, 318 K and corresponding wind speed of ~4.3, 1.25, 0.25 m/s, to mimic mild, common and severe environmental conditions, for the PV operation, respectively. The impact of each cooler on the thermal, optical and total gain is shown in Fig. 6.5, in comparison with an ideal cooler (*I1*) for case (1) (see first paragraph of current Section).

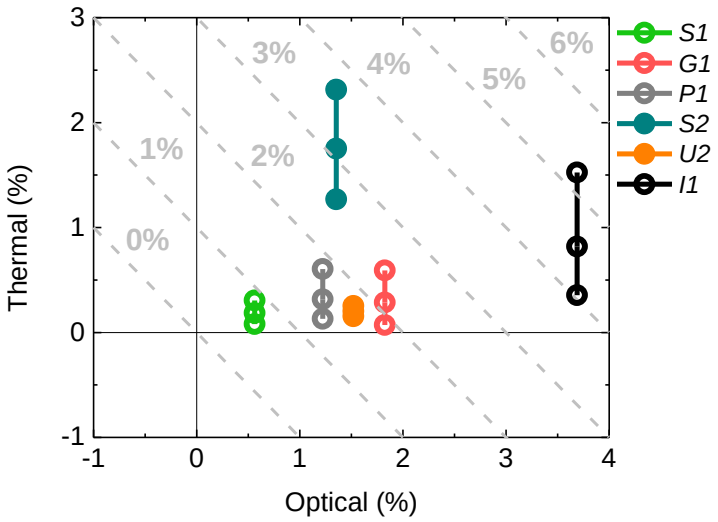

Fig. 6.5: PV gain [$\Delta\eta_{total}(\%_{rel})=\Delta\eta_{thermal}(\%_{rel})+\Delta\eta_{optical}(\%_{rel})$], relative to the conventional PV (with a flat soda-lime glass on the top surface), arising by the implementation of the photonic coolers described in Figs. 6.3, 6.4, for three different environmental conditions (denoted by the dots – see main text). The gains are decomposed into thermal [$\Delta\eta_{thermal}(\%_{rel})$] and optical components [$\Delta\eta_{optical}(\%_{rel})$], by solving Equation (4.8) [see also Equations (4.1), (4.2) and (4.6)]. The diagonal lines show contours of equal total gain. The higher thermal gain corresponds to the higher T_{amb} and lower wind speed case.

Despite the increased solar absorption provided from the photonic structures relative to the conventional flat glass (and hence the associated increased thermalization losses that result to higher heat dissipation in the structure), due to the increased top surface transmissivity in the wavelength range within the absorptive band of silicon, the operating temperature can still be reduced significantly (compared to the conventional PV), up to ~3.9 K (~-2.8 K to -3.9 K), ~0.3 K (-0.2 K to -0.3 K) for *S2*, *U2*, respectively, and ~0.5 K (0 to -0.5 K), ~0.9 K (0 to -0.9 K), 1 K (~-0.2 K to -1.0 K) for *S1*, *G1*, *P1*, respectively. Thermal together with optical gains (due to solar transmission enhancement) can reach values of up to ~+3.7 % (~+2.6 to +3.7 %), ~+1.8 % (~+1.7 to +1.8 %) for *S2*, *U2*, respectively, and ~+0.6 % to +0.9 %, ~+1.9 % to +2.4 %, ~+1.4 % to +1.8 % for *S1*, *G1*, *P1*, respectively, leading to higher absolute efficiency values by ~0.6 % (*S2*) and ~0.4 % (*G1*) with respect to the conventional PV. Interestingly, aiming primarily for an enhanced thermal-emitter-cooler compared to an optical-reflector-cooler leads to an ~0.2 % absolute efficiency decrease. We note that the ideal implementation of both reflecting UV, sub-bandgap radiation and further enhancing the beneficial absorption in optical and the emissivity in mid-IR results to gains of ~+5.6 to +10.2 %, taking also into account the different environmental conditions (+1.2

to +1.7 % in absolute values) and temperature reductions of ~4.0 to 10.6 K, implying sub-optimal cooling, heat dissipation and absorption efficiency in commercial photovoltaics.

From the results shown in Fig. 6.5, it is clear that the most efficient approach for PV efficiency enhancement is the reflection of the sub-bandgap radiation, due to the relatively high parasitic absorption from the crystalline silicon-based PV modules at that regime (see also Section 5.4). Moreover, we see no detrimental effects (no negative gains) for all cases discussed here, despite the increased PV absorptivity with the implementation of the radiative coolers, due to the improved thermal effect. Comparing *S1*, *G1*, *P1* and *I1* [i.e., ideal case (1)], shows that enhancing mid-IR radiative cooling in conjunction with increasing PVs' optical transmissivity is beneficial. In fact, many studies examining radiative cooling for solar cells note that a photonic cooler should also provide an increased transmissivity in optical, for this cooler to be economically feasible. Additionally, the cooler's hemispherical emittance must well-exceed that of conventional glasses [61]. Here, comparing the vertical "stretching" of the lines of Fig. 6.5 corresponding to *S1*, *G1*, *P1*, *I1*, we provide evidence that these requirements can be achieved by utilizing appropriate materials in conjunction with appropriate photonic designs. For instance, in Fig. 6.6, we depict the impact of material's enhanced hemispherical emittance, by assuming for *S1*, *G1*, *I1* cases conventional transmissivity in the optical regime (prefix *H*: hybrid coolers – this way PV's thermal enhancement is exclusively due to the enhanced thermal radiation) and also adding a new polymeric cooler (*HSP1*) by applying at the highly efficient PDMS radiative cooling material the same photonic patterning as *S1*.

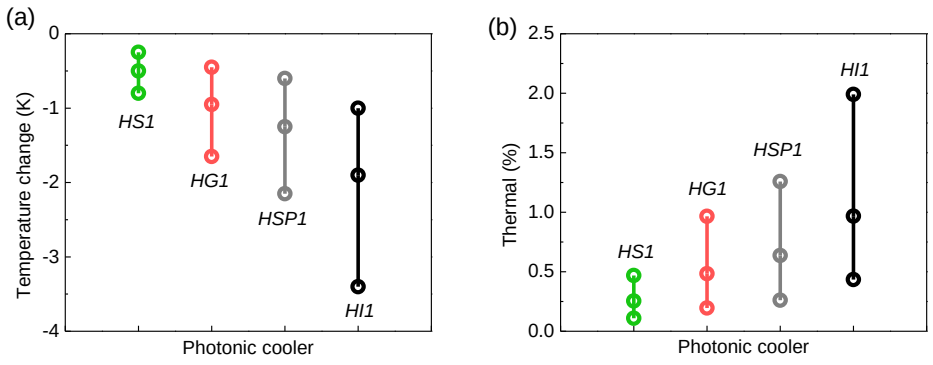

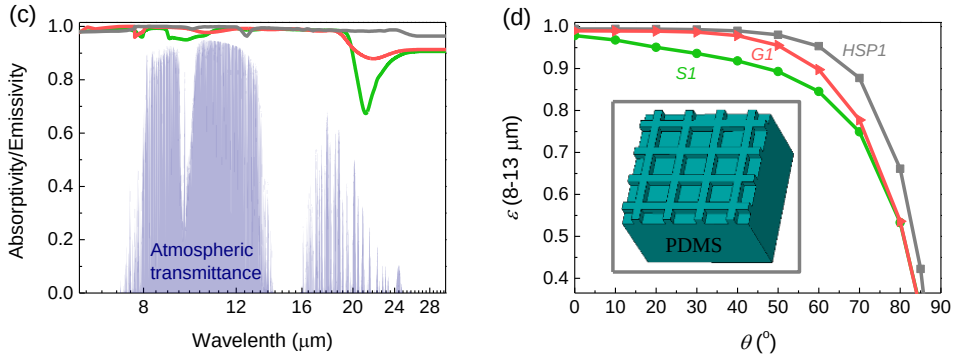

Fig. 6.6: (a) Temperature change and (b) thermal gain [$\Delta\eta_{thermal}(\%_{rel})$] arising from the photonic coolers of Figs. 6.3 and 6.4 assuming for all cases conventional transmissivity in the optical regime (prefix H: hybrid coolers). An additional polymeric cooler is added, which is a structured PDMS cooler (HSP1) with the same patterning as S1. We assume three different environmental conditions (denoted by the dots) same as in Fig. 6.5. (c) Emissivity spectra and (d) average emissivity between 8 and 13 μm plotted as a function of polar angle, θ (°), for the S1 (green line) and G1 (red line) photonic coolers in comparison with the photonic/polymeric cooler, HSP1, (assuming the same patterning as S1, see inset) (gray line).

Apparently, polymeric coolers show advantages towards this direction, i.e., providing increased hemispherical emittance [see Fig. 6.6(d)] (and potentially solar transmissivity) due to their low refractive index, in addition to the manufacturing scalability that is an important factor in PV technology [68]. Employing chemical additives or coatings [152] may also improve their outdoor performance, although, already thin polymer films with extended outdoor lifetime are available [153].

6.4 THIN NANO-MICRO-GRATING COATING FOR SOLAR CELLS

As already discussed in Section 6.1, due to the increased thermal load in solar cell devices, studies aim to further enhance materials' emissivity in the thermal wavelength range, usually by applying a photonic patterning resulting in a surface structuring in the micro-scale. Although most of the proposed structures in literature exhibit an almost perfect blackbody emissivity, their implementation in the solar cell industry depends also on their fabrication feasibility and cost-effectiveness. Manufacturing scalability is also an important factor. A way to achieve economically feasible radiative cooling is to pursue of additional improvements, e.g., to employ radiative coolers with enhanced transparency in the optical range and radiative cooling at the same

time [144]. However, most of the proposed radiative coolers are too thick (>100 μm) with a micro-structuring that is often sub-optimal for other spectral regimes besides 8-13 μm, such as 0.3–1.1 μm, where a much smaller structuring size is required.

In this section, aiming to address the aforementioned issues, we propose a scalable, few-micron-thick, and simple, single-material (glass) radiative cooler based on the superposition of properly designed in-plane nano- and micro-scaled periodic patterns on glass (see Fig. 6.7). We show that such a cooler can result to enhanced PV device performance (optical, thermal, electrical), arising from the combination of optimal surface nano- and microstructures for each spectral regime of interest (i.e., 0.3–1.1 μm and 8–13 μm). The combined efficiency gain is because the micro-grating's response in the mid-IR is not affected by the nano-grating (which controls the optical response) and vice versa.

In the first part of our studies we assume that the thin glass nano-micro-structured cooling grating, which is a two-dimensional grating (for achieving polarization insensitive response), is placed on top of a Si wafer [see Fig. 6.7(a)]. The silicon wafer is assumed *p*-type heavily-doped with a dopant of boron and resistivity of 0.0013 Ω cm [154]. (This way we take into account the substantial emissivity of crystalline silicon solar cells in the mid-IR [16,74].) For such a structure a variety of fabrication techniques are available [24,74,143,147,155]. To achieve enhanced mid-IR emissivity, our grating is imprinted in soda-lime glass, a common encapsulant material in solar cell applications, with permittivity as given in [156]. The microstructured grating has a pitch of α_m=8 μm, a height of h_m=2.2 μm, a width of w_m=2 μm, and a thickness of t=1.5 μm, as shown in Fig. 6.7(a).

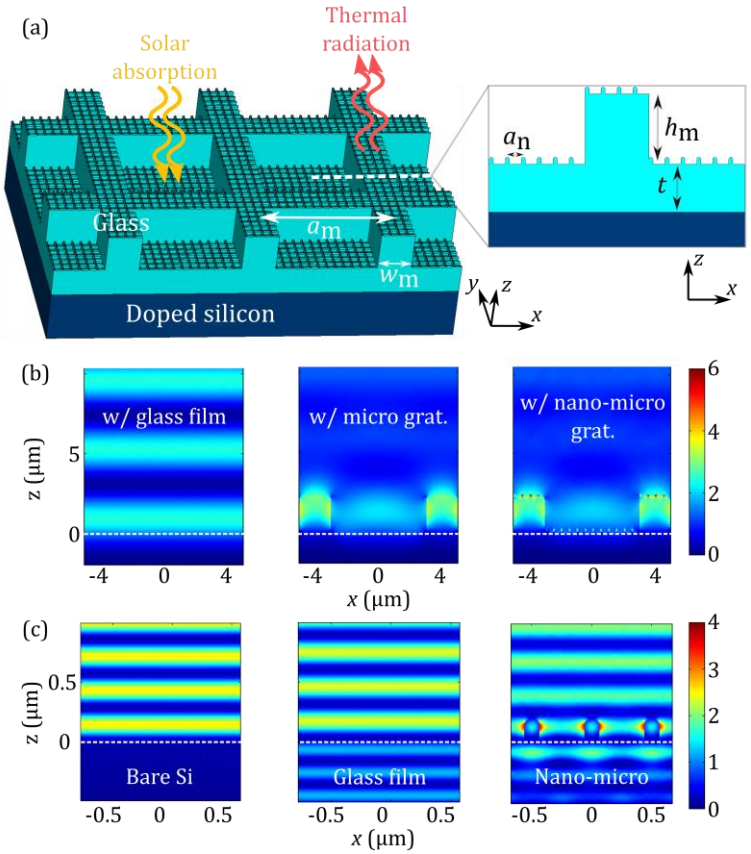

Fig. 6.7: (a) Schematic of the nano-micro-structured glass grating coating atop of a doped Si layer, and a vertical cross-section of the micro-unit-cell. (b), (c) Normalized (relative to the incident field, $\mathbf{E}_0$) distribution of the squared amplitude of the electric field at λ=8.7 μm, θ=0° in (b) for a flat 3.7-μm-thick glass film on top of Si (left), the microstructured glass grating on top of Si (middle), and the nano-micro-structured glass grating on top of Si (right) cases, and λ=0.58 μm, θ=0° in (c) for the flat Si (left), flat 1.5-μm-thick glass film on top of Si (middle), and the nano-micro-structured glass grating on top of Si (right) cases.

The resulting emissivity at the atmospheric transparency window (8–13 μm) is shown in Figs. 6.8(a) and 6.8(b), where a significant enhancement compared to bare Si and a flat glass film is demonstrated, which is maintained even for larger incidence angles (e.g. larger than 60°). This enhancement is related both to the excitation of localized resonant modes in the pillars of the grating as well as to the lattice effect that excites collective in-plane surface states [see Fig. 6.7(b)] for both *s*- and *p*-polarization. Such states arise from arrays satisfying the Bragg scattering condition, i.e., the array period α and the free space wavelength λ_0 obey the Equation (2.11), $\alpha\left(\sqrt{\varepsilon} \pm sin\theta\right) = l\lambda_0$, where ε is the dielectric constant of the optical medium, l is an integer, and θ is the angle of incidence.

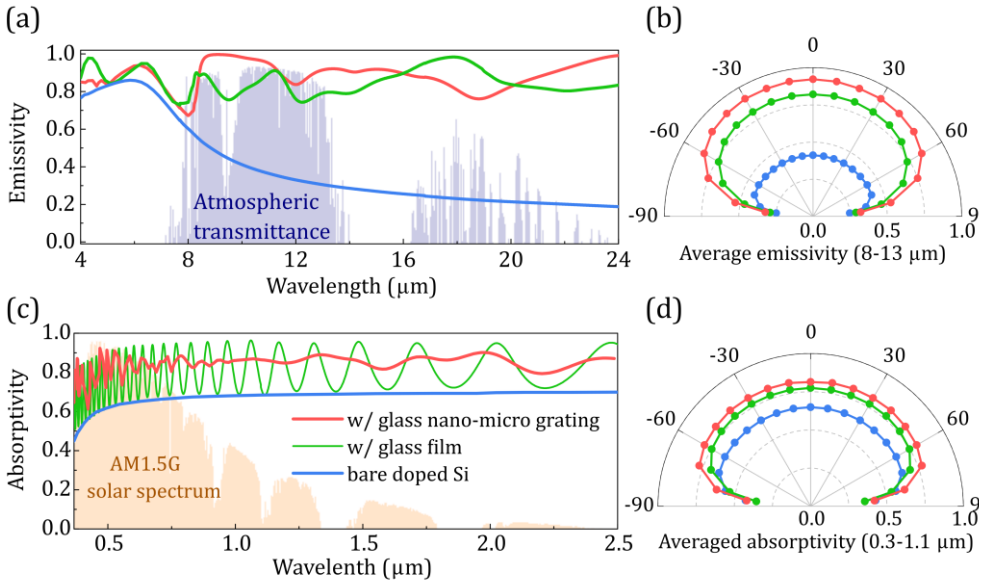

Fig. 6.8: Absorptivity/emissivity spectra of the radiative cooler shown in Fig. 6.7(a), in (a) thermal and (c) solar wavelengths, compared to a bare doped silicon and a Si covered by a 3.7-μm-thick glass film. (b) Angular dependence of the average emissivity at 8-13 μm (averaged over wavelength) for the systems of (a). (d) Absorbed fraction of solar radiation at 0.3-1.1 μm weighted by the AM1.5G spectrum [55].

On top of the microstructured grating, and in order to achieve an enhanced transparency in the optical wavelengths compared to a flat-glass film, we superimpose a two-dimensional nanostructured grating with a pitch of α_n=0.5 μm, a height of h_n=0.21 μm, and a width of w_n=0.13 μm. (Such structures may be quite easily realized by laser induced nanostructuring [147,155,157,158]; therefore their potential for light harvesting in solar cells is worthy to be examined.) The resulting broadband transparency (anti-reflectivity), compared to bare Si [see Figs. 6.8(c), 6.8(d)], arises from two main effects. Firstly, the presence of the glass film (even flat glass) reduces the reflection at the air/Si interface. This is verified in Fig. 6.7(c). This reduction comes from interferences within the thin film implied by the oscillations of the corresponding absorption curve [see Fig. 6.8(c), green lines] [74]. Secondly, the resonant response of the nanostructured grating and the associated strong scattering result also to reduced reflection at the air/glass interface and thus to further absorption enhancement in Si [see Fig. 6.7(c) and Fig. 6.8(c–d)] [147,151,159] (note that glass practically does not absorb at those wavelengths).

The optimized nano- and microstructured gratings indicate that each case's optimum size differs by over an order of magnitude. Moreover, comparing the ***E***-field intensity in Fig. 6.7(b) middle and right indicates that

the impact of the micro-grating in mid-IR is not affected by the nano-grating. Both results validate the idea of superimposing nano-micro-structured gratings for enhancing device performance. Overall, the nano-micro-structured grating exhibits a high mid-IR emissivity of >0.85 [at 0−60° − see Fig. 6.8(b)] as well as >0.79 (0−60°) Si optical absorptivity [see Fig. 6.8(d)], yielding a ~25.4 % solar absorption enhancement (at 0.3-1.1 μm), compared to a bare Si wafer. The Si absorption enhancement in the optical wavelengths provided by the proposed nano-micro-structured grating is considerably higher than that of the scalable thin radiative coolers proposed in the literature, with values of ~19.0 % (compared, e.g., to the coolers proposed in Refs. [74,143]).

The enhanced emissivity provided by the nano-micro-grating at the atmospheric window implies improved device thermal response. The change in the bare Si wafer's steady-state temperature (ΔT) when we incorporate the glass nano-micro-grating radiative cooler is calculated [by solving Equation (3.1) for $P_{net}(T)=0$] and plotted in Fig. 6.9(a). The nonradiative heat-transfer coefficient, h_c, was taken in the range of 5.5–12 W/m^2/K, corresponding to wind speeds of 1–3 m/s [74,143], and the ambient temperature in the range of 0–44 ºC.

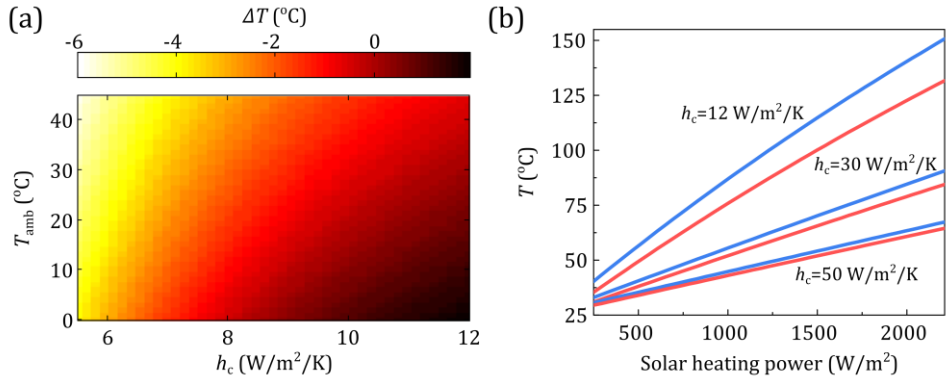

Fig. 6.9: (a) Calculated steady-state temperature change, ΔT(ºC), with the implementation of the nano-micro-structured grating on top of a bare doped silicon wafer, as a function of the conduction-convection coefficient, h_c, and the ambient temperature, T_{amb}. (b) Calculated steady-state temperature of Si with nano-micro-structured grating (red), and bare silicon (blue)] versus the solar heating power, for h_c = 12 W/m^2/K (corresponding to natural convection) and 30, 50 W/m^2/K (corresponding to forced convection or actively cooled systems).

The temperature decrease provided by the nano-micro-grating coating (of equivalent/average thickness 2.46 μm) compared to the bare doped silicon is approximately up to 5.8 ºC, and up to 0.2 ºC compared to the flat 3.7-μm-thick glass film case, despite the augmented solar absorption by 164.8 W/m^2 and

36.1 W/m^2, respectively. Indicatively, for silicon-based solar cells, a temperature decrease by 1 °C could increase the efficiency by ~0.45 %$_{rel}$, while the aging rate doubles if the temperature increases by 10 °C [10]. As shown in Fig. 6.9(a), the positive impact of the nano-micro-grating coating on device temperature increases as outdoor temperature increases; it further increases (in a nonlinear manner) as h_c decreases, indicating the greater importance of radiative cooling in severe environmental conditions (e.g., high temperatures with low wind speeds), in particular when convective cooling is not adequate.

Another evaluation of the nano-micro-grating cooler is given in Fig. 6.9(b), where we plot the device temperature in the case of the nano-micro-grating atop of doped silicon (red) compared to bare Si (blue), as a function of the solar heating power of the device ranging from 250 to 2200 W/m^2 [to roughly estimate the cooler impact also in concentrated PV systems (CPVs), where the absorbed solar power reaches values higher than 1000 W/m^2]. Indicatively, depending on the conditions (clouds, humidity), the expected heat output of a crystalline solar cell under peak unconcentrated solar irradiance (1000 W/m^2) can reach values higher than 250 W/m^2 up to approximately 730 W/m^2. We observe that the temperature reduction, coming from the implementation of the radiative cooler, scales up almost linearly with the solar heating power. Even in the case of low-concentration systems and high h_c, i.e., 30 and 50 W/m^2/K, which correspond to actively cooled systems, the temperature reduction can reach values of ~6.2 ^{o}C and ~2.9 ^{o}C, respectively. Results in Fig. 6.9(b) demonstrate also the increased impact of passive radiative cooling in CPVs, due to their higher absorbed solar powers and high device temperatures that develop (>80 ^{o}C) [16]. (Temperature reductions due to radiative cooling have been reported already in CPVs by using a conducting surface area larger than the cell itself [146].) Despite their high operating temperatures, CPVs constitute promising candidates for efficient and cost-effective energy harvesting due to their high efficiencies, induced by incorporating low-cost concentrator lenses, and the associated lower electrical-power-temperature coefficients compared to conventional PVs. Our results demonstrate that radiative cooling can play a significant role in the case of CPVs, given that it can be employed efficiently in conjunction with other nonradiative cooling techniques, such as backside finned heat exchangers with/or forced air convection.

In the second part of our studies regarding the nano-micro grating cooler, we examine its impact on both the temperature and the efficiency of a realistic encapsulated IBC-PV system [see Fig. 6.10(b)] by solving Equation (4.8). Comparing the optical absorptivity and the mid-IR emissivity of the

encapsulated IBC cell without and with the nano-micro-grating cooler [see Figs. 6.10(a), (c), (d)], one can see already the high impact of the grating on the absorption and emission properties of the PV. This impact, as shown below, is translated to lower PV operating temperatures and enhanced efficiencies.

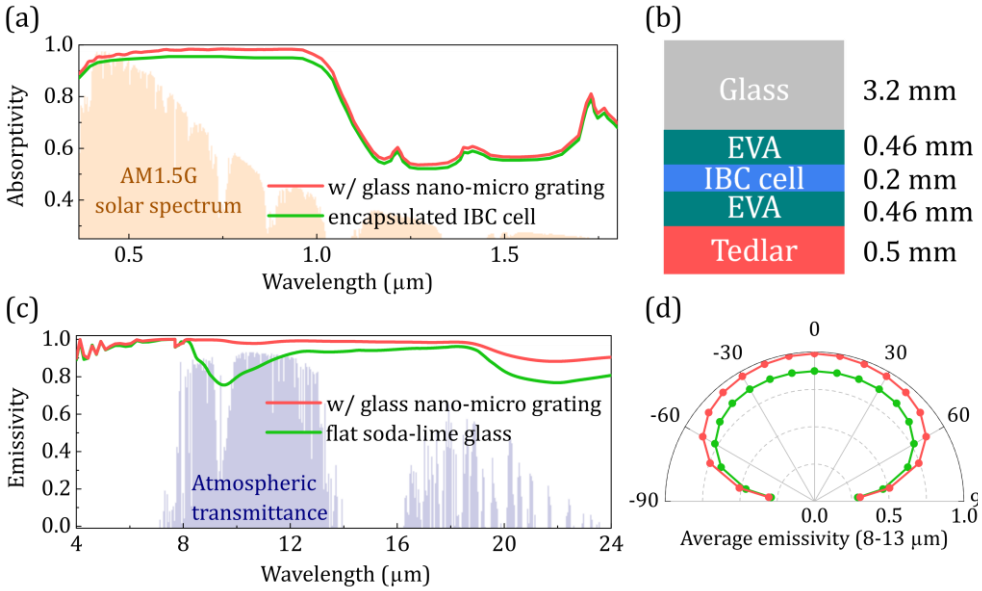

Fig. 6.10: (a) Absorptivity spectra of the encapsulated IBC cell (green, see main text) and of the encapsulated cell with the glass nano-micro-grating on top of it (red). (b) Conventional material stacking of the encapsulated crystalline silicon-based IBC solar cell. (c) Emissivity spectra of a 3.2-mm-thick PV glass (green) and of the proposed nano-micro grating cooler assuming a semi-infinite glass substrate (red), and (d) angular dependence of the average emissivity at 8-13 μm.

In Fig. 6.11 we depict the impact of the glass nano-grating, the glass micro-grating, and the glass nano-micro-grating when applied on the encapsulated IBC cell [Fig. 6.10(b)], on the operating temperature and efficiency change (comparing to the conventional cell - with the flat-glass). Additionally, we compare with two common glass antireflection coatings (glass ARCs), which are a 99 nm porous SiO_2 layer (ARC_1) and a thin low-index MgF_2 layer (ARC_2), with data extracted from Ref. [160]. The PV is assumed to operate under the following environment conditions (from Ref. [145]): illumination under the AM1.5G spectrum (1000 W/m^2), T_{amb}=30 ^{o}C, $h_{c,top}$=10 W/m^2/K (~1.2 m/s wind speed), $h_{c,bottom}$=5 W/m^2/K (~0.8 m/s wind speed).

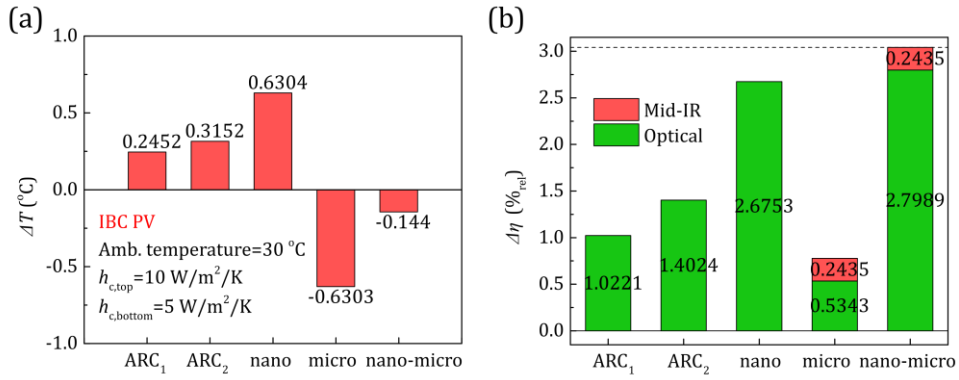

Fig. 6.11: The change in the operating temperature (a) and efficiency (b) of the IBC PV of Fig. 6.10(b) resulting from the implementation of the only nano-, only micro- and nano-micro gratings of Fig. 1(a), compared also to that of two conventional antireflection coatings (glass-ARCs). The parameters shown in the legends are explained in the main text.

As seen in Fig. 6.11(a), the operating temperature increases with the implementation of ARC_1, ARC_2, and glass nano-grating. This temperature increase is due to the enhanced optical absorption associated with the increased heat dissipation within the Si absorption band range (0.28–1.107 μm), often called thermalization losses, as well as the increased unwanted absorption at the sub-bandgap range (1.107–4 μm). On the other hand, the glass micro-grating results in a temperature reduction of ~0.6 °C due to the improved thermal response in the thermal wavelength range in the mid-IR. Interestingly, the implementation of the combined nano-micro-grating still results in an operating temperature reduction (~0.1 °C) rather than an increase, despite the increased optical absorption [at 0.28–4 μm – red line in Fig. 6.11(a)]. (Note that if one assumes zero optical absorption enhancement, the temperature reduction would be slightly higher.)

In Fig. 6.11(b), we plot the relative efficiency increase (gain), $\Delta\eta(\%_{rel})$, with the implementation of each radiative cooler. Namely, we calculate the optical gain, $\Delta\eta_{optical}(\%_{rel})$, assuming conventional (flat glass) PV emissivity in the thermal wavelengths in the mid-IR. Accordingly, we calculate the gain due to the emissivity enhancement in the mid-IR, $\Delta\eta_{mid\text{-}IR}(\%_{rel})$, by assuming flat glass absorptivity in the optical. For the total gain, $\Delta\eta_{total}(\%_{rel})$, we take into account both the optical and the mid-IR responses from each cooler. As seen in Fig. 6.11(b), substantial optical gains arise for the cases of the glass nano- and nano-micro-structured gratings, considerably higher than those of conventional glass ARCs. Indicatively, the glass nano- and the glass nano-micro-structured grating achieve optical gains of ~2.8 % compared to ~1.0 % and ~1.4 % of ARC_1 and ARC_2, respectively. Moreover, the glass nano-micro-grating provides additional gain due to the enhanced emissivity in the mid-IR

[see Fig. 6.10(c),(d)], resulting to total gain of ~3.1 %. Examining different environmental conditions (different h_c and T_{amb}), we found that the efficiency increase, $\Delta\eta(\%_{rel})$, compared to the conventional case, is always higher than 2.96 %.

In conclusion, in this last section of Chapter 6, we have demonstrated that the superposition of properly designed in-plane nano- and micro-scaled periodic patterns in a thin, glass radiative cooler on top of a Si-based solar cell can significantly enhance solar cells' performance. The microscale patterning enhances cooler's performance in the atmospheric transparency window (8–13 μm) while the nanopatterning further enhances the optical radiation absorption (i.e., in the Si absorption band: 0.3–1.1 μm). The combined enhancement is possible because the emissivity enhancement provided by the micro-grating in the thermal wavelengths is not affected by the nano-grating and vice versa. We evaluated the impact of the proposed nano-micro-structured grating on the temperature and absorption efficiency of a commercial PV and we found a relative efficiency increase higher than 3.0 %, performance surpassing any previously reported results in the literature. Thus, our findings in the present section can significantly impact the PV industry, as well as other radiative cooling applications. Moreover, the proposed combined double- or multi-periodic patterning approach is a simple, single-material and scalable approach, suitable for all devices affected by photon management at different wavelength ranges/scales.

7
CONCLUSIONS

7.1 CONCLUSIONS AND OUTLOOK

In this work we examined and discussed the physical mechanisms and requirements for cooling radiatively selected state-of-the-art silicon-based photovoltaics (PVs). Besides radiative cooling, common photonic strategies for reducing radiatively heat generation within the PV cell, such as ultraviolet and sub-bandgap reflection, were also examined and their detailed impact on the PV temperature and efficiency was evaluated. This was done by deriving and employing an opto-electro-thermal modeling which takes into account all the major intrinsic processes affected by the temperature variation in a PV device. The accuracy and applicability of our model was tested through comparison with experimental data provided by PV manufacturers concerning highly-efficient cells with interdigitated state-of-art type back contacts (IBC).

Employing our model, we showed that the main reason of the efficiency decrease due to the heating in crystalline silicon-based PVs is the increased electron-hole nonradiative recombination at elevated temperatures, which in turn reduces the quantum efficiency, *QE*, defined as $QE=J_{rad}/(J_{rad}+J_{nrad})$ with $J_{rad/nrad}$ the radiative/non-radiative recombination current density, resulting to decreased open-circuit-, and maximum-point-voltage. To reduce this effect realistic photonic coolers were designed and their impact on the operating temperature and PV efficiency was evaluated and compared with "ideal" structures, i.e., perfect thermal emitters and UV/sub-bandgap reflectors. The main conclusions of this task are that one-dimensional (1D) photonic crystals (PCs) acting as UV/sub-bandgap-reflecting coolers may improve the thermal effect in PVs considerably, increasing this way the PV yield and lifetime. Considering the impact of harmful UV radiation on the lifetime of PVs, we showed that implementing a photonic approach to effectively (i.e., up to a certain wavelength) reflect it, may provide an effective alternative to the existing costly techniques for screening UV, without sacrificing PV

performance or even increasing it. Interestingly, the proper design of the reflectors-coolers, even without requiring a high number of layers in the case of 1D PCs (i.e., ~10), provides further efficiency gains, arising by the increased photocurrent due to the improved transmissivity at the beneficial wavelengths in the optical regime.

Regarding the impact of radiative cooling in mid-IR we found that enhancing radiative cooling is an efficient approach for enhancing PVs performance if combined with cost-friendly materials and sophisticated photonic designs that simultaneously enhance the hemispherical emittance and the transparency in optical range. Polymeric coolers show advantages towards this direction due to their low refractive index, in addition to the manufacturing scalability. Their reliability though related to dust or moisture should be examined. Moreover, we demonstrated that 2D PC slabs seem to be promising candidates for the realization of cost-effective radiative cooling in solar cells. Important advantages of these photonic designs are their simplicity compared for example to the more complex 2D or 3D photonic crystals as well as the high hemispherical emittance that arises from the photonic patterning of the materials. Additionally, because of the lattice effect, the 2D PC slabs are both shape- and material-independent further facilitating this way the fabrication process considerably. Our study also demonstrated that the utilization of double-periodic, thin radiative cooling coatings can significantly enhance solar cells' performance. The combination of properly designed in-plane nano- and micro-scale periodic patterns on top of thin glass films or on top of realistic photovoltaics can result to an optimum transparency in the optical and an optimum emissivity in the mid-IR, simultaneously. Specifically, the microscale patterning enhances cooler's performance in the atmospheric transparency window (8–13 μm) while the nanopatterning further enhances the optical radiation absorption (i.e., in the Si absorption band: 0.3–1.1 μm). These findings pave the way for cost-effective radiative cooling in solar cells and therefore can significantly impact the PV industry, as well as other radiative cooling applications.

Utilizing photonic approaches for the thermal management in PVs constitutes a quite robust strategy to increase the PV efficiency, in respect to the varying operating conditions and the various characteristics of crystalline silicon-based PVs. Gains were always present especially when convective cooling is not adequate. Moreover, for all cases (all realistic photonic coolers examined), we report no detrimental thermal effects despite the increased optical absorption associated with increased thermalization losses.

The main advantage of radiative cooling and heat reduction techniques compared to conventional cooling approaches is the passive operation.

Temperature reduction can reach values of ~2.8 to 3.9 K (~-4.0 to -10.6 K ideally) with no extra energy input and without increasing the complexity of the PV design significantly. Nowadays, a hybrid photovoltaic/thermal (PV/T) solar system is one of the most common methods for cooling the photovoltaic panels [12,161]. It consists of photovoltaic panels combined with a cooling system and it actually combines the solar cell technology, i.e., solar to electrical energy conversion, and solar thermal technology, i.e., solar to thermal energy conversion. The cooling agent, water or air for example, is circulated around the PV panels for cooling the solar cell, and the warm water or air leaving the panels may be used for domestic applications such as domestic heating. The integrated cooling systems such as backside finned heat exchangers with/or forced air convection (active cooling) or active water cooling have shown to decrease the solar cell temperature by even more than ~10 degrees [161]. It is also shown in the literature that using water as a coolant is more effective than using air. Hence, the goal is to minimize the amount of water and energy needed for cooling the solar panels. This practically means that there is a compromise between the output energy from the PV panels and the energy needed for cooling [12]. It could be possible to integrate radiative cooling in PV/T systems for harnessing electrical and thermal energy simultaneously. For instance, the fluid used for cooling returns to a water tank that is often buried into the ground to avoid solar heating. Incorporating fluid cooling panels that harness radiative sky cooling may result in a significant reduction of the energy consumed in the case of PV/T systems [162].

Finally, it is important to note that the radiative cooling effect may potentially play a significant role in thermal management of concentrating PV systems (CPVs) (more than 1 sun), since its impact linearly scales up with the solar heating power. In CPVs, higher temperature reductions than in conventional PVs due to radiative cooling, have already been reported, by using a conducting surface area larger than the cell itself [146,163]. Therefore, radiative cooling may be employed efficiently in conjunction with other nonradiative cooling techniques for the case of CPVs [16]. Moreover, other optoelectronic devices such as thermoradiative cells, thermoelectric generators (TEGs), thermophotovoltaics or automobiles can also benefit from radiative cooling due to the asymmetric radiative heat exchange of the device with the environment.

The modeling technique proposed in the present study can be extended and describe any other state-of-the-art solar cell system, i.e., multi-, mono-crystalline silicon solar cells, as well as the emerging thin-film PV technologies like the organic or the organic-inorganic-perovskite solar cells

consisting of sensitive materials. This can be done by arbitrarily modifying cell's quantum efficiency (ratio of the radiative recombination rate to radiative and non-radiative) appropriately, independently of the nature of the recombination process. Properly applying the radiative cooling strategy could pave the way towards commercialization of different novel solar cell technologies and materials.

8

REFERENCES

1. "Homepage - U.S. Energy Information Administration (EIA)," https://www.eia.gov/.
2. "IEA – International Energy Agency," https://www.iea.org/.
3. "• Statista - The Statistics Portal for Market Data, Market Research and Market Studies," https://www.statista.com/.
4. J. Wang, L. Feng, X. Tang, Y. Bentley, and M. Höök, "The implications of fossil fuel supply constraints on climate change projections: A supply-side analysis," Futures **86**, 58–72 (2017).
5. "Annual reports – IEA-PVPS," https://iea-pvps.org/annual-reports/.
6. "Global Overview," https://www.ren21.net/gsr-2019/chapters/chapter_01/chapter_01/.
7. J. Jean, M. Woodhouse, and V. Bulović, "Accelerating Photovoltaic Market Entry with Module Replacement," Joule **3**(11), 2824–2841 (2019).
8. T. Deppe and J. N. Munday, "Nighttime Photovoltaic Cells: Electrical Power Generation by Optically Coupling with Deep Space," ACS Photonics **7**(1), 1–9 (2020).
9. D. Otth, R. R.-29th I. of E. S. Technical, and undefined 1983, "Assessing photovoltaic module degradation and lifetime from long term environmental tests," jpl.nasa.gov (n.d.).
10. E. Skoplaki and J. A. Palyvos, "On the temperature dependence of photovoltaic module electrical performance: A review of efficiency/power correlations," Sol. Energy **83**(5), 614–624 (2009).
11. H. G. Teo, P. S. Lee, and M. N. A. Hawlader, "An active cooling system for photovoltaic modules," Appl. Energy **90**(1), 309–315 (2012).

12. K. A. Moharram, M. S. Abd-Elhady, H. A. Kandil, and H. El-Sherif, "Enhancing the performance of photovoltaic panels by water cooling," Ain Shams Eng. J. **4**(4), 869–877 (2013).

13. A. Akbarzadeh and T. Wadowski, "Heat pipe-based cooling systems for photovoltaic cells under concentrated solar radiation," Appl. Therm. Eng. **16**(1), 81–87 (1996).

14. J. D. Jackson, *Classical Electrodynamics* (Wiley, 1999).

15. L. Zhu, A. P. Raman, and S. Fan, "Radiative cooling of solar absorbers using a visibly transparent photonic crystal thermal blackbody.," Proc. Natl. Acad. Sci. U. S. A. **112**(40), 12282–7 (2015).

16. W. Li, Y. Shi, K. Chen, L. Zhu, and S. Fan, "A Comprehensive Photonic Approach for Solar Cell Cooling," ACS Photonics **4**(4), 774–782 (2017).

17. "J. D. Joannopoulos, S. G. Johnson, J. N. Winn, and R. D. Meade, Photonic Crystals: Molding the Flow of Light, second ed. (Princeton Univ. Press, Princeton, New Jersey, 2008)," https://press.princeton.edu/books/hardcover/9780691124568/photonic-crystals.

18. J. N. Winn, Y. Fink, S. Fan, and J. D. Joannopoulos, "Omnidirectional reflection from a one-dimensional photonic crystal," Opt. Lett. **23**(20), 1573 (1998).

19. R. Srivastava, K. B. Thapa, S. Pati, and S. P. Ojha, "Omni-direction reflection in one dimensional photonic crystal," Prog. Electromagn. Res. B **7**, 133–143 (2008).

20. *S. A. Maier. Plasmonics: Fundamentals and Applications. Springer, New York, USA, 2007.* (n.d.).

21. A. V. Krasavin and N. I. Zheludev, "Active plasmonics: Controlling signals in Au/Ga waveguide using nanoscale structural transformations," Appl. Phys. Lett. **84**(8), 1416–1418 (2004).

22. I. Dolev, I. Epstein, and A. Arie, "Surface-plasmon holographic beam shaping," Phys. Rev. Lett. **109**(20), 203903 (2012).

23. I. Epstein, I. Dolev, D. Bar-Lev, and A. Arie, "Plasmon-enhanced Bragg diffraction," Phys. Rev. B - Condens. Matter Mater. Phys. **86**(20), 205122 (2012).

24. G. Perrakis, O. Tsilipakos, G. Kenanakis, M. Kafesaki, C. M. Soukoulis, and E. N. Economou, "Perfect optical absorption with nanostructured metal films: design and experimental demonstration,"

Opt. Express **27**(5), 6842 (2019).

25. N. I. Landy, S. Sajuyigbe, J. J. Mock, D. R. Smith, and W. J. Padilla, "Perfect metamaterial absorber," Phys. Rev. Lett. **100**(20), 207402 (2008).

26. K. Aydin, V. E. Ferry, R. M. Briggs, and H. A. Atwater, "Broadband polarization-independent resonant light absorption using ultrathin plasmonic super absorbers," Nat. Commun. **2**(1), 1–7 (2011).

27. C. L. C. Smith, N. Stenger, A. Kristensen, N. A. Mortensen, and S. I. Bozhevolnyi, "Gap and channeled plasmons in tapered grooves: A review," Nanoscale **7**(21), 9355–9386 (2015).

28. L. Liu, Z. Han, and S. He, "Novel surface plasmon waveguide for high integration," Opt. Express **13**(17), 6645 (2005).

29. E. Moreno, F. J. Garcia-Vidal, S. G. Rodrigo, L. Martin-Moreno, and S. I. Bozhevolnyi, "Channel plasmon-polaritons: modal shape, dispersion, and losses," Opt. Lett. **31**(23), 3447 (2006).

30. C. Cherqui, M. R. Bourgeois, D. Wang, and G. C. Schatz, "Plasmonic Surface Lattice Resonances: Theory and Computation," Acc. Chem. Res. **52**(9), 2548–2558 (2019).

31. L. Rayleigh, "Note on the remarkable case of diffraction spectra described by Prof. Wood. Phil. Mag.," **14**, 60–65 (1907).

32. A. Hessel and A. A. Oliner, "A New Theory of Wood's Anomalies on Optical Gratings," Appl. Opt. **4**(10), 1275 (1965).

33. I. R. Hooper and J. R. Sambles, "Some considerations on the transmissivity of thin metal films," Opt. Express **16**(22), 17258 (2008).

34. E. D. Palik, *Handbook of Optical Constants of Solids. II* (Academic Press, 1998).

35. A. D. Rakić, A. B. Djurišić, J. M. Elazar, and M. L. Majewski, "Optical properties of metallic films for vertical-cavity optoelectronic devices," Appl. Opt. **37**(22), 5271 (1998).

36. Z. Han and S. I. Bozhevolnyi, "Radiation guiding with surface plasmon polaritons," Reports Prog. Phys. **76**(1), 016402 (2013).

37. A. V. Zayats, I. I. Smolyaninov, and A. A. Maradudin, "Nano-optics of surface plasmon polaritons," Phys. Rep. **408**(3–4), 131–314 (2005).

38. A. Abass, S. R. K. Rodriguez, J. Gómez Rivas, and B. Maes,

"Tailoring Dispersion and Eigenfield Profiles of Plasmonic Surface Lattice Resonances," ACS Photonics **1**(1), 61–68 (2014).

39. S. Enoch and N. Bonod, *Plasmonics - From Basics to Advanced Topics* (2012), **167**.

40. H. Tan, R. Santbergen, A. H. M. Smets, and M. Zeman, "Plasmonic Light Trapping in Thin-film Silicon Solar Cells with Improved Self-Assembled Silver Nanoparticles," Nano Lett. **12**(8), 4070–4076 (2012).

41. G. Kakavelakis, I. Vangelidis, A. Heuer-Jungemann, A. G. Kanaras, E. Lidorikis, E. Stratakis, and E. Kymakis, "Plasmonic Backscattering Effect in High-Efficient Organic Photovoltaic Devices," Adv. Energy Mater. **6**(2), 1501640 (2016).

42. G. Perrakis, G. Kakavelakis, G. Kenanakis, C. Petridis, E. Stratakis, M. Kafesaki, and E. Kymakis, "Efficient and environmental-friendly perovskite solar cells via embedding plasmonic nanoparticles: an optical simulation study on realistic device architectures," Opt. Express **27**(22), 31144–31163 (2019).

43. C. F. Bohren and D. R. Huffman, *Absorption and Scattering of Light by Small Particles* (Wiley, 1998).

44. T. Wriedt, "Mie theory: A review," Springer Ser. Opt. Sci. **169**, 53–71 (2012).

45. "Lecture 29: The Earth's Atmosphere," http://www.astronomy.ohio-state.edu/~pogge/Ast161/Unit5/atmos.html.

46. M. Planck, *The Theory of Heat Radiation* (Tomash, 1988).

47. "IR Transmission Spectra | Gemini Observatory," http://www.gemini.edu/sciops/telescopes-and-sites/observing-condition-constraints/ir-transmission-spectra.

48. S. Catalanotti, V. Cuomo, G. Piro, D. Ruggi, V. Silvestrini, and G. Troise, "The radiative cooling of selective surfaces," Sol. Energy **17**(2), 83–89 (1975).

49. D. Michell and K. L. Biggs, "Radiation cooling of buildings at night," Appl. Energy **5**(4), 263–275 (1979).

50. E. Rephaeli, A. Raman, and S. Fan, "Ultrabroadband Photonic Structures To Achieve High-Performance Daytime Radiative Cooling," Nano Lett. **13**(4), 1457–1461 (2013).

51. A. P. Raman, M. A. Anoma, L. Zhu, E. Rephaeli, and S. Fan, "Passive

radiative cooling below ambient air temperature under direct sunlight," Nature **515**(7528), 540–544 (2014).

52. R. Kumar and S. C. Kaushik, "Performance evaluation of green roof and shading for thermal protection of buildings," Build. Environ. **40**(11), 1505–1511 (2005).

53. "Total Energy Monthly Data - U.S. Energy Information Administration (EIA)," https://www.eia.gov/totalenergy/data/monthly/.

54. J. Testa and M. Krarti, "A review of benefits and limitations of static and switchable cool roof systems," Renew. Sustain. Energy Rev. **77**, 451–460 (2017).

55. "Solar Spectral Irradiance: Air Mass 1.5," https://rredc.nrel.gov/solar/spectra/am1.5/.

56. P.-M. Robitaille, *Kirchhoff's Law of Thermal Emission: 150 Years* (2009), **4**.

57. W. Shockley and H. J. Queisser, "Detailed Balance Limit of Efficiency of *p-n* Junction Solar Cells," J. Appl. Phys. **32**(3), 510–519 (1961).

58. R. Couderc, M. Amara, and M. Lemiti, "In-Depth Analysis of Heat Generation in Silicon Solar Cells," IEEE J. Photovoltaics **6**(5), 1123–1131 (2016).

59. O. Dupré, R. Vaillon, and M. A. Green, "A full thermal model for photovoltaic devices," Sol. Energy **140**, 73–82 (2016).

60. R. M. Almeida, "Detection of LO modes in glass by infrared reflection spectroscopy at oblique incidence," Phys. Rev. B **45**(1), 161–170 (1992).

61. A. R. Gentle and G. B. Smith, "Is enhanced radiative cooling of solar cell modules worth pursuing?," Sol. Energy Mater. Sol. Cells **150**, 39–42 (2016).

62. A. S. Barker and R. Loudon, "Response functions in the theory of raman scattering by vibrational and polariton modes in dielectric crystals," Rev. Mod. Phys. **44**(1), 18–47 (1972).

63. M. K. Gunde, "Vibrational modes in amorphous silicon dioxide," Phys. B Condens. Matter **292**(3–4), 286–295 (2000).

64. T. B. Wang, Z. G. Liu, and C. Z. Tan, "Relationship between the frequency of the main LO mode of silica glass and angle of

incidence," J. Chem. Phys. **119**(1), 505–508 (2003).

65. J. D. Caldwell, L. Lindsay, V. Giannini, I. Vurgaftman, T. L. Reinecke, S. A. Maier, and O. J. Glembocki, "Low-loss, infrared and terahertz nanophotonics using surface phonon polaritons," Nanophotonics **4**(1), 44–68 (2015).

66. J. Ordonez-Miranda, L. Tranchant, Y. Chalopin, T. Antoni, and S. Volz, "Thermal conductivity of nano-layered systems due to surface phonon-polaritons," J. Appl. Phys. **115**(5), 054311 (2014).

67. *H. Frohlich. Theory of Dielectrics: Dielectric Constant and Dielectric Loss. Oxford, Clarendon Press, 1949* (n.d.).

68. Y. Zhai, Y. Ma, S. N. David, D. Zhao, R. Lou, G. Tan, R. Yang, and X. Yin, "Scalable-manufactured randomized glass-polymer hybrid metamaterial for daytime radiative cooling," Science (80-.). **355**(6329), 1062–1066 (2017).

69. X. Sun, Y. Sun, Z. Zhou, M. A. Alam, and P. Bermel, "Radiative sky cooling: Fundamental physics, materials, structures, and applications," Nanophotonics **6**(5), 997–1015 (2017).

70. D. Zhao, A. Aili, Y. Zhai, S. Xu, G. Tan, X. Yin, and R. Yang, "Radiative sky cooling: Fundamental principles, materials, and applications," Appl. Phys. Rev. **6**(2), 021306 (2019).

71. Y. Lu, Z. Chen, L. Ai, X. Zhang, J. Zhang, J. Li, W. Wang, R. Tan, N. Dai, and W. Song, "A Universal Route to Realize Radiative Cooling and Light Management in Photovoltaic Modules," Sol. RRL **1**(10), 1700084 (2017).

72. J. Jaramillo-Fernandez, G. L. Whitworth, J. A. Pariente, A. Blanco, P. D. Garcia, C. Lopez, and C. M. Sotomayor-Torres, "A Self-Assembled 2D Thermofunctional Material for Radiative Cooling," Small **15**(52), 1905290 (2019).

73. L. Zhu, A. Raman, K. X. Wang, M. A. Anoma, and S. Fan, "Radiative cooling of solar cells," Optica **1**(1), 32 (2014).

74. L. Long, Y. Yang, and L. Wang, "Simultaneously enhanced solar absorption and radiative cooling with thin silica micro-grating coatings for silicon solar cells," Sol. Energy Mater. Sol. Cells **197**, 19–24 (2019).

75. J. long Kou, Z. Jurado, Z. Chen, S. Fan, and A. J. Minnich, "Daytime Radiative Cooling Using Near-Black Infrared Emitters," ACS Photonics **4**(3), 626–630 (2017).

76. S. Y. Jeong, C. Y. Tso, Y. M. Wong, C. Y. H. Chao, and B. Huang, "Daytime passive radiative cooling by ultra emissive bio-inspired polymeric surface," Sol. Energy Mater. Sol. Cells **206**, 110296 (2020).

77. X. Nie, Y. Yoo, H. Hewakuruppu, J. Sullivan, A. Krishna, and J. Lee, "Cool White Polymer Coatings based on Glass Bubbles for Buildings," Sci. Rep. **10**(1), 1–10 (2020).

78. E. Lee and T. Luo, "Black body-like radiative cooling for flexible thin-film solar cells," Sol. Energy Mater. Sol. Cells **194**, 222–228 (2019).

79. A. R. Gentle and G. B. Smith, "Radiative heat pumping from the Earth using surface phonon resonant nanoparticles," Nano Lett. **10**(2), 373–379 (2010).

80. A. W. Harrison and M. R. Walton, "Radiative cooling of TiO2 white paint," Sol. Energy **20**(2), 185–188 (1978).

81. B. Orel, M. K. Gunde, and A. Krainer, "Radiative cooling efficiency of white pigmented paints," Sol. Energy **50**(6), 477–482 (1993).

82. C. N. Suryawanshi and C. T. Lin, "Radiative cooling: Lattice quantization and surface emissivity in thin coatings," ACS Appl. Mater. Interfaces **1**(6), 1334–1338 (2009).

83. J. Mandal, Y. Fu, A. C. Overvig, M. Jia, K. Sun, N. N. Shi, H. Zhou, X. Xiao, N. Yu, and Y. Yang, "Hierarchically porous polymer coatings for highly efficient passive daytime radiative cooling," Science (80-.). **362**(6412), 315–319 (2018).

84. G. Perrakis, A. C. Tasolamprou, G. Kenanakis, E. N. Economou, S. Tzortzakis, and M. Kafesaki, "Ultraviolet radiation impact on the efficiency of commercial crystalline silicon-based photovoltaics: a theoretical thermal-electrical study in realistic device architectures," OSA Contin. **3**(6), 1436 (2020).

85. B. Zhao, M. Hu, X. Ao, Q. Xuan, and G. Pei, "Comprehensive photonic approach for diurnal photovoltaic and nocturnal radiative cooling," Sol. Energy Mater. Sol. Cells **178**, 266–272 (2018).

86. T. S. Safi and J. N. Munday, "Improving photovoltaic performance through radiative cooling in both terrestrial and extraterrestrial environments," Opt. Express **23**(19), A1120 (2015).

87. W. Li, S. Buddhiraju, and S. Fan, "Thermodynamic limits for simultaneous energy harvesting from the hot sun and cold outer space," Light Sci. Appl. **9**(1), 2047–7538 (2020).

88. T. Saga, "Advances in crystalline silicon solar cell technology for industrial mass production," NPG Asia Mater. **2**(3), 96–102 (2010).

89. A. Polman, M. Knight, E. C. Garnett, B. Ehrler, and W. C. Sinke, "Photovoltaic materials: Present efficiencies and future challenges," Science (80-.). **352**(6283), aad4424–aad4424 (2016).

90. U. Wurfel, A. Cuevas, and P. Wurfel, "Charge Carrier Separation in Solar Cells," IEEE J. Photovoltaics **5**(1), 461–469 (2015).

91. S. Roy Chowdhury and H. Saha, "Maximum power point tracking of partially shaded solar photovoltaic arrays," in *Solar Energy Materials and Solar Cells* (2010), **94**(9), pp. 1441–1447.

92. F. J. Castano, D. Morecroft, M. Cascant, H. Yuste, M. W. P. E. Lamers, A. A. Mewe, I. G. Romijn, E. E. Bende, Y. Komatsu, A. W. Weeber, and I. Cesar, "Industrially feasible >19% efficiency IBC cells for pilot line processing," in *2011 37th IEEE Photovoltaic Specialists Conference* (IEEE, 2011), pp. 001038–001042.

93. P. Singh, S. N. Singh, M. Lal, and M. Husain, "Temperature dependence of I–V characteristics and performance parameters of silicon solar cell," Sol. Energy Mater. Sol. Cells **92**(12), 1611–1616 (2008).

94. O. Dupré, R. Vaillon, and M. A. Green, "Physics of the temperature coefficients of solar cells," Sol. Energy Mater. Sol. Cells **140**, 92–100 (2015).

95. M. Wolf and H. Rauschenbach, "Series resistance effects on solar cell measurements," Adv. Energy Convers. **3**(2), 455–479 (1963).

96. H. Steinkemper, M. Hermle, and S. W. Glunz, "Comprehensive simulation study of industrially relevant silicon solar cell architectures for an optimal material parameter choice," Prog. Photovoltaics Res. Appl. **24**(10), 1319–1331 (2016).

97. H. Steinkemper, I. Geisemeyer, M. C. Schubert, W. Warta, and S. W. Glunz, "Temperature-Dependent Modeling of Silicon Solar Cells-Eg, ni, Recombination, and VOC," IEEE J. Photovoltaics **7**(2), 450–457 (2017).

98. R. Vaillon, O. Dupré, R. B. Cal, and M. Calaf, "Pathways for mitigating thermal losses in solar photovoltaics," Sci. Rep. **8**(1), 1–9 (2018).

99. T. Tiedje, E. Yablonovitch, G. D. Cody, and B. G. Brooks, "Limiting efficiency of silicon solar cells," IEEE Trans. Electron Devices **31**(5),

711–716 (1984).

100. M. A. Green, "Limits on the open-circuit voltage and efficiency of silicon solar cells imposed by intrinsic Auger processes," IEEE Trans. Electron Devices **31**(5), 671–678 (1984).

101. K. G. Svantesson and N. G. Nilsson, "The temperature dependence of the Auger recombination coefficient of undoped silicon," J. Phys. C Solid State Phys. **12**(23), 5111–5120 (1979).

102. A. Richter, M. Hermle, and S. W. Glunz, "Reassessment of the limiting efficiency for crystalline silicon solar cells," IEEE J. Photovoltaics **3**(4), 1184–1191 (2013).

103. K. Misiakos and D. Tsamakis, "Accurate measurements of the silicon intrinsic carrier density from 78 to 340 K," J. Appl. Phys. **74**(5), 3293–3297 (1993).

104. P. P. Altermatt, "Models for numerical device simulations of crystalline silicon solar cells - A review," J. Comput. Electron. **10**(3), 314–330 (2011).

105. O. Breitenstein, "Understanding the current-voltage characteristics of industrial crystalline silicon solar cells by considering inhomogeneous current distributions," Opto-Electronics Rev. **21**(3), 259–282 (2013).

106. T. S. Safi and J. N. Munday, "Improving photovoltaic performance through radiative cooling in both terrestrial and extraterrestrial environments," Opt. Express **23**(19), A1120 (2015).

107. T. Markvart, "Thermodynamics of losses in photovoltaic conversion," Appl. Phys. Lett. **91**(6), 064102 (2007).

108. L. C. Hirst and N. J. Ekins-Daukes, "Fundamental losses in solar cells," Prog. Photovoltaics Res. Appl. **19**(3), 286–293 (2011).

109. Y. Xu, T. Gong, and J. N. Munday, "The generalized Shockley-Queisser limit for nanostructured solar cells," Sci. Rep. **5**(1), 1–9 (2015).

110. E. Yablonovitch, "STATISTICAL RAY OPTICS.," in *Journal of the Optical Society of America* (Optical Society of America, 1982), **72**(7), pp. 899–907.

111. O. D. Miller, E. Yablonovitch, and S. R. Kurtz, "Strong internal and external luminescence as solar cells approach the Shockley-Queisser limit," IEEE J. Photovoltaics **2**(3), 303–311 (2012).

112. I. Schnitzer, E. Yablonovitch, C. Caneau, and T. J. Gmitter,

"Ultrahigh spontaneous emission quantum efficiency, 99.7% internally and 72% externally, from AlGaAs/GaAs/AlGaAs double heterostructures," Appl. Phys. Lett. **62**(2), 131–133 (1993).

113. T. Kirchartz, U. Rau, M. Kurth, J. Mattheis, and J. H. Werner, "Comparative study of electroluminescence from Cu(In,Ga)Se2 and Si solar cells," Thin Solid Films **515**(15 SPEC. ISS.), 6238–6242 (2007).

114. "NeON R | NeON | Products | Solar | Business | LG Global," https://www.lg.com/global/business/neon-r.

115. "The SunPower Maxeon ® Solar Cell Conventional Panel SunPower ® X-Series 12% More Power in Year 25 SunPower ® E-Series and X-Series Conventional Panel," (n.d.).

116. "Eagle 72M G2 – JinkoSolar US," https://jinkosolar.us/product/eagle-72m-g2/.

117. S. Dubey, J. N. Sarvaiya, and B. Seshadri, "Temperature Dependent Photovoltaic (PV) Efficiency and Its Effect on PV Production in the World – A Review," Energy Procedia **33**, 311–321 (2013).

118. P. Wurfel, "The chemical potential of radiation," J. Phys. C Solid State Phys. **15**(18), 3967–3985 (1982).

119. K. R. McIntosh, J. N. Cotsell, J. S. Cumpston, A. W. Norris, N. E. Powell, and B. M. Ketola, "An optical comparison of silicone and EVA encapsulants for conventional silicon PV modules: A ray-tracing study," in *2009 34th IEEE Photovoltaic Specialists Conference (PVSC)* (IEEE, 2009), pp. 000544–000549.

120. D. D. Smith, P. J. Cousins, A. Masad, S. Westerberg, M. Defensor, R. Ilaw, T. Dennis, R. Daquin, N. Bergstrom, A. Leygo, X. Zhu, B. Meyers, B. Bourne, M. Shields, and D. Rose, "SunPower's Maxeon Gen III solar cell: High efficiency and energy yield," in *2013 IEEE 39th Photovoltaic Specialists Conference (PVSC)* (IEEE, 2013), pp. 0908–0913.

121. I. Subedi, T. J. Silverman, M. G. Deceglie, and N. J. Podraza, "Emissivity of solar cell cover glass calculated from infrared reflectance measurements," Sol. Energy Mater. Sol. Cells **190**, 98–102 (2019).

122. A. Riverola, A. Mellor, D. Alonso Alvarez, L. Ferre Llin, I. Guarracino, C. N. Markides, D. J. Paul, D. Chemisana, and N. Ekins-Daukes, "Mid-infrared emissivity of crystalline silicon solar cells," Sol. Energy Mater. Sol. Cells **174**, 607–615 (2018).

123. T. J. Silverman, M. G. Deceglie, I. Subedi, N. J. Podraza, I. M. Slauch, V. E. Ferry, and I. Repins, "Reducing Operating Temperature in Photovoltaic Modules," IEEE J. Photovoltaics **8**(2), 532–540 (2018).

124. M. R. Vogt, H. Schulte-Huxel, M. Offer, S. Blankemeyer, R. Witteck, M. Köntges, K. Bothe, and R. Brendel, "Reduced Module Operating Temperature and Increased Yield of Modules with PERC Instead of Al-BSF Solar Cells," IEEE J. Photovoltaics **7**(1), 44–50 (2017).

125. D. H. Neuhaus and A. Münzer, "Industrial silicon wafer solar cells," Adv. Optoelectron. **2007**, (2007).

126. S. Dubey, G. S. Sandhu, and G. N. Tiwari, "Analytical expression for electrical efficiency of PV/T hybrid air collector," Appl. Energy **86**(5), 697–705 (2009).

127. M. W. Davis, A. H. Fanney, and B. P. Dougherty, "Prediction of Building Integrated Photovoltaic Cell Temperatures," J. Sol. Energy Eng. **123**(3), 200 (2001).

128. C. N. Santos, D. de S. Meneses, V. Montouillout, and P. Echegut, "Infrared emissivity spectroscopy of a soda-lime silicate glass up to the melt," (2012).

129. "Solite - Patterned Glass - Patterned Glass by AGC Solar," https://www.energy-xprt.com/products/solite-patterned-glass-198869.

130. E. R. Schleiger, "Measurement of Total Hemispherical Emittance of Transparent Materials at Low Temperature," Appl. Opt. **6**(5), 919 (1967).

131. M. C. C. de Oliveira, A. S. A. Diniz Cardoso, M. M. Viana, and V. de F. C. Lins, "The causes and effects of degradation of encapsulant ethylene vinyl acetate copolymer (EVA) in crystalline silicon photovoltaic modules: A review," Renew. Sustain. Energy Rev. **81**, 2299–2317 (2018).

132. P. Hacke, S. Spataru, K. Terwilliger, G. Perrin, S. Glick, S. Kurtz, and J. Wohlgemuth, "Accelerated Testing and Modeling of Potential-Induced Degradation as a Function of Temperature and Relative Humidity," IEEE J. Photovoltaics **5**(6), 1549–1553 (2015).

133. G. M. Kimball, S. Yang, and A. Saproo, "Global acceleration factors for damp heat tests of PV modules," in *Conference Record of the IEEE Photovoltaic Specialists Conference* (Institute of Electrical and Electronics Engineers Inc., 2016), **2016-November**, pp. 101–105.

134. I. M. Slauch, M. G. Deceglie, T. J. Silverman, and V. E. Ferry, "Spectrally Selective Mirrors with Combined Optical and Thermal Benefit for Photovoltaic Module Thermal Management," ACS Photonics **5**(4), 1528–1538 (2018).

135. H. Huang, J. Lv, Y. Bao, R. Xuan, S. Sun, S. Sneck, S. Li, C. Modanese, H. Savin, A. Wang, and J. Zhao, "20.8% industrial PERC solar cell: ALD Al2O3 rear surface passivation, efficiency loss mechanisms analysis and roadmap to 24%," Sol. Energy Mater. Sol. Cells **161**, 14–30 (2017).

136. R. G. . J. Ross, Ross, R. G., and Jr., "Technology developments toward 30-year-life of photovoltaic modules," pvsp 464–472 (1984).

137. B. Ottersböck, G. Oreski, and G. Pinter, "Comparison of different microclimate effects on the aging behavior of encapsulation materials used in photovoltaic modules," Polym. Degrad. Stab. **138**, 182–191 (2017).

138. A. Ndiaye, A. Charki, A. Kobi, C. M. F. Kébé, P. A. Ndiaye, and V. Sambou, "Degradations of silicon photovoltaic modules: A literature review," Sol. Energy **96**, 140–151 (2013).

139. D. C. Jordan and S. R. Kurtz, "Photovoltaic Degradation Rates-an Analytical Review," Prog. Photovoltaics Res. Appl. **21**(1), 12–29 (2013).

140. M. D. Kempe, T. Moricone, M. Kilkenny, M. D. Kempe, T. Moricone, and M. Kilkenny, *Effects of Cerium Removal from Glass on Photovoltaic Module Performance and Stability Preprint Effects of Cerium Removal From Glass on Photovoltaic Module Performance and Stability* (2009).

141. G. Perrakis, A. C. Tasolamprou, G. Kenanakis, E. N. Economou, S. Tzortzakis, and M. Kafesaki, "Passive radiative cooling and other photonic approaches for the temperature control of photovoltaics: a comparative study for crystalline silicon-based architectures," Opt. Express **28**(13), 18548 (2020).

142. W. J. Yang, Z. Q. Ma, X. Tang, C. B. Feng, W. G. Zhao, and P. P. Shi, "Internal quantum efficiency for solar cells," Sol. Energy **82**(2), 106–110 (2008).

143. J.-W. Cho, S.-J. Park, S.-J. Park, Y.-B. Kim, K.-Y. Kim, D. Bae, and S.-K. Kim, "Scalable On-Chip Radiative Coolers for Concentrated Solar Energy Devices," ACS Photonics (2020).

144. X. Sun, T. J. Silverman, Z. Zhou, M. R. Khan, P. Bermel, and M. A.

Alam, "Optics-Based Approach to Thermal Management of Photovoltaics: Selective-Spectral and Radiative Cooling," IEEE J. Photovoltaics **7**(2), 566–574 (2017).

145. B. Zhao, M. Hu, X. Ao, and G. Pei, "Performance analysis of enhanced radiative cooling of solar cells based on a commercial silicon photovoltaic module," Sol. Energy **176**, 248–255 (2018).

146. Z. Wang, D. Kortge, J. Zhu, Z. Zhou, H. Torsina, C. Lee, and P. Bermel, "Lightweight, Passive Radiative Cooling to Enhance Concentrating Photovoltaics," Joule **4**(12), 2702–2717 (2020).

147. A. Papadopoulos, E. Skoulas, A. Mimidis, G. Perrakis, G. Kenanakis, G. D. Tsibidis, and E. Stratakis, "Biomimetic Omnidirectional Antireflective Glass via Direct Ultrafast Laser Nanostructuring," Adv. Mater. **31**(32), 1901123 (2019).

148. Y. An, C. Sheng, and X. Li, "Radiative cooling of solar cells: Opto-electro-thermal physics and modeling," Nanoscale **11**(36), 17073–17083 (2019).

149. V. G. Kravets, F. Schedin, and A. N. Grigorenko, "Fine structure constant and quantized optical transparency of plasmonic nanoarrays," Nat. Commun. **3**(1), 1–5 (2012).

150. F. J. García-Vidal and L. Martín-Moreno, "Transmission and focusing of light in one-dimensional periodically nanostructured metals," Phys. Rev. B - Condens. Matter Mater. Phys. **66**(15), 1–10 (2002).

151. J. Morikawa, M. Ryu, G. Seniutinas, A. Balčytis, K. Maximova, X. Wang, M. Zamengo, E. P. Ivanova, and S. Juodkazis, "Nanostructured antireflective and thermoisolative cicada wings," Langmuir **32**(18), 4698–4703 (2016).

152. A. Syafiq, B. Vengadaesvaran, N. A. Rahim, A. K. Pandey, A. R. Bushroa, K. Ramesh, and S. Ramesh, "Transparent self-cleaning coating of modified polydimethylsiloxane (PDMS) for real outdoor application," Prog. Org. Coatings **131**, 232–239 (2019).

153. H. Price, E. Lüpfert, D. Kearney, E. Zarza, G. Cohen, R. Gee, and R. Mahoney, "Advances in parabolic trough solar power technology," J. Sol. Energy Eng. Trans. ASME **124**(2), 109–125 (2002).

154. S. Basu, B. J. Lee, and Z. M. Zhang, "Infrared radiative properties of heavily doped silicon at room temperature," J. Heat Transfer **132**(2), 1–8 (2010).

155. E. Skoulas, A. C. Tasolamprou, G. Kenanakis, and E. Stratakis,

"Laser induced periodic surface structures as polarizing optical elements," Appl. Surf. Sci. 148470 (2020).

156. M. Rubin, "Optical properties of soda lime silica glasses," Sol. Energy Mater. **12**(4), 275–288 (1985).

157. A. Rudenko, J. P. Colombier, S. Höhm, A. Rosenfeld, J. Krüger, J. Bonse, and T. E. Itina, "Spontaneous periodic ordering on the surface and in the bulk of dielectrics irradiated by ultrafast laser: A shared electromagnetic origin," Sci. Rep. **7**(1), 1–14 (2017).

158. S. Gräf, C. Kunz, and F. Müller, "Formation and Properties of Laser-Induced Periodic Surface Structures on Different Glasses," Materials (Basel). **10**(8), 933 (2017).

159. R. H. Siddique, G. Gomard, and H. Hölscher, *The Role of Random Nanostructures for the Omnidirectional Anti-Reflection Properties of the Glasswing Butterfly* (Nature Publishing Group, 2015), **6**(1).

160. M. R. Vogt, "Vogt, M. R. Ph.D. Thesis, Leibniz University of Hanover: Hanover, Germany," Ph.D. Thesis, Leibniz Univ. Hanover Hanover, Ger. (2015).

161. S. Diwania, S. Agrawal, A. S. Siddiqui, and S. Singh, "Photovoltaic–thermal (PV/T) technology: a comprehensive review on applications and its advancement," Int. J. Energy Environ. Eng. **11**(1), 33–54 (2020).

162. E. A. Goldstein, A. P. Raman, and S. Fan, "Sub-ambient non-evaporative fluid cooling with the sky," Nat. Energy **2**(9), 1–7 (2017).

163. Z. Zhou, Z. Wang, and P. Bermel, "Radiative cooling for low-bandgap photovoltaics under concentrated sunlight," Opt. Express **27**(8), A404 (2019).

9

SUPPLEMENTARY RESEARCH: PLASMONICS-INDUCED ABSORPTION IN THIN-FILM DEVICES

9.1 INTRODUCTION

Lastly, in the general context of light-matter interaction enhancement, we explore light control via plasmonic resonances. The plasmonic resonance-induced strong scattering or electromagnetic field enhancement in the active layer can counteract the short interaction time with the incoming wave in thin-film devices and thus improve the absorption efficiency for various applications.

In the present thesis, aside from conventional silicon-based PVs, we additionally explore emerging PV technologies such as the highly efficient metal halide perovskite-based thin-film solar cells, which are promising routes for reducing the levelized cost of electricity [7]. As we show in the appended publication entitled "Efficient and environmental-friendly perovskite solar cells via embedding plasmonic nanoparticles: an optical simulation study on realistic device architectures", the short interaction time of the incoming light in perovskite thin-films can be counteracted via plasmonic-induced light-trapping schemes. For instance, confining light in space, or inducing strong scattering of light, providing access to guided modes, are promising routes to enhance the absorption efficiency in perovskite thin-film solar cells.

Finally, we demonstrate that sensing applications can also be benefited from plasmonic enhancement. Structuring metal surfaces on the nanoscale has been shown to alter their scattering response, inducing, e.g., strong absorption peaks, own to the excitation of surface plasmon resonances. Consequently, we conduct a thorough numerical analysis to gain physical insight on how the key structural parameters affect the optical response and identify the designs

leading to strong absorption resonances with broad/narrow spectral and angular bandwidths, both of which are highly desirable in practical absorber/sensing applications. The details of the pertinent research are given in the appended publication entitled “Perfect optical absorption with nanostructured metal films: design and experimental demonstration”.

Perfect optical absorption with nanostructured metal films: design and experimental demonstration

GEORGE PERRAKIS,[1,2] ODYSSEAS TSILIPAKOS,[1,*] GEORGE KENANAKIS,[1,5] MARIA KAFESAKI,[1,2] COSTAS M. SOUKOULIS,[1,3] AND ELEFTHERIOS N. ECONOMOU[1,4]

[1] *Institute of Electronic Structure and Laser, FORTH, GR-71110 Heraklion, Crete, Greece*
[2] *Department of Materials Science and Technology, University of Crete, GR-71003 Heraklion, Crete, Greece*
[3] *Ames Laboratory—U.S. DOE and Department of Physics and Astronomy, Iowa State University, Ames, Iowa 50011, USA*
[4] *Department of Physics, University of Crete, GR-71003 Heraklion, Crete, Greece*
[5] *gkenanak@iesl.forth.gr*
[*] *otsilipakos@iesl.forth.gr*

Abstract: Structuring metal surfaces on the nanoscale has been shown to alter their fundamental processes like reflection or absorption by supporting surface plasmon resonances. Here, we propose metal films with subwavelength rectangular nanostructuring that perfectly absorb the incident radiation in the optical regime. The structures are fabricated with low-cost nanoimprint lithography and thus constitute an appealing alternative to elaborate absorber designs with complex meta-atoms or multilayer structuring. We conduct a thorough numerical analysis to gain physical insight on how the key structural parameters affect the optical response and identify the designs leading to broad spectral and angular bandwidths, both of which are highly desirable in practical absorber applications. Subsequently, we fabricate and measure the structures with an FT-IR spectrometer demonstrating very good agreement with theory. Finally, we assess the performance of the proposed structures as sensing devices by quantifying the dependence of the absorption peak frequency position on the superstrate material.

1. Introduction

Surface plasmon polaritons (SPPs) are electromagnetic surfaces waves coupled to free electron oscillations [1–4]. They propagate along a metal-dielectric interface and exhibit an exponential decay of the field components away from it [1,2,4]. Free space radiation cannot couple directly to propagating SPPs due to the wavevector mismatch between them, i.e., the dispersion relation of SPP waves lies on the right of the light line. Thus, the excitation of SPPs exploiting corrugated metal-dielectric surfaces which can satisfy momentum conservation has been a subject of continuous research.

Following the seminal work of Raether [1], metallic corrugated surfaces and gratings have been investigated for an abundance of applications. Besides efficient coupling to propagating SPPs [5–7], metallic gratings can be used as Bragg reflectors to route propagating signals in guided wave circuits [8–11] or form wavelength-selective components [12–14]. In addition, they can serve as diffractive optical elements deflecting free-space beams to the desired direction [15,16]. Finally, they have been examined for demonstrating SPP-based sensors exploiting the field enhancement on the metallic-dielectric interface [17,18].

In this work, we focus on a different application, that of perfect absorption. Recently-proposed metamaterial-based perfect absorbers require elaborate designs with precisely structured metal inclusions and/or multilayer topologies [19–25]. Achieving efficient operation with simpler structures that do not involve elaborate fabrication techniques is thus of high importance, as highlighted in [23]. Here, we design metal films with rectangular

nanostructuring (i.e., binary metallic gratings with subwavelength pitch) that can perfectly absorb incident radiation without any reflections. The structures are designed to operate in the visible region. We propose broadband and wide-angle designs that are suitable for practical perfect absorption applications. We subsequently fabricate selected samples using nanoimprint lithography: a low-cost process that is particularly advantageous for producing large scale samples, something not possible with other fabrication techniques. We measure their optical response using Fourier-transform infrared spectroscopy and find excellent agreement between measured and simulated data. We are thus able to demonstrate experimentally an optical perfect absorber that offers excellent performance in terms of absorption efficiency and angular bandwidth and at the same time is a very simple structure that can be fabricated with a low cost fabrication technique. In addition, we find that the spectral position of the absorption peak is sensitive to the superstrate material. As a result, we highlight the possibility of utilizing our structures for sensing applications, thus allowing for multiple functionalities with the same structure by properly selecting the geometrical parameters in the design stage.

Other routes to simple and efficient absorber designs have been proposed in the literature. One prominent example is high-impedance structures, such as the mushroom structure [27,28]. Their main characteristic is wide-angle absorption, achieved by suppressing the spatial dispersion (angular dependence) of the surface input impedance. Fabricating mushroom structures for the microwave frequency regime is straightforward by means of plated through vias on standard printed circuit boards. However, this is not the case in the optical regime we are targeting. Another prominent example is planar, uniform multi-layer structures comprising lossy dielectric and metal layers [29,30]. In these cases, it becomes necessary to process different materials for covering different frequencies of operation [30]. Having a structure made of a single material that can tune its operation frequency by means of the geometrical parameters of the patterning is thus beneficial from a fabrication standpoint.

The remainder of the paper is organized as follows: The structure under study is presented in Section 2 along with the relevant geometrical and material parameters. In Section 3 we conduct a thorough numerical analysis to gain insight on how the key structural parameters affect the optical response and identify practical designs with broad spectral and angular bandwidth. Section 4 discusses the fabrication details and presents the experimental measurements verifying the numerical simulations. Finally, in Section 5 we quantify the dependence of the absorption peak position on the superstrate material.

2. Geometric and material parameters

The structure under study is the binary (i.e., rectangular) grating depicted in Fig. 1. It consists of metallic ridges of width s and height h on top of a metallic substrate with thickness t. In the remainder of the paper we assume $t = 200$ nm meaning that for the wavelengths of interest (400-1200nm) the structure is opaque and no transmission is allowed. The periodicity (pitch) is denoted by a. It is set to 400 nm (or lower) meaning that in the said wavelength range only the zeroth diffraction order is propagating (normal incidence). For the material parameters, the metal is silver and the relative permittivity, ε_m, is given by a Drude model, $\varepsilon_m = 1 - \omega_p^2 / (\omega^2 + i\omega\gamma)$, with plasma frequency $\omega_p = 13.2 \cdot 10^{15}$ rad/s and collision rate $\gamma = 43.33 \cdot 10^{13}$ rad/s [31]. The relative permittivity of the superstrate material is ε_s and is initially set to 1 (air).

In what follows, we assess the optical response by illuminating the structure with a plane wave of TM polarization, $\mathbf{H} = H_z \hat{\mathbf{z}}$, impinging at an incidence angle θ (Fig. 1). We calculate or measure the reflection coefficient and subsequently determine the absorption through $A = 1 - R$ since transmission through the structure is zero.

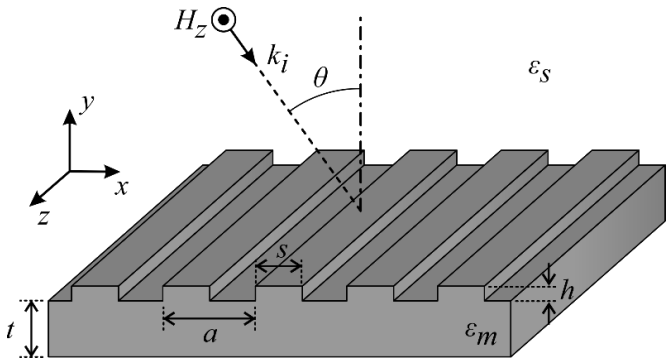

Fig. 1. Binary metallic grating illuminated by a TM polarized plane wave impinging at an incidence angle θ. All relevant geometric parameters (pitch *a*, ridge width *s*, and ridge height *h*) are included. *t* = 200 nm throughout the paper.

3. Optical response: perfect absorption in the visible regime

For calculating the optical response we conduct full-wave electromagnetic simulations using commercially available software (CST Microwave Studio, Computer Simulation Technology GmbH, Darmstadt, Germany). We start from normal incidence ($\theta = 0$) and vary the ridge height, h, while keeping the width, s, constant at 250 nm. The results are depicted in Fig. 2(a). The presence of a surface corrugation results in the excitation of SPPs on the metal-dielectric interface. This manifests as a reflection dip which translates into an absorption peak. For $h = 10$ nm, the grating can be considered a slight perturbation of the planar interface. This can be verified by the electric field distribution (real part of E_y component) which is included in Fig. 2(a) as an inset. As a result, the wavelength of the absorption peak is at 432 nm, very close to 424 nm calculated from the Bragg condition, $k_{\mathrm{SPP}} = k_0\sqrt{\varepsilon_s}\sin\theta + m(2\pi/a)$, and the well-known dispersion relation for SPPs on metal-dielectric interfaces [1], which for normal incidence ($\theta = 0$) lead to:

$$k_{\mathrm{SPP}} = \frac{2\pi}{a} \Rightarrow k_0\sqrt{\frac{\varepsilon_s\varepsilon_m(\omega)}{\varepsilon_s + \varepsilon_m(\omega)}} = \frac{2\pi}{a}, \tag{1}$$

where $k_0 = \omega / c_0$ is the wavenumber in vacuum and $\varepsilon_s = 1$ for an air superstrate.

By increasing the ridge height the position of the absorption peak redshifts [Fig. 2(a)]. In addition, the maximum absorption increases reaching 100% for $h = 20$ nm, indicating that the radiation reflected directly from the surface (the zeroth diffraction order) and the radiation out-coupled (scattered back to the radiation zone) from the propagating SPPs are equal and exactly out of phase. For $h \geq 30$ nm the absorption peak starts decreasing again since we deviate from the condition of perfect destructive interference leading to nonzero reflection. In addition, tuning the ridge height results in a strong variation of the absorption linewidth.

The increased absorption bandwidth observed for $h = 50$ nm in Fig. 2(a) is beneficial for perfect absorption applications. We thus retain this height value and vary the ridge width (i.e., the second design parameter) aiming to increase the absorption efficiency. The results are depicted in Fig. 2(b). Indeed, as the ridge width increases we observe an increase in the absorption efficiency. To reveal the origin of this increase we plot the *E*-field norm distribution for three characteristic values of *s*: 250, 350, and 375 nm. As can be seen in Fig. 2(c), as *s* increases the field becomes tightly confined in the slot region between adjacent ridges. The field enhancement compared to the incident amplitude increases accordingly: 30,

40, and 45 in the three cases, respectively. The excitation of localized slot modes in metallic gratings has also been reported in [17,32]. The increased field enhancement associated with squeezing the field into a smaller slot volume leads to stronger absorption ($A \sim |\mathbf{E}|^2$). We note that for $s > 375\,\text{nm}$ the absorption peak starts decreasing again (not shown) as the fields cannot be accommodated inside the nanoscale gaps.

In Fig. 2(d) we plot the maximum value of the absorption spectrum for any parameter combination in the entire (*s*, *h*) parametric space and in Fig. 2(e) the corresponding wavelength where it is observed. These plots can serve as a design guide for achieving perfect optical absorption with 100% efficiency at different wavelengths by properly tuning the geometrical parameters of the structure under study.

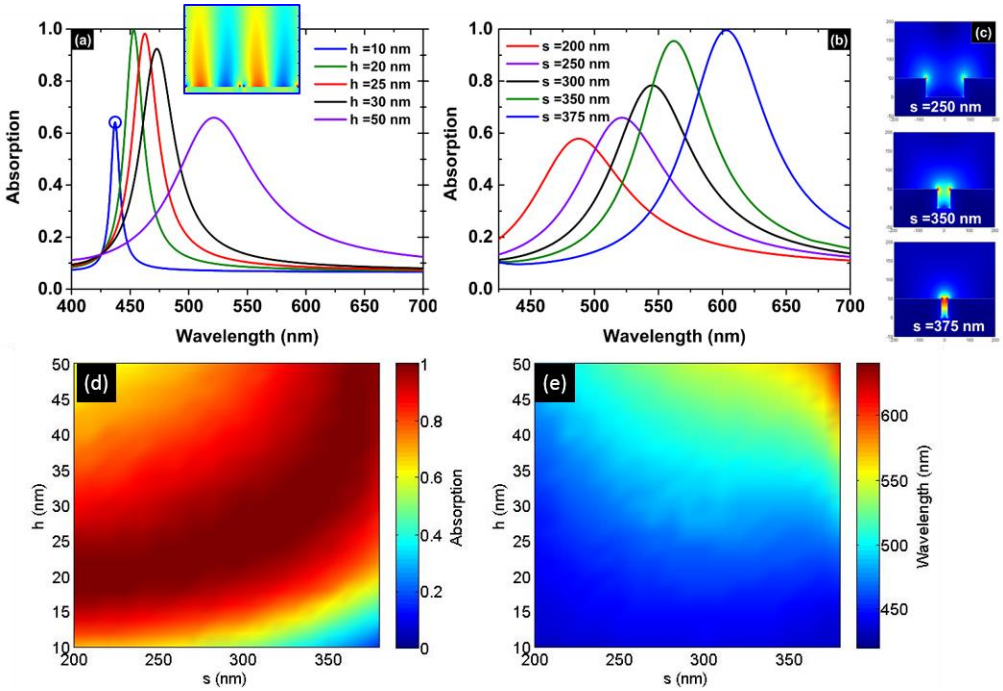

Fig. 2. (a) Absorption vs wavelength when varying the ridge height, *h*, while keeping the width constant at *s*=250 nm. (b) Absorption vs wavelength when varying the ridge width, *s*, while keeping the height constant at *h*=50 nm. (c) Electric field amplitude at the absorption peak (red denotes high values and blue low values). With increasing *s* the field becomes tightly confined in the slot and the field enhancement increases. (d) Maximum value of the absorption spectrum for any parameter combination in the entire (*s*, *h*) parametric space and (e) the corresponding wavelength where it is observed.

We are now interested in the performance of the proposed structure under oblique incidence, since this is important for practical perfect absorption applications. We first focus on the structure with $a = 400\,\text{nm}$, $h = 50\,\text{nm}$, and $s = 375\,\text{nm}$ that featured 100% absorption efficiency in Fig. 2(b). The incidence angle is varied up to 65° and the results are compiled in Fig. 3(a). The absorption remains quite high; however, the position of the peak moves to higher wavelengths and the absorption linewidth decreases. Note that as the incidence angle increases the onset of the first diffraction order approaches the wavelength of the main absorption peak and extra features are introduced in the absorption spectrum (lower wavelengths). Markers in Fig. 3(a) denote the analytically calculated onset of the first diffraction order, taking place when the respective reflected wavevector (normal component) becomes real. It should be noted when higher diffraction orders become propagating the

relation between reflection and absorption coefficients is modified to $A=1-\sum_m R_m$, where index *m* runs through the propagating diffraction orders. In analogy with the sharp features in the absorption spectrum when a higher reflection diffraction order becomes propagating observed here (Fig. 3), sharp features in the transmissivity from a grating of cylindrical particles have been associated with the emergence of a higher refraction diffraction order in [33].

In Fig. 3(b) we alter the design: we retain the s/a ratio constant at the optimum value (375/400=0.9375) found in Fig. 2(b), but modify the grating pitch, a, to 275 nm. This way, higher diffraction orders do not approach the vicinity of the perfect absorption peak near ~600nm even for very steep angles of incidence. As a result, the absorption peak shows exceptional robustness with incidence angle: the efficiency, position and linewidth of absorption remain unchanged for incidence angles up to 65°.

The results in Figs. 2 and 3 highlight the existence and hybridization of two types of resonances in metallic gratings, which have been identified in the literature [32]. More specifically, one type of resonance is primarily an SPP with the *E*-field located mainly on the top surface of the ridges [see inset in Fig. 2(a) for example]. The second type concerns localized resonances inside the metal slots. When these resonances are tightly confined and do not hybridize with the SPP-type resonances, they are characterized by flat (dispersionless) bands in the (k_x,ω) photonic band diagram of the periodic structure [32]. In other words, the position of the corresponding spectral absorption feature does not depend on the incidence angle, which is the case seen in Fig. 3(b). Intermediate scenarios where the localized modes hybridize with the SPP-type resonance leading to dependence of the absorption peak with the incidence angle are seen in Fig. 3(a) for example.

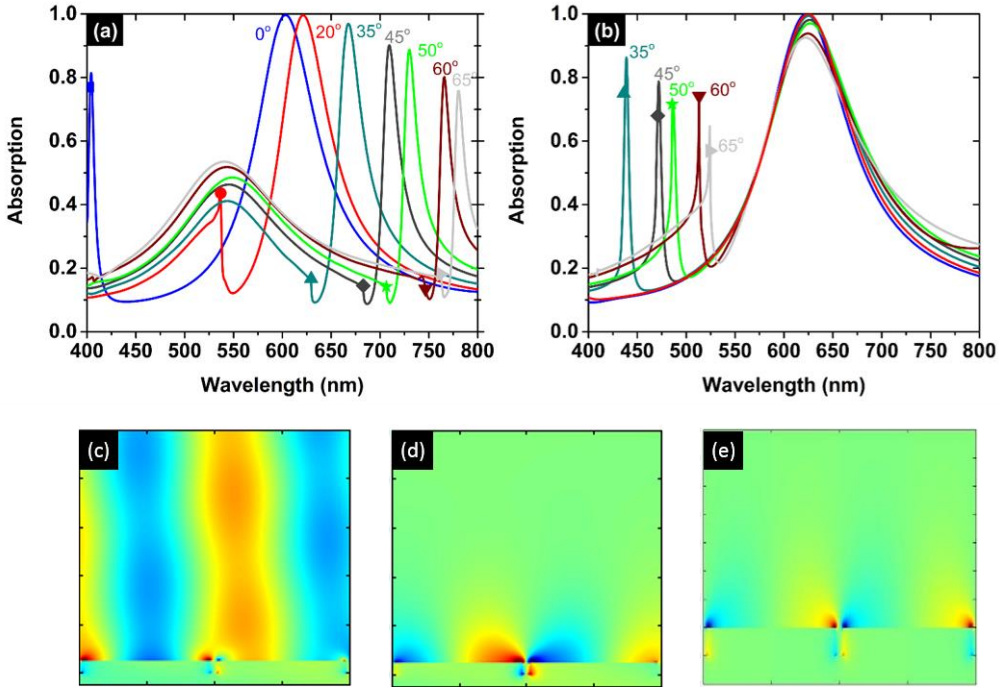

Fig. 3. (a) Absorption vs wavelength for varying incidence angle (TM polarization) when *a*=400 nm, *h*=50 nm and *s*=0.9375*a*=375 nm. The absorption remains high but the position and linewidth of the peak change. (b) Absorption vs wavelength for varying incidence angle when *a*=275 nm, *h*=50 nm and *s*=0.9375*a*= 258 nm. The efficiency, position and linewidth of absorption remain unchanged for incidence angles up to 65°. Markers denote the analytically calculated onset of the first diffraction order. Field distributions (real part of E_y component)

for three characteristic points: (c) At 536 nm on the 20-degree curve in panel (a). The first diffraction order has just become propagating and is leaving the structure at grazing angle. (d) At 621 nm on the 20-degree curve in panel (a).(e) At 625 nm on the 60-degree in panel (b).

To recapitulate, we have investigated how the key structural parameters (*a*, *h*, *s*) affect the optical response of our nanostructured metal film. Observing the results in Figs. 2, 3 one sees several opportunities for perfect absorption with the simple structure of a binary metallic grating. However, one should be careful in selecting the optimum design taking into account the absorption bandwidth and the robustness with incidence angle. The design in Fig. 3(b) satisfies both of these requirements by adopting a narrow slot region for confining the fields with increased enhancement and by opting for a short pitch value to avoid higher diffraction orders becoming propagating in the spectral vicinity of the absorption peak.

4. Experimental verification of perfect optical absorption

Next, we fabricate and measure two different samples in order to verify our proposed approach. Our structures were realized by means of ultraviolet nanoimprint lithography (UV-NIL). First, typical silicon (Si) master molds were realized by electron beam lithography and reactive ion etching steps. Each Si master mold was treated with an anti-adhesion coating to enhance the release properties of the mold during replication steps. Subsequently a soft PDMS (Sylgard 184, Dow Corning, USA) replica was fabricated by casting the PDMS pre-polymer against the relief structure of Si master molds. A 10:1 ratio (precursor: curing agent) was mixed and cured for 12 hours at 60 ^{0}C. The final PDMS mold was used as our working mold in the UV-NIL process. A thin layer of Ormocomp resist material (micro resist technology GmbH, Germany) was spin coated (3000 rpm for 1 min) on a silicon substrate while the PDMS mold and substrate were brought into physical contact. Once the cavities of the PDMS molds were filled, the assembly was exposed to soft air pressure (5bars) followed by a UV light (365 nm) exposure for 5 sec. Subsequently, our replicated structures were coated with a thin (200 nm) Ag layer by means of evaporation.

For the experimental electromagnetic characterization we performed FT-IR measurements using a Bruker Vertex 70v spectrometer with a collimated beam, attached to a Bruker HYPERION 2000 FT-IR microscope, and two calcite based Glan-Thompson linear polarizers, providing a >500:1 degree of polarization in a spectral range of 450nm. The above instrument was equipped with a Quartz beamsplitter and a room temperature RT-Silicon diode detector, in order to get both transmission and reflection measurements in a spectral range of 400-900 nm (25.000 – 11.100 cm^{-1}). A total of 100 scans were acquired with a scanner velocity of 10 kHz at a resolution of 8 cm^{-1}. The scans were coadded, apodized with the Blackman-Harris three-term function, and fast Fourier transformed with two level of zero filling to produce spectral data encoded at 0.2 cm^{-1} intervals.

The measured data are presented in Fig. 4 (solid curves) for two different designs and compared with the respective simulations (dashed curves). More specifically, Fig. 4(a) concerns the design (*a*, *h*, *s*) = (400 nm, 50 nm, 375 nm) and Fig. 4(b) the design (*a*, *h*, *s*) = (400 nm, 20 nm, 200 nm). In both cases, very good agreement between theory and experiment is observed, indicating the figh quality of the fabricated samples and validating the numerical simulations. Deviations in the absorption peak position are minimal and a slight discrepancy in the absorption linewidth can be attributed to sample roughness. The ripple in Fig. 4(b) is due to measuring near the limit of the FT-IR spectrometer's range. The surface morphology of the samples was studied by means of a field emission scanning electron microscope (FE-SEM, JEOL JSM-7000F). The SEM image appearing as an inset in Fig. 4(b) demonstrates that the actual dimensions of the fabricated sample are in excellent agreement with the nominal values.

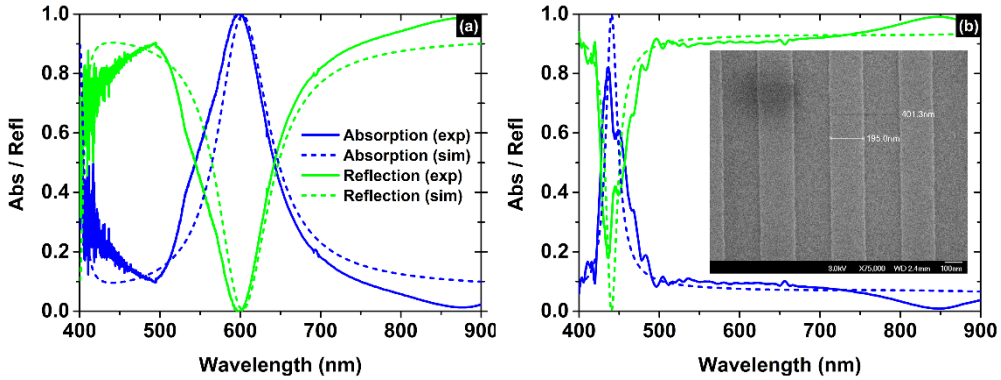

Fig. 4 Simulated and measured reflection and absorption spectra for (a) the design (a, h, s) = (400 nm, 50 nm, 375 nm) and (b) the design (a, h, s) = (400 nm, 20 nm, 200 nm). Excellent agreement between simulation and experiment is observed. The SEM image inset in panel (b) demonstrates that the actual dimensions of the fabricated sample are in excellent agreement with the nominal values.

5. Effect of superstrate material

In this section, we investigate the effect of the superstrate permittivity on the optical response of our proposed structure. We are interested in assessing the potential of the structure as a sensing platform. In Fig. 5 we examine different analytes (amines, acids, etc.) relevant for sensing applications. We focus on the design with $a = 400$ nm, $h = 20$ nm, and $s = 200$ nm examined in Fig. 4(b) since a smaller linewidth is preferable for sensing applications. As the superstrate permittivity changes (increases) the absorption peak experiences a significant shift towards higher wavelengths. More specifically, the absorption peaks shifts from $\lambda_{PA} = 440$ nm for air, to $\lambda_{PA} = 700$ nm for $C_4H_{11}N$ ($\varepsilon_r = 3.6$), $\lambda_{PA} = 793$ nm for $CHCl_3$ ($\varepsilon_r = 4.8$), and $\lambda_{PA} = 900$ nm for HCl ($\varepsilon_r = 6.35$). Importantly, the absorption efficiency is retained at 100%. As a result, tracking the position of the perfect absorption peak, appearing as a reflection dip in actual measurements, allows for identifying the permittivity of the material covering our binary metallic grating structure.

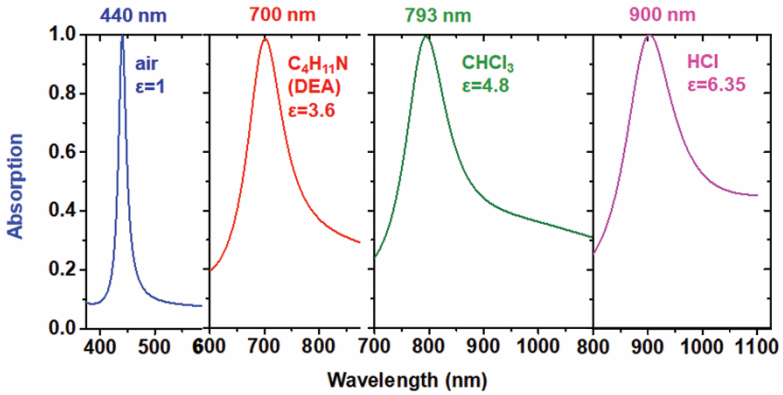

Fig. 5 Response of metallic binary grating with $(a, h, s) = (400\text{ nm}, 20\text{ nm}, 200\text{ nm})$ for different superstrate materials. The absorption peak is significantly shifted towards higher wavelengths while maintaining 100% absorption efficiency.

6. Conclusions

We have demonstrated, both theoretically and experimentally, perfect optical absorption using simple metallic films with a subwavelength rectangular nanostructuring. Such corrugated films can be easily fabricated with low-cost nanoimprint lithography and thus constitute an appealing alternative to elaborate absorber structures. We have conducted a thorough numerical analysis to identify the design that results in both broad absorption bandwidth and angle-independent performance, both of which are essential traits for an efficient absorber structure. To verify the theoretical results, two samples were fabricated and subsequently measured with an FT-IR spectrometer; very good agreement with the numerical simulations has been observed. Finally, we have assessed the potential of the proposed structures as refractive index sensing devices by examining the effect of the superstrate material on the absorption spectrum.

Funding

This work was supported by the European Research Council under ERC Advanced Grant no. 320081 (project PHOTOMETA), the European Union's Horizon 2020 Future Emerging Technologies call (FETOPEN-RIA) under Grant Agreement No. 736876 (project VISORSURF), and the ERA.Net RUS Plus project EXODIAGNOS.

7. References

1. H. Raether, *Surface Plasmons on Smooth and Rough Surfaces and on Gratings* (Springer-Verlag, 1988).
2. E. N. Economou, "Surface plasmons in thin films," Phys. Rev. **182**, 539–554 (1969).
3. W. L. Barnes, A. Dereux, and T. W. Ebbesen, "Surface plasmon subwavelength optics," Nature **424**, 824–830 (2003).
4. O. Tsilipakos, T. V. Yioultsis, and E. E. Kriezis, "Theoretical analysis of thermally tunable microring resonator filters made of dielectric-loaded plasmonic waveguides," J. Appl. Phys. **106**, 093109 (2009).
5. A. V Krasavin and N. I. Zheludev, "Active plasmonics : Controlling signals in Au/Ga waveguide using nanoscale structural transformations," Appl. Phys. Lett. **84**, 1416–1418 (2004).
6. I. P. Radko, S. I. Bozhevolnyi, G. Brucoli, L. Martín-Moreno, F. J. García-Vidal, and A. Boltasseva, "Efficiency of local surface plasmon polariton excitation on ridges," Phys. Rev. B - Condens. Matter Mater. Phys. **78**, 115115 (2008).
7. V. M. Shalaev and S. Kawata, eds., *Nanophotonics with Surface Plasmons* (Elsevier, 2007).
8. M. U. González, J.-C. Weeber, A.-L. Baudrion, A. Dereux, A. L. Stepanov, J. R. Krenn, E. Devaux, and T. W. Ebbesen, "Design, near-field characterization, and modeling of 45 surface-plasmon Bragg mirrors," Phys. Rev. B **73**, 155416 (2006).
9. S. Jetté-Charbonneau, R. Charbonneau, N. Lahoud, G. Mattiussi, and P. Berini, "Demonstration of Bragg gratings based on long ranging surface plasmon polariton waveguides," Opt. Express **13**, 4674–4682 (2005).

10. S. Jetté-Charbonneau, R. Charbonneau, N. Lahoud, G. A. Mattiussi, and P. Berini, "Bragg gratings based on long-range surface plasmon-polariton waveguides: comparison of theory and experiment," IEEE J. Quantum Electron. **41**, 1480–1491 (2005).

11. S. I. Bozhevolnyi, A. Boltasseva, T. Søndergaard, T. Nikolajsen, and K. Leosson, "Photonic bandgap structures for long-range surface plasmon polaritons," Opt. Commun. **250**, 328–333 (2005).

12. A. Boltasseva, S. I. Bozhevolnyi, T. Søndergaard, T. Nikolajsen, and K. Leosson, "Compact Z-add-drop wavelength filters for long-range surface plasmon polaritons," Opt. Express **13**, 4237–4243 (2005).

13. D. C. Zografopoulos and R. Beccherelli, "Liquid-crystal-tunable metal--insulator--metal plasmonic waveguides and Bragg resonators," J. Opt. **15**, 055009 (2013).

14. T. Christopoulos, G. Sinatkas, O. Tsilipakos, and E. E. Kriezis, "Bistable action with hybrid plasmonic Bragg-grating resonators," Opt. Quantum Electron. **48**, 128 (2016).

15. I. Epstein, I. Dolev, D. Bar-Lev, and A. Arie, "Plasmon-enhanced Bragg diffraction," Phys. Rev. B **86**, 205122 (2012).

16. I. Dolev, I. Epstein, and A. Arie, "Surface-plasmon holographic beam shaping," Phys. Rev. Lett. **109**, 203903 (2012).

17. X. Sun, X. Shu, and C. Chen, "Grating surface plasmon resonance sensor: angular sensitivity, metal oxidization effect of Al-based device in optimal structure," Appl. Opt. **54**, 1548–1554 (2015).

18. Y.-L. Ho, L.-C. Huang, E. Lebrasseur, Y. Mita, and J.-J. Delaunay, "Independent light-trapping cavity for ultra-sensitive plasmonic sensing," Appl. Phys. Lett. **105**, 061112 (2014).

19. N. I. Landy, S. Sajuyigbe, J. J. Mock, D. R. Smith, and W. J. Padilla, "Perfect metamaterial absorber," Phys. Rev. Lett. **100**, 207402 (2008).

20. K. Aydin, V. E. Ferry, R. M. Briggs, and H. A. Atwater, "Broadband polarization-independent resonant light absorption using ultrathin plasmonic super absorbers," Nat. Commun. **2**, 517 (2011).

21. G. Isić, B. Vasić, D. C. Zografopoulos, R. Beccherelli, and R. Gajić, "Electrically tunable critically coupled terahertz metamaterial absorber based on nematic liquid crystals," Phys. Rev. Appl. **3**, 064007 (2015).

22. D. C. Zografopoulos, G. Sinatkas, E. Lotfi, L. A. Shahada, M. A. Swillam, E. E. Kriezis, and R. Beccherelli, "Amplitude modulation in infrared metamaterial absorbers based on electro-optically tunable conducting oxides," Appl. Phys. A **124**, 105 (2018).

23. J. Hao, J. Wang, X. Liu, W. J. Padilla, L. Zhou, and M. Qiu, "High performance optical absorber based on a plasmonic metamaterial," Appl. Phys. Lett. **96**, 251104 (2010).

24. K. Bhattarai, S. Silva, K. Song, A. Urbas, S. J. Lee, Z. Ku, and J. Zhou, "Metamaterial Perfect Absorber Analyzed by a Meta-cavity Model Consisting of Multilayer Metasurfaces," Sci. Rep. **7**, 10569 (2017).

25. K. Bhattarai, Z. Ku, S. Silva, J. Jeon, J. O. Kim, S. J. Lee, A. Urbas, and J. Zhou, "A Large-Area, Mushroom-Capped Plasmonic Perfect Absorber: Refractive Index

Sensing and Fabry-Perot Cavity Mechanism," Adv. Opt. Mater. **3**, 1779–1786 (2015).

26. G. Kenanakis, C. P. Mavidis, E. Vasilaki, N. Katsarakis, M. Kafesaki, E. N. Economou, and C. M. Soukoulis, "Perfect absorbers based on metal--insulator--metal structures in the visible region: a simple approach for practical applications," Appl. Phys. A **123**, 77 (2017).

27. S. A. Tretyakov and S. I. Maslovski, "Thin absorbing structure for all incidence angles based on the use of a high-impedance surface," Microw. Opt. Technol. Lett. **38**, 175–178 (2003).

28. H. Wakatsuchi, S. Kim, J. J. Rushton, and D. F. Sievenpiper, "Circuit-based nonlinear metasurface absorbers for high power surface currents," Appl. Phys. Lett. **102**, 214103 (2013).

29. M. A. Kats and F. Capasso, "Optical absorbers based on strong interference in ultra-thin films," Laser Photonics Rev. **10**, 735–749 (2016).

30. A. N. Papadimopoulos, N. V Kantartzis, N. L. Tsitsas, and C. A. Valagiannopoulos, "Wide-angle absorption of visible light from simple bilayers," Appl. Opt. **56**, 9779–9786 (2017).

31. I. R. Hooper and J. R. Sambles, "Some considerations on the transmissivity of thin metal films," Opt. Express **16**, 17258–17267 (2008).

32. F. J. García-Vidal and L. Martín-Moreno, "Transmission and focusing of light in one-dimensional periodically nanostructured metals," Phys. Rev. B **66**, 155412 (2002).

33. Z. Tagay and C. Valagiannopoulos, "Highly selective transmission and absorption from metasurfaces of periodically corrugated cylindrical particles," Phys. Rev. B **98**, 115306 (2018).

Efficient and environmental-friendly perovskite solar cells via embedding plasmonic nanoparticles: an optical simulation study on realistic device architectures

GEORGE PERRAKIS,[*,1,2] GEORGE KAKAVELAKIS,[*,3,4] GEORGE KENANAKIS,[1] CONSTANTINOS PETRIDIS,[3,5] EMMANUEL STRATAKIS,[1] MARIA KAFESAKI,[1,2] AND EMMANUEL KYMAKIS[3]

[1]*Institute of Electronic Structure and Laser (IESL), Foundation for Research and Technology Hellas (FORTH), Heraklion, Greece*
[2]*Dept. of Materials Science and Technology, Univ. of Crete, Heraklion, Greece*
[3]*Department of Electrical & Computer Engineering, Hellenic Mediterranean University, Estavromenos, Heraklion, GR-71410, Crete, Greece*
[4]*Cambridge Graphene Centre, University of Cambridge, 9 JJ Thomson Avenue, Cambridge CB3 0FA, UK*
[5]*Department of Electronic Engineering, Hellenic Mediterranean University, Chania, GR-71305, Crete, Greece*
**E-mail: gperrakis@iesl.forth.gr*
**E-mail: gk415@cam.ac.uk*

Abstract: Solution-processed, lead halide-based perovskite solar cells have recently overcome important challenges, offering low-cost and high solar power conversion efficiencies. However, they still undergo unoptimized light collection due mainly to the thin (~350 nm) polycrystalline absorber layers. Moreover, their high toxicity (due to the presence of lead in perovskite crystalline structures) makes it necessary that the thickness of the absorber layers to be further reduced. Here we address these issues via embedding spherical plasmonic nanoparticles of various sizes, composition, concentrations, and vertical positions, in realistic halide-based perovskite solar cells. We theoretically show that plasmon-enhanced near-field effects and scattering leads to a device photocurrent enhancement up to ~7.3% when silver spheres are embedded inside the perovskite layer. An even further enhancement, up to ~12%, is achieved with the combination of silver spheres in perovskite and aluminum spheres inside the hole transporting layer (PEDOT:PSS). The proper involvement of nanoparticles allows the employment of much thinner perovskite layers (up to 150 nm) reducing thus significantly the toxicity. Providing the requirements related to the design parameters of nanoparticles, our study establishes guidelines for a future development of highly-efficient, environmentally friendly and low-cost plasmonic perovskite solar cells.

8. Introduction

Emerging halide Perovskite ($CH_3NH_3PbX_3$, X= Cl, Br and I) based thin-film Solar Cells (PSCs) have attracted significant interest over the recent years due to their remarkable photovoltaic performance (incident solar to electrical power conversion efficiency of 23.7%). Some of their main characteristics are the high absorption coefficient of perovskite along with its direct band-gap property [1] and, high power conversion efficiency [2, 3] (PCE) combined with fabrication simplicity using solution-processing techniques at room temperature [4, 5]. However, despite their high performance, there are still two major issues that must be addressed. Firstly, a further improvement of the light collection of the PSCs should be achieved [6, 7]. Additionally, a reduction of the PSCs' toxicity [8], due to the presence of pure lead (Pb) in the perovskite materials, should be attained for their further commercialization.

A possible solution to reduce the amount of the lead is to employ perovskite absorbers thinner than the optimum thickness [9] of about ~350 nm. However, there is a main drawback using this approach, which is the small interaction time of the incoming wave with the very thin perovskite layer, resulting to an unoptimized light collection and thus a reduced absorption.

One of the most promising approaches to increase the light/matter interaction time and as a result to improve light collection in thin-film solar cells is the use of the plasmonic effect [10]. Surface plasmons are collective oscillations of conduction electrons of metallic nanoparticles that are excited by light at the nanoparticle interface with the surrounding dielectric medium. Important features of the surface plasmons are that they are associated with high local-field amplitudes and strong far-field scattering at the resonances of the oscillations. Strong far-field scattering can increase the absorption efficiency in thin film solar cells also by exploiting the effect of total internal reflection. This has been already demonstrated in amorphous-silicon-based thin-film solar cells [11] and in organic solar cells [12]. Moreover, the high local fields in the vicinity of plasmonic nanoparticles overlap not only with metal but also with the surrounding absorbing matter resulting in increased absorption, *A*. This follows directly from Poynting's theorem for power dissipation [13] [$A \sim |\boldsymbol{E}|^2$]. To benefit from the above features, the parameters determining the resonance characteristics of the plasmonic nanoparticles, i.e. the size, position or the material of the nanoparticles and their hosting environment [14], must be carefully chosen to properly match the plasmon resonance to the spectral properties of the solar cell's material. Otherwise, ohmic losses or coupling between the nanoparticles [15] can lead to increased parasitic absorption in metal turning into heat, a behavior not desirable in solar cells.

Other routes to enhance perovskite solar cell efficiencies have recently proposed in the literature. One prominent example is light focusing structures, such as microlens arrays attached to the top (glass) side of the solar cell [16]. Their main characteristic was the nanoscale light focusing from the microlens within the absorber layer by the formation of vertical standing waves that resulted to enhanced absorption. Another prominent example is inverted vertical-cone photonic-crystal PSC architectures that trap incident sunlight due to parallel-to-interface refraction into slow-light modes over a broad angular range from 0 to 70 degree for both TE and TM linear polarizations [17]. These cases provided significant absorption enhancement even up to 6% compared to the Lambertian limit; however, they require elaborate designs and future commercialization depends on the simplicity of the cell processing.

Already, several studies have explored the plasmonic enhancement in perovskite thin-films [18, 19]. An additional reason for this is that metal particles dispersed inside a solution preserve the simplicity of the PSC at processing without increasing its cost [20]. In fact, the cost reduction caused by thickness reduction is greater than that caused by incorporating metal particles. The main finding of the existing studies was that metal particles could improve considerably the beneficial absorption inside the perovskite material [21]. Interestingly, parasitic absorption in metal particles does not surpass the enhancement they provide. More specifically, both N.K. Pathak et al. [22] and Roopak et al. [23] explored Mie theory [24] and showed that silver, gold and aluminum nanoparticles, embedded inside a perovskite matrix, support plasmonic resonances of high magnitude with tunable resonance frequency and width by varying the size, shape or material of the nanoparticles. These results are very promising since plasmonic nanoparticles can induce light incoupling to the perovskite near its band edge (~650-800 nm) where it shows inferior photo response due to lower absorption in conjunction with increased reflection from the perovskite at that regime [6, 7]. In this respect, broadband absorption enhancement (>600 nm) was reported in PSCs that incorporated plasmonic gold-silver alloy popcorn-shaped nanoparticles especially around the band-edge, between 720-820 nm. Since the excitation of plasmonic resonances is closely related to the shapes and composition of the metal materials, irregular alloy nanoparticles with many fine structures are conducive to support panchromatic plasmonic resonances [18]. Moreover, Carretero-Palacios

S. et al. [25, 26] theoretically examined the effect of plasmonic enhancement by incorporating metallic nanoparticles of different shapes, sizes, concentrations and composition in methyl ammonium lead iodide perovskite ($CH_3NH_3PbI_3$) absorbing layers assumed to be supported on a glass substrate and coated by a hole transporting material. Notably, it was shown that the conditions for plasmonic enhancement are not very stringent, and ample ranges of sizes, shapes and concentrations of the metallic nanoparticles give rise to an important degree of improvement. In addition, the main conclusion was that the improvement was neatly the result of the near optical field enhancement at longer wavelengths within the absorption band of perovskites (~550-800 nm).

The above-mentioned studies demonstrate the possibility of improvement of perovskite film absorption with the employment of metallic nanoparticles; it is still of great importance, though, if they can be successfully implemented to realistic PSCs. In a real solar cell one has to consider the interplay of metal particles with several optical mechanisms; for instance the effect of the asymmetric environment of the PSC on the localized surface plasmon resonances of the nanoparticles compared to a homogeneous perovskite matrix, coupling with fabry-perrot (FP) resonances (i.e. modes that are supported by the absorbing layer due to its finite thickness) and guided modes of the absorbing layer, interference effects and reflections introduced by the multilayered structure of the PSC, etc., which give rise to a more complex optical system in the neighborhood of the nanoparticles. All those effects are highly unexplored and need careful examination as to definitively conclude on the impact of plasmonic nanoparticles on the performance of realistic PSCs and to be able to optimize this impact.

In this respect we aim in this paper to clarify the effect of the plasmonic nanoparticles on the absorption properties and enhancement of realistic PSCs, with further aim to improve the optical performance of such PSCs. We achieve this by incorporating metal nanoparticles of different size, concentration and material (among the most standard ones, namely silver, gold and aluminum) at different positions into the perovskite absorber or inside different layers of the PSC (see Fig. 1). Moreover, the combined effect of nanoparticles embedded inside different layers at the same time is examined. The aim is to (i) achieve an enhanced absorption efficiency compared to the conventional (nanoparticles-free) PSCs and (ii) reduce the amount of lead by either replacing perovskite material by nanoparticles or by employing thinner perovskite absorbers, without deteriorating the absorption. The perovskite material that we deal with in this work is the most common halide perovskite, the methyl ammonium lead iodide perovskite ($CH_3NH_3PbI_3$), which has been extensively examined for solar cells. One of its main advantages is the fabrication simplicity, while its direct band-gap of ~1.55 eV (~800 nm, i.e. at the onset of the optical range), very close to the ideal compared to other perovskites in which another halide is present, leads to high efficiencies. Improving further its already good performance without increasing the fabrication cost is of high importance.

9. PSC geometrical and material parameters - Modeling approaches

Here we investigate the common inverted [27] planar heterojunction PSC geometry (see Fig. 1) where the poly(3,4-ethylenedioxythiophene) polystyrene sulfonate (PEDOT:PSS) and the phenyl-C71 -butyric acid methyl ester (PCBM) serve as the hole transporting layer (HTL) and the electron transporting layer (ETL) respectively. The planar inverted (upside down fabrication, possibly on top of flexible substrates [27]) PSC adopts the structure of organic solar cells to fulfill the requirements of high performance as well as low-cost and easy fabrication, where all the device layers could be deposited at room temperature through a solution-process [4]. Additionally, since the most efficient two-terminal monolithic Si/Perovskite tandem solar cells are based on inverted heterojunction device architectures, their fine optimization towards the beyond 30% efficiency target is of significant importance. The structure of the device investigated here is as follows: SiO_2 (1.1 mm) /ITO (100 nm) /PEDOT:PSS (40 nm) /$CH_3NH_3PbI_3$ /PCBM (50 nm) /Al (100 nm) (see Fig. 1), where the

numbers indicate the thickness of each layer. The transparent conducting oxide (ITO: indium tin oxide) and the aluminum back-reflector serve as the electrical contacts.

In our study the thickness of the perovskite absorber is varied among the standard lengths of PSCs, regarding efficient absorption and photocarrier collection [9], from 150 nm to 400 nm. We note that the optimized perovskite thickness in PSCs is in the range of 280 to 350 nm [28, 29]. Larger perovskite thicknesses suffer from long transport distance, which inevitably intensifies adverse recombination, while smaller thicknesses are difficult to demonstrate experimentally due to challenges involved with device fabrication and degradation in electrical properties. However, devices with perovskite thicknesses of ~200 nm have been realized [28] and, as mentioned above, their inadequate light absorption could be sufficiently enhanced.

To simulate the performance of our structures the material parameters used for the perovskite [see inset of Fig. 2(b)] and the materials of the other layers have been obtained from Ref. [4], while those of silver, gold and aluminum from Palik [30]. Despite the "inverted" fabrication sequence of the PSC layers, we will refer as top layers the layers at which the sun is incident on, i.e., following this order from the top to bottom: Glass/ITO/PEDOT:PSS/Perovskite/PCBM/Al.

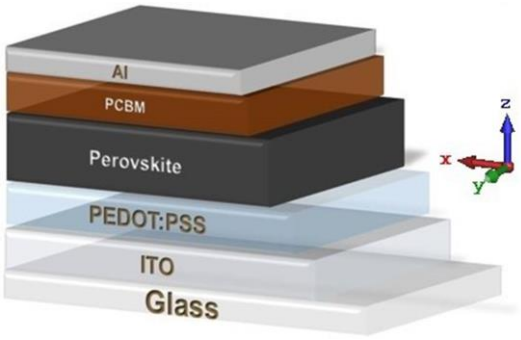

Fig. 1. Geometry of the inverted planar heterojunction perovskite solar cell. The thickness and role of the different layers of the cell are discussed in the main text.

Due to the complexity of the solar cell geometries investigated here, which include metallic nanoparticles and highly absorbing multilayered materials, a numerical methodology is required. To evaluate the optical performance of the plasmonic PSCs, we performed three-dimensional full-wave electromagnetic simulations using the commercially available software CST Microwave Studio (Computer Simulation Technology GmbH, Darmstadt, Germany) based on the finite element method. Briefly, we assess the optical response of the system by illuminating the structure with a plane wave source at two perpendicular linear polarizations, TE and TM. The simulated structure consists of a semi-infinite SiO_2 (glass) slab, which serves as a substrate for the device fabrication, on top of the multilayered PSC. The simulated region is terminated by unit cell (Floquet) boundary conditions at the bounded planes perpendicular to the surface of the PSC, to investigate the effect of the periodically placed nanoparticles, and by open-boundary (matching) conditions realized by Floquet modes at the unbounded planes parallel to the PSCs' surfaces. Finally, in order to obtain the angular performance, broadband simulations were also performed for each angle of incidence varying from 0 to 70 degrees with a step of 10 degrees.

Finally, we quantify the optical performance of the device with and without the metallic nanoparticles by obtaining numerically the absorption in the perovskite material from which we determine the generated current density inside the solar cell, called the illumination or photocurrent density (J_{ph}), given by:

$$J_{ph} = q \int A_p(\lambda) \Phi_{AM1.5G}(\lambda) d\lambda, \quad (1)$$

In Eq. (1) $\Phi_{AM1.5G}$ is the photon flux density [in photons·m^{-2}·s^{-1}·nm^{-1}] of the "AM 1.5G" standard sunlight spectrum [31] reaching the Earth's surface, that is considered universal when characterizing solar cells, and A_p, q are the absorption of the perovskite material and the elementary charge [in C] of an electron respectively. The integration takes place at $300<\lambda<800$ nm that corresponds to the range within the pass-band edges of the perovskite material. Throughout this work, J_{ph} is considered the most critical parameter for the performance evaluation of the PSCs. Increasing J_{ph} leads to an increased current density under short circuit conditions (J_{SC}) and hence increased extracted electrical power and efficiency, as long as the approach chosen for the J_{ph} enhancement does not have a negative influence on the electrical properties of the device.

In fact, the incorporation of metal nanoparticles in PSCs has been shown that not only is not negative but under certain conditions it can act in favor of the electrical properties of the cell. For instance, as concluded in Ref. [32], the incorporation of metal nanoparticles may preserve or even enhance the diode characteristics of the PSC, like the open-circuit voltage or the fill factor, due to improved transport and collection of charge carriers, as long as a more careful design implementation is applied. Moreover, in plasmonic PSCs larger than the expected photocurrent enhancement was found with the incorporation of core-shell ($Au@SiO_2$) nanoparticles [19]. However, in our study, to ensure that the involvement of nanoparticles will have the smallest possible impact on the electrical properties of the cell, we choose carefully the size and concentration of the nanoparticles when placed close to the carrier transporting layers where an energy barrier for the transportation of the photo-generated carriers can be formed; moreover, the effect of coating layers on the surface of metal nanoparticles, which can cause electrical isolation at metal-semiconductor junctions, is also examined and evaluated.

10. Results and discussion

In the current section we discuss the effect on the PSC photocurrent density (J_{ph}) of plasmonic nanoparticles of spherical shape and of different sizes, concentrations, positions and materials, embedded in different parts of the PSC, for the cell shown in Fig. 1. To gain insight on the mechanisms that lead to the unexploited absorption losses, which decline the absorption efficiency of the solar cell, and to employ a common reference system we investigate and discuss first the pristine PSC, i.e., the cell with no metallic nanoparticles (see subsection 3.1). Next, we discuss the effect of plasmonic spheres inside the perovskite layer of the PSC (subsection 3.2) and demonstrate and analyze the associated increase of photocurrent density. In subsection 3.3 we examine the effect of plasmonic nanoparticles (not only spherical but also cylindrical ones) if placed inside the carrier transporting layers and not in the perovskite layer. This way there is no competition between the volume occupied by the metal particles and the perovskite material. Finally, in subsection 3.4 the combination of nanoparticles placed simultaneously inside more than one layers of the PSC is examined, to demonstrate the full potential of plasmonic nanoparticles if combined with realistic PSCs.

10.1 Pristine PSC

To fully understand the PSC optical response and set appropriate references, we firstly calculate the absorption for each layer of the pristine PSC for a device as shown in Fig. 1 with perovskite layer thickness equal to 350 nm. The result is shown in Fig. 2(a). As can be seen, absorption in perovskite remains high along the entire optical spectrum, due to its high absorption coefficient [see inset in Fig. 2(b)]. Interestingly, high absorption in perovskite persists even at longer wavelengths (~750 nm), close to its band-gap edge (~750-800 nm), as a result of its direct band-gap property. The absorption peak at λ~610 nm is a FP mode arising from the finite thickness of the perovskite slab while the second absorption peak, at λ~750 nm, is a FP mode induced by the aluminum back reflector. Specifically, perovskite absorbs 75% of the maximum achievable current density ($J_{ph,sun}$, obtained from Eq. (1) with A_p=1,

integrated at 300<λ<800 nm), while all the other materials of the device absorb 8% (absorption in PCBM is almost zero along the entire spectrum). The highest fraction of the unexploited sun spectrum is lost due to reflection and equals 17%.

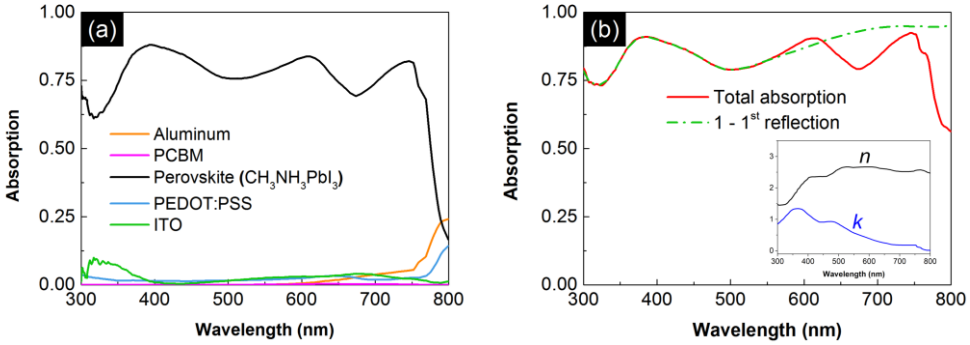

Fig. 2. (a) Absorption in each layer of the PSC. (b) Total absorption (red solid line) of the PSC, absorption in perovskite due to the first reflection only (green dashed-dotted line). Inset: refractive index (black line), *n*, and absorption coefficient (blue line), *k*, of perovskite $CH_3NH_3PBI_3$.

To reveal the origin of the reflection losses we calculated both the total absorption (perovskite absorption and the parasitic absorption that occurs at the several layers of the device) of the pristine PSC and the absorption ($A_{1st} = 1 - R_{1st}$) arising from the "first" reflection (R_{1st}) of the top layers of the structure. More specifically, R_{1st} is calculated for the PSC shown in Fig. 1 but assuming a semi-infinite perovskite layer along the *z*-axis without the back-aluminum reflector and the PCBM layer. This way, the "first" reflection from the top layers can be computationally isolated from the total reflection of the device since waves that are not absorbed and reach the bottom surface of the structure are lost. The result is shown in Fig. 2(b), together with the refractive index and absorption coefficient of the perovskite (see inset – data from Ref. [4]). The red line corresponds to the total absorption (both perovskite absorption and the parasitic absorption that occurs at the several layers of the device) of the pristine PSC (as shown in Fig. 1), which is subject to both multi-pass phenomena and interference effects arising by the multilayer device, and the green line corresponds to the absorption ($A_{1st} = 1 - R_{1st}$) arising from the "first" reflection. As can be seen there, the absorption spectrum of the system is divided into two spectral regimes of different behavior. For λ<550 nm, the total absorption of the pristine PSC follows the absorption arising from the "first" reflection (i.e. it occurs in the first pass of the wave into the perovskite) due to the very high absorption coefficient of the perovskite material for the corresponding wavelengths [see inset in Fig. 2(b)]. For λ>550 nm, where the absorption coefficient of the perovskite material is much lower, interference effects introduced by the several layers of the device of finite thickness are now present, leading to an overall reduced absorption due to higher reflection losses relative to the "first" reflection. These results confirm that further improvement of the PSC could be achieved in agreement with other studies [6, 7], at the range of ~650-800 nm where perovskite material shows inferior absorption that results to higher reflection losses from the PSC, as well as at the range of ~350-650 nm by minimizing further the reflection at the PEDOT:PSS-Perovskite interface. Such an improvement can be achieved by adoption of efficient light trapping strategies, which will forbid light from escaping. As we show in this article such a strategy is the proper incorporation of metallic nanoparticles.

Before proceeding to the incorporation of the nanoparticles we evaluate our pristine PSC calculations by comparing with experimental data for the same device [20]. The J_{ph} of our simulated pristine device was calculated at 20.40 mA/cm^2, very close to the experimentally obtained current density under short circuit conditions (J_{SC}), equal to 20.55 mA/cm^2. This indicates that the experimental device achieves near-unity quantum yield for the generation

and collection of charge carriers [33]. In addition, any mismatch between the simulated sunlight and the AM1.5G standard is negligibly small. The excellent agreement of our theoretical calculations with the experimental measurements allows us to continue with the examination of the plasmonic PSCs while using the J_{ph} of the pristine PSC as a reference.

10.2 Plasmonic nanoparticles inside perovskite

In what follows, we aim to investigate and clarify the effect of plasmonic nanoparticles on the optical response of the PSC for different nanoparticle parameters and configurations. This will allow an efficient understanding and optimization of the PSC performance. In particular, we examine the effect of metal spheres embedded inside the perovskite layer for different metal-material (subsection 3.2.1), sphere size and vertical position (along *z*-axis, see Fig 1) (subsection 3.2.2), and sphere lateral-spacing/concentration (subsection 3.2.3), including investigation of features which are likely to be present in a dispersion of metal particles in a realistic PSC, i.e., random particles location and clustering, and other aspects like lattice effects (subsection 3.2.3). Finally, in subsection 3.2.4 the consequences of shielding metal particles with a dielectric coating or covering with organic ligands, an approach commonly employed in realistic systems, are also assessed. In all those studies we assume a constant perovskite layer thickness of 350 nm that is considered optimum regarding the PCE of the PSCs [9]. The spherical shape of nanoparticles was preferred when they are embedded inside the perovskite layer because it is associated with: (i) broadband extinction (scattering and absorption) cross-sections of high magnitude, according to Mie theory [22], for an ample range of diameters, along the entire spectral region near perovskite's band edge (~650-800 nm) where it shows inferior photoresponse; (ii) significant field intensity enhancement in the vicinity of the nanoparticle [23]; (iii) preservation of the PSC fabrication simplicity due to its symmetric nature [34].

3.2.1 PSCs efficiency versus nanoparticle material

Optimization of plasmonic light trapping in solar cells is a balancing act in which several physical parameters and competing factors must be taken into account. For instance, regarding nanoparticle size, very small particles suffer from significant ohmic losses according to Mie theory [24] whereas larger particles, while show larger scattering and smaller ohmic losses, come at the expense of the useful host material (if their spacing is kept constant). Regarding nanoparticle spacing, smaller spacing, associated with larger nanoparticle coupling, may favor absorption (as it may create collective modes propagating in the perovskite), but again comes at the expense of the active perovskite material (if particle size is kept constant). Moreover, one has to take in to account the coupling of nanoparticles with the guided modes supported by the perovskite layer of finite thickness and with the FP resonances induced by the multilayer structure. Thus, the question of optimum size and spacing as to achieve higher nanoparticle-induced PSCs efficiency does not have a trivial answer. Although the above issues will be discussed in more detail in the next sections, while here the aim is to investigate the effect of the nanoparticle metal/composition, it is of great benefit to start our investigation from a nearly optimized size and periodicity setup. For that we performed a "blind" optimization (using the global optimizer of the CST software, employing the "Particle Swarm Optimization" algorithm), requiring maximum photocurrent density enhancement for the plasmonic PSC relative to the pristine PSC (reference system), i.e. maximum $\eta(\%) = ((J_{ph,plasm}-J_{ph,ref})/J_{ph,ref})\cdot 100$, for spheres of three different metals, namely silver, gold and aluminum. The spheres were forming a square lattice and were located exactly at the middle of the perovskite layer along *z*-direction (see inset of Fig. 2b). In the optimization the enhancement η was calculated for radius, r, varying from zero to 90 nm and lateral spacing, L (in the *x*-*y*-plane), varying from 200 nm to 500 nm. The optimization regarding silver and gold spheres gave larger enhancement, η, for r=40 nm, while for aluminum for r=60 nm. The optimum lateral spacing was in all cases L~300 nm.

To elucidate the origin of the enhancement and of the above-mentioned optimum parameters, we calculated and plot in Fig. 3(a) the scattering and absorption cross-section for a single silver, gold and aluminum sphere, embedded in perovskite matrix (considering here zero absorption in perovskite). As can be seen in Fig. 3(a), in the region 700-800 nm, where the perovskite shows inferior absorption, the silver and gold spheres (especially silver) present much larger scattering compared to aluminum, indicating their favorable role as plasmonic scatters in plasmonic PSCs. Indeed, this is confirmed by relevant simulations, as those presented in Fig. 3(b).

Fig. 3(b) illustrates the absorption inside the perovskite for plasmonic PSCs that contain silver, gold and aluminum spherical particles located exactly at the middle of the perovskite layer with the size and periodicity for which the photocurrent density was found maximum. As can be concluded from Fig. 3(b), the highest absorption and thus photocurrent enhancement is obtained for silver nanoparticles. Moreover, the absorption enhancement for the case of silver and gold nanoparticles takes place at a wider spectral range compared to aluminum and coincides with the 2nd spectral region (λ>550 nm) mentioned in section 3.1, where the absorption coefficient of the perovskite is lower.

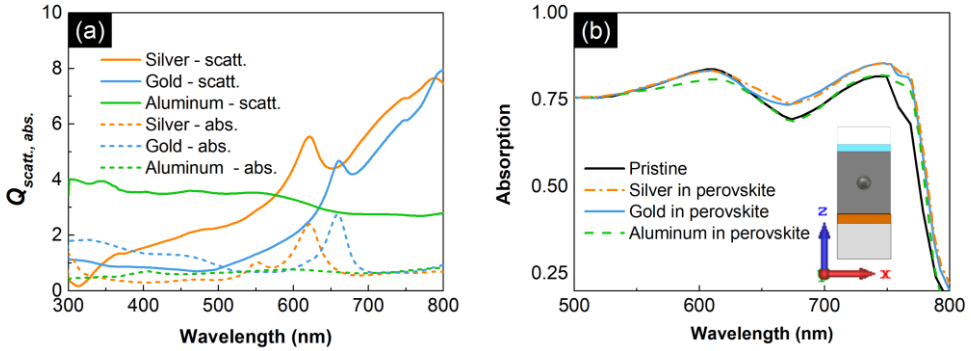

Fig. 3. (a) Scattering (solid lines) and absorption (dashed lines) cross-sections ($Q_{scatt.,\ abs}$) of a silver sphere (orange line – sphere radius 40 nm), gold sphere (blue line- sphere radius 40 nm) and aluminum sphere (green line - sphere radius 60 nm) inside a homogeneous perovskite matrix (here the matrix is considered with no losses and the absorption cross-section represents only ohmic losses inside the spheres); (b) Absorption in perovskite for plasmonic PSCs with silver (orange dashed-dotted line), gold (blue line) and aluminum (green dashed line) spheres placed at the middle of the perovskite layer (see inset) compared to the pristine case (black line). The radii of spheres are as in (a), and they are placed in square lattice with spacing L=300 nm.

In all cases, the origin of the absorption enhancement was that the plasmonic nanoparticles behaved as light nano-antennas that led to strong scattering (thus to increase of the interaction time of the field with the perovskite material) and to strong local fields (common to plasmonic antennas) in their vicinity, inside the absorptive perovskite layer. These strong local fields are demonstrated in Fig. 4, where the normalized distribution of the squared amplitude of the electric field, $|\boldsymbol{E}|^2/|\boldsymbol{E}_0|^2$, is plotted for an incident plane wave of λ=779 nm, at which the maximum absorption enhancement takes place ($\boldsymbol{E}_0$ is the incident electric field). Fig. 4 demonstrates the higher local fields around the sphere for the case of silver and gold nanoparticles compared to the aluminum case. Both high local and scattered fields make the silver nanoparticles the optimum plasmonic material choice for the solar cell absorption enhancement, justifying their corresponding larger enhancement factor [obtained from the data of Fig. 3(b)], which is 3.36%, compared to 2.80% for gold and 0.25% for aluminium.

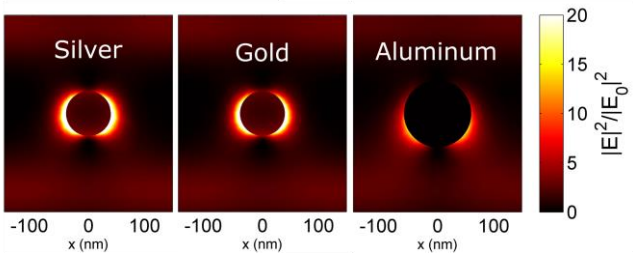

Fig. 4. Normalized (relative to the incident field, E_0) distribution of the squared amplitude of the electric field, at λ=779 nm for silver, gold and aluminum (left, central, right figures respectively) spheres with optimum radius and periodicity for each case.

3.2.2 Vertical position and nanoparticle size effect on the PSCs performance

Another important parameter affecting the optical response of the PSC is the depth at which the nanoparticles are embedded inside the perovskite layer. In a homogeneous perovskite absorbing matrix the effect of nanoparticles' vertical position is related basically to the absorption depth of the wave into the perovskite [25]. For a more complex environment like in PSCs, the effect of nanoparticles' position is not so straightforward and further analysis is needed, given also the fact that in a realistic solar cell device the vertical distribution of nanoparticles is difficult to control. Therefore, in this section, we vary the vertical position (along the *z*-axis; see Fig. 1) of silver spheres placed in a square lattice in the *x*-*y* plane with spacing L=300 nm (spacing for which we have found maximum solar absorption enhancement - see subsection 3.2.1), for two radii; a smaller one, of 40 nm, and a larger, of 70 nm, to take as well into consideration the size effect as the vertical position of nanoparticles varies. Fig. 5(a) shows the enhancement factor η (%) as a function of particles' position along the *z*-direction for r=40 nm (blue line) and r=70 nm (orange line), where Z denotes the distance of the center of the metallic nanoparticle from the top perovskite surface. Fig 5(b) shows the associated absorption spectrum for the case of r=40 nm for vertical distances Z_1=70 nm, Z_2=175 nm (exactly at the middle of the perovskite layer), Z_3=245 nm, Z_4=270 nm (see right panel in Fig. 5), compared to the case with r=70 nm and Z=Z_5=100 nm, and with the pristine PSC.

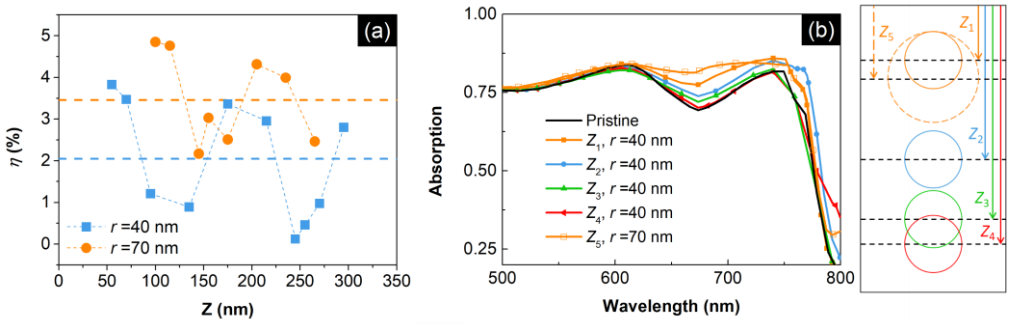

Fig. 5. (a) η (%) as a function of Z which denotes the distance of the center of the metallic nanoparticle from the top perovskite surface, for a periodic (in the *x*-*y* plane) system of silver spheres with radius r=40 (blue line) and 70 nm (orange line), and periodicity 300 nm. Dashed lines indicate the averaged η (%) for all positions for each case. (b) Absorption of perovskite for the plasmonic PSC with silver spheres of r=40 nm placed at different vertical positions (Z_1=70 nm – orange line, Z_2=175 nm – blue line, Z_3=245 nm – green line, Z_4=270 nm – red line) inside the perovskite layer, as depicted at the right panel, compared to the case with silver spheres of r=70 nm at Z_5=100 nm (orange dashed line) and the pristine case (black line).

As can be seen, the optimum vertical position is close to the top surface of the perovskite, while the decrease of absorption efficiency going from top to bottoms is not monotonic. In addition, silver spheres of higher radius (r=70 nm) provide higher absorption in most of the vertical positions, and thus higher average η (%) [see dashed lines in Fig. 5(a)].

To reveal the origin of this puzzling non-monotonic behavior as we change the vertical position of the metal nanoparticles inside the perovskite layer, we examined the electric field intensity, $|\boldsymbol{E}|^2/|\boldsymbol{E}_0|^2$, for the r=40 nm case and the vertical positions shown in Fig. 5(b), including the case of the pristine PSC. This intensity for λ=673 nm, where a substantial absorption enhancement is observed, is plotted in Fig. 6.

For the case without nanoparticles, shown in Fig. 6(a), we see that the electric field forms a standing wave inside the perovskite layer which arises from the fabry-perrot resonance induced by the aluminum back reflector of the device. Analyzing the plots shown in Fig. 6, we see that we have larger enhancement in the cases where the vertical nanoparticle position coincides with field maxima of the standing wave, and minimum or no enhancement where the sphere position is in the nodes of the electric field. This is easy to understand taking into account that both the local field around the nanoparticles and the scattered field (main factors of the absorption enhancement) are directly proportional to the input field. Thus, nanoparticles at the field maxima experience the largest possible input field associated with the largest resulting local and scattered fields.

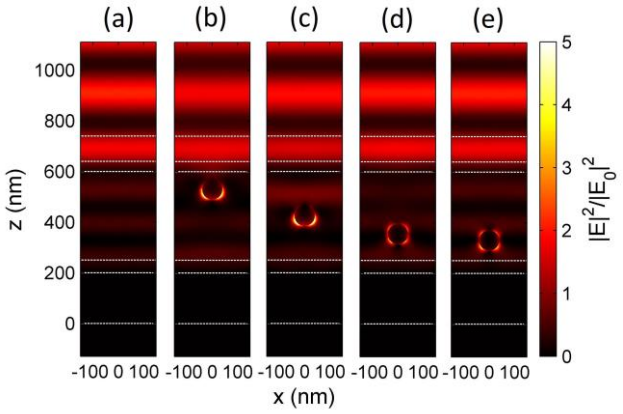

Fig. 6. Normalized distribution of the squared amplitude of the electric field, $|\boldsymbol{E}|^2/|\boldsymbol{E}_0|^2$, at λ=673nm, for the pristine PSC (a), and for a PSC with spherical silver nanoparticles placed at the four different vertical positions shown in Fig. 5, i.e. at Z_1 (b), Z_2 (c), Z_3 (d), and at Z_4 (e). In all cases the nanoparticles radius is 40 nm and their lateral spacing 300 nm. $\boldsymbol{E}_0$ is the incident electric field.

We noticed the same vertical position dependence when spheres of larger size, i.e., with a radius equal to 70 nm, are placed inside the perovskite layer. Moreover, since larger spheres are associated with smaller ohmic losses and larger scattered and near-field enhancement (as they exploit also the quadrupole besides dipole mode), they seem to be more robust regarding their performance associated to their vertical position [see Fig 5(a)]. Therefore, r~60-70 nm seem to be the optimum sphere size for PSC absorption enhancement.

Interestingly, as observed in Fig. 5(a), the largest absorption enhancement for both the r=40 nm and r=70 nm cases is observed when the spheres are placed close to the top surface of the perovskite. The basic reason is that spheres close to the top of the perovskite behave also as antireflection layer, directing the scattered light towards perovskite. Close to the top of the perovskite, the larger scattering offered by the larger size particles seems to lead to larger enhancement [see Fig. 5(b)]. We note though that if placing large metal spheres at the top positions in perovskite, close to the interface with PEDOT:PSS, there is the risk of increasing the interface transport resistance, and therefore a coating layer causing electrical

isolation may be needed [35]. The presence and optical response of such a layer is discussed in subsection 3.2.4.

3.2.3 Nanoparticles concentration effect on the PSC performance

In the current section we aim to elucidate the effect of the concentration of metal particles at the expense of the perovskite material. Concentration is considered a critical parameter in plasmonic solar cells since it is a parameter that can be easily controlled externally at processing, while, e.g. the precise control of position is not possible, resulting in a more randomized environment. To predict the effect of the concentration on the solar cell performance and to optimize it, it is not a straightforward task, as this effect is not expected to be monotonic. Small concentrations are expected to give small plasmonic impact while larger concentrations come at the expense of the highly absorbing perovskite material. Here we omit the case of very-closely spaced nanoparticles which requires removal of much of the active perovskite material.

In our numerical study, we change the nanoparticles concentration by changing the lattice constant, i.e., the interparticle distance, maintaining a constant sphere radius (r=70 nm) and vertical position (Z_5 position – see Fig. 5), values/conditions which were found as optimum according to the analysis of our previous sections. The results are shown in Fig. 7, where we plot the absorption versus wavelength for different lattice constants [Fig. 7(a)] and the resulting photocurrent density [Fig. 7(b)].

As was expected and mentioned above, the effect of concentration on the photocurrent density is not monotonic. Here lattice constants around 300 nm seem to give the optimum performance, while both smaller and larger lattice constants lead to a decline of the achieved photocurrent. This is not unexpected, as mentioned also above, as small concentrations are equivalent to small impact of the plasmonic particles, while larger concentrations are associated also with interparticle coupling and the possible formation of collective modes in the perovskite, which facilitate absorption. Since though the enhancement of concentration goes in conjunction with decrease of the active perovskite material, the effect of the plasmonic enhancement is expected to be overwhelmed above a critical concentration.

The achievement of optimum performance in our case for L=300 nm, where on one hand no very strong interparticle coupling is expected (due to the relatively large interparticle distance) and on the other hand it is still subwavelength compared to the region of 650-750 nm where the plasmonic enhancement has considerable impact, indicates that the effects of deviations from the periodicity of the particles system are expected to be relatively small. This is indeed verified by additional simulations, where we introduced deviations from the periodicity (changing the lateral spheres position) in the system of Fig. 7(a), preserving the concentration of the L=300 nm periodic case; we found a relatively small decrease of the efficiency compared to the periodic case [see green rhombus in Fig. 7(b)]. As was already mentioned examination of non-periodic systems is particularly important in our case, since in realistic solar cells the precise control of the position of nanoparticles is not possible at processing, resulting to a rather random plasmonic system.

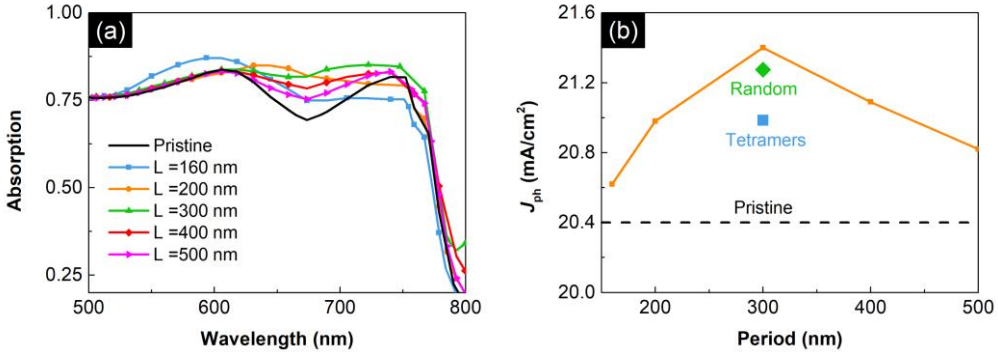

Fig. 7. (a) Absorption of perovskite versus wavelength for different lattice constants (160 nm – blue line; 200 nm – orange line; 300 nm – green line; 400 nm – red line; and 500 nm – magenta line) compared to the pristine case (black line) and (b) the resulting photocurrent density for the different concentrations investigated, assuming silver spheres with a constant radius of 70 nm, and vertical position Z_5 as shown in Fig. 5. The simulations to examine randomness were conducted assuming a periodicity of L=2×300=600 nm (along x-, and y-axis), due to the optimum L=300 nm case of the square lattice, keeping this way the same concentration. Random deviations to the particles lateral position were induced (their spacing in the lateral direction varies randomly thus it is not equal to 300 nm) two times, showing here the results of their average. The result is depicted as the green rhombus. The simulations to examine clustering were conducted assuming again a periodicity of L=2×300=600 nm (along *x*-, and *y*-axis), assuming four spheres per unit cell (without altering this way the particles concentration), where we decreased gradually their inter-particle distance going from particles to particle tetramers. The result is depicted as the blue square.

Attempting to be as close as possible to the experimentally realizable plasmonic PCSs, in our simulation study we examined also other features which are likely to be present in a dispersion of metal particles in such PSCs, like the effect of clustering. (Although we aim for the precise control of the concentration of nanoparticles inside the perovskite layer, clustering formation during the actual preparation of the films cannot be entirely discarded.) Therefore, we performed simulations assuming a periodicity of L=2×300=600 nm (along *x*-, and *y*-axis) with four spheres per unit cell, without altering this way the particles concentration, where we decreased gradually their inter-particle distance going from equally spaced particles to particle tetramers. The impact of clustering for silver spheres of r=70 nm at Z_5 (see Fig. 5) is depicted as the blue square in Fig. 7.

Examining additional concentrations besides the optimum one, we see that although the formation of clustering in general results to a decrease of the solar cell efficiency its effect is not capable to override the plasmonic enhancement. Corresponding field plots showed that the hot spots created inside the inter-particle gap occupy a very small volume that the effect on the perovskite absorption is much less significant than that when particles are separated. However, this balance is better in the case of larger spheres due to the higher scattering, especially when placed close to the top perovskite surface, due to their antireflection property at that position, leading to substantial enhancements even if clustering is present.

3.2.4 Coatings and organic ligands effect on PSCs performance

The preparation of metal (silver, gold, aluminum) nanoparticle dispersions in most fabrication techniques gives nanoparticles covered with ligands (PVP, CTAB, PEG Hexadecylamine) (although there are techniques giving bare nanoparticles, e.g. ultrashort pulsed laser ablation [20]). Moreover, the nanoparticles often are prepared on purpose with dielectric coatings [19, 35], e.g. silica, to prevent the direct contact of metal with semiconductor and avoid recombination of the excited charges at the metal/ semiconductor interface. Therefore, it is important to consider also the optical effect of dielectric nanoparticle covering, given the fact

that a large part of the plasmon-induced absorption enhancement occurs in the close vicinity of the nanoparticles, i.e. in the area occupied by the coating.

Since, the refractive index of most common organic ligands is almost the same with that of silica, a common dielectric coating, in our optical simulation study the covering of nanoparticles will be presumed as silica coating (metal@SiO_2) and can be well accounted for both organic ligands covering and dielectric coating effects.

In Fig. 8 we show the photocurrent enhancement factor η (%) of PSCs containing r=40, 70 nm, L=300 nm silver spheres placed both close to the top perovskite surface (Z_1 for r=40 nm and Z_5 for r=70 nm – see right panel in Fig. 5) and at the middle (Z_2), covered by silica shells of different thicknesses.

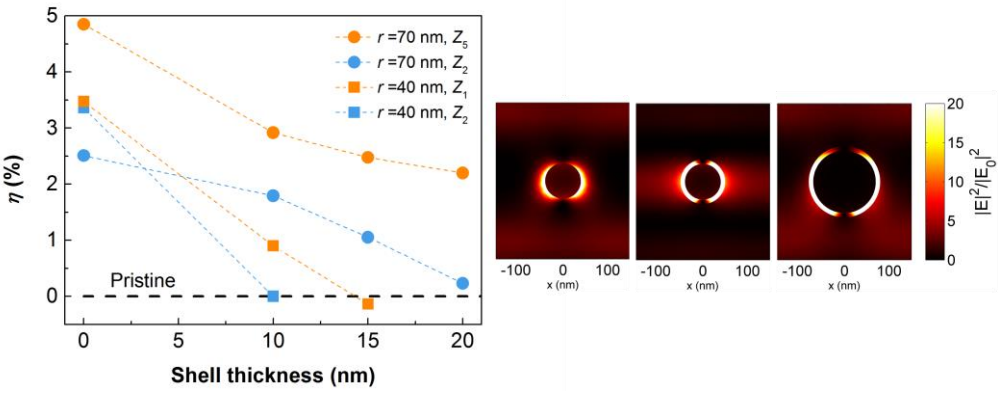

Fig. 8. Photocurrent enhancement factor η (%) of PSCs containing r=40 (lines with squares), 70 nm (lines with circles), L=300 nm silver spheres placed both close to the top surface of the perovskite layer (Z_1 for r=40 nm and Z_5 for r=70 nm - see right panel in Fig. 5) (orange lines) and at the middle (Z_2) (blue lines) as a function of silica shell thickness, compared to the pristine case. Right panel: Spatial distribution of the normalized electric field intensity at λ=779 nm for silica coated silver spheres (Ag@SiO_2): r=40@10 (middle), r=70@10 (right) compared to the uncoated r=40 nm case (left).

It can be seen that, although the overall light harvesting by the perovskite film is always larger for the uncoated particles case, the presence of a dielectric coating does not necessarily prompt the total collapse of the plasmonic enhancement effect, as long as (i) larger spheres are employed and shell's thickness is not too large, and (ii) especially if the larger spheres are placed close to the top surface of the perovskite layer.

An analysis of the spatial distribution of the calculated electric field intensity ($|\boldsymbol{E}|^2/|\boldsymbol{E}_0|^2$) reveals a strong localization of the optical fields inside the shell, in which no absorption takes place (see right panel in Fig. 8). However, for larger spheres this effect seems to be overwhelmed by their enhanced scattering, leading to maintenance of a high photocurrent enhancement, especially for smaller shell thicknesses (<15 nm). The inferior performance of the coated spheres is related also to another effect of the dielectric coating: it presents a low index environment for the spheres, resulting (especially for thick coatings) to a blue-shift of their plasmonic resonance compared to bare spheres in perovskite. Thus, for spheres showing a plasmonic resonance close to perovskite band edge the coating causes a shift of the resonance towards the high-absorption region of the perovskite where the presence of spheres is not that essential, especially for spheres deeply inside perovskite.

Nevertheless, as mentioned also above, although for most cases shell thicknesses higher than 20 nm should eventually cancel any plasmonic enhancement of the PCS efficiency, this is not the case for the r=70 nm Ag@SiO_2 spheres when placed close to the top of the perovskite surface. This is due to their antireflection property/effect, which is important not only close to the perovskite band-edge but also at lower wavelengths.

3.3 Plasmonic nanoparticles inside different than the perovskite layers of PSC

Due to the manufacturing procedure of the inverted PSC, the embedding of solution-processed metallic nanoparticles at different layers of the device other than the perovskite, e.g. inside the PEDOT:PSS and the PCBM carrier transporting layers, is possible without increasing the cost [20] as well as maintaining the planar architecture [36]. This way, plasmonic enhancement could be exploited without reducing the perovskite material, albeit at the price of reduced local field enhancement in the absorbing perovskite layer.

Furthermore, placing nanoparticles at the carrier transporting layers may facilitate other internal processes related to the electrical properties of the device. For instance, resonant metallic nanoparticles have been shown to be able to favor the electrical properties of the system too [20, 36, 37]. Increased exciton generation and dissociation (photocarrier generation, separation) due to the localized surface plasmon resonance oscillating fields that also extend inside the perovskite layer [12], improved carrier transport and extraction due to lower series or contact resistance [20, 37] of the solar cell and stability [38] are some examples of the additional impact of plasmonics in PSCs.

In this work we aim first to examine and improve the optical absorption of the PSC by incorporating metal nanoparticles inside the hole-transporting layer, PEDOT:PSS; this way we hope to minimize the reflection at the PEDOT:PSS-Perovskite interface. In the previous discussion we have revealed the importance of the reflection minimization, especially at the PEDOT:PSS-Perovskite interface. Particularly, we showed that the reflection from the multilayered device is the main reason resulting in decreased absorption in perovskite [Fig. 2(b)] along the entire spectrum ($300<\lambda<800$ nm), especially for $\lambda<550$ nm. Interestingly, the low refractive index of PEDOT:PSS ($n\sim1.41$) tunes the plasmonic resonances of metal nanoparticles at lower wavelengths (compared to the case of perovskite host) which coincide with this spectral region. The main restriction in the introduction of nanoparticles in the HTL/ETL is the small thickness of those layers (40, 50 nm) that limits the size of nanoparticles able to maintain the simplicity of the planar architecture. Employing small spheres, though, results to increase of the ohmic losses, as for small spheres absorption dominates extinction. Indeed, embedding spheres of radius $r\sim18$ nm in the PEDOT:PSS enhancement was achieved only for the case of aluminum, with maximum achievable photocurrent $J_{ph}=21.22$ mA/cm^2 [see Fig. 10(a)], corresponding to an enhancement of ~4% (assuming a perovskite layer thickness of 350 nm, and a spheres period of 65 nm). The photocurrent enhancement by embedding the nanoparticles in the PEDOT:PSS layer indicates the possibility to reduce the thickness of the perovskite layer, reducing thus the toxicity of the device (due to the lead content reduction), maintaining though its efficiency. Indeed, as is verified by related simulations, calculating the photocurrent for different perovskite layer thicknesses [see Fig. 9(b)], the thicknesses of about ~270 nm generate the same J_{ph} with that of the conventional (pristine) PSCs with the optimum thickness of ~350 nm. (The step-like behavior of J_{ph} as a function of perovskite thickness at around 275 nm, as observed in Fig. 9(b), is attributed to the appearance of a prominent FP resonance (at $\lambda\sim750$ nm for the 350 nm thickness) as we go from 200 to 300 nm thickness. We have to note that such a step-like response is not present in PSC device architectures with different carrier transport layers [16, 39].)

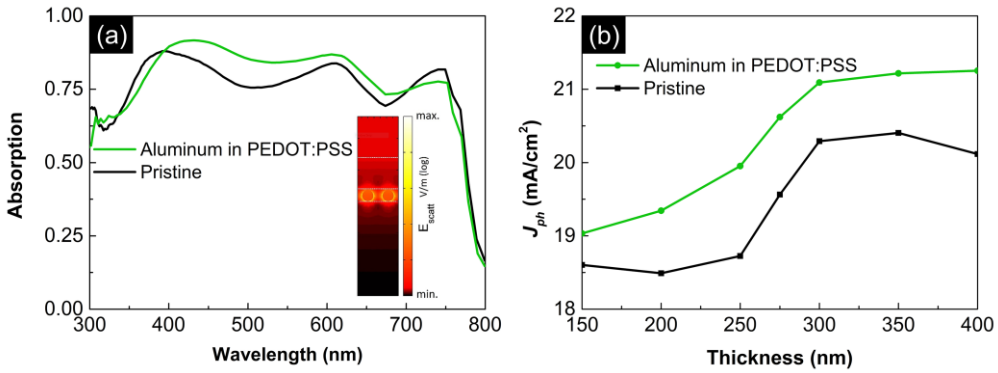

Fig. 9. (a) Absorption in perovskite for the pristine (black line) and the plasmonic PSC (green line) assuming aluminum spheres with radius equal to 18 nm and a period of 65 nm placed inside the PEDOT:PSS carrier transporting layer. The origin of the absorption enhancement is depicted at the right inset where the scattered field, due to the presence of the aluminum nanoparticles, is plotted for λ=517 nm. (b) J_{ph} of the pristine (black line), plasmonic PSC (green line) as a function of the perovskite thickness.

The origin of the absorption enhancement in the case of nanoparticles embedded in the PEDOT:PSS is the re-distribution of the incident light with enhanced scattering in the forward direction (towards the perovskite layer) along with the high local fields which are also extended inside the perovskite layer [see inset in Fig. 9(a)], in conjunction with the low parasitic absorption in aluminum nanoparticles.

Summarizing, we have to note that the antireflection property in PSCs with plasmonic nanoparticles placed in PEDOT:PSS offers a quite prominent absorption enhancement approach, especially at lower wavelengths (<550 nm), because there is no competition between the volume occupied by the metal particles and the absorptive perovskite material. Employing this approach allows employment of thinner perovskite layers, and thus reduction of the structure toxicity, without sacrificing the PSC performance. Placing nanoparticles in PEDOT:PSS is considered a reliable strategy regarding the enhancement of the overall efficiency of the solar cell, since studies have been shown it to favor the electrical properties of the system too [20, 36]. In addition, in this case we do not have a decline of the efficiency by coating the particles by a dielectric, i.e. employing Al@SiO_2. This is due to the low refractive index of the PEDOT:PSS matrix, like that of the coating layer.

Regarding incorporation of nanospheres inside the electrons transporting layer (PCBM), we found no enhancement, given the already known nanoparticle size restrictions owing to the small thickness of the ETL, as well as the impossible exploitation of antireflection at lower wavelengths (where the plasmonic resonance of nanospheres in PCBM, with n~2, occurs) in such depth of the PSC, given the highly absorptive nature of perovskite.

An approach to utilize the higher wavelengths (>500 nm) to achieve an efficiency enhancement is to utilize nanoparticles of different shape or different aspect ratio [40] to tailor their localized surface plasmon resonances and tune them at higher wavelengths. The most suitable candidates seem to be the nanorod-shaped particles, because they are synthesized in a wide range of aspect ratios [41] showing two localized dipole resonant modes (aligned with their “short” and “long” axis) and the mode aligned with the axis parallel to the PCBM layer (where no significant size restrictions exist) is highly tunable. The incorporation though of nanorod particles in the ETL layer of our system showed very limited absorption enhancement (due to increased near-field intensity at the vicinity of the nanorods that also extended inside the perovskite material), which was polarization dependent and it is questionable if can be observed in realistic systems (where disorder in the nanoparticle parameters is unavoidable).

Therefore, we conclude that utilizing plasmonic nanoparticles inside the PCBM is not recommended for improving the optical response of the PSCs. Other techniques should be

exploited here, i.e., nanostructuring on the back-reflector [42] as long as the interface transport resistance does not increase. Lastly, we note that nanoparticles can be placed inside the ITO layer too with a less harsh size constriction (ITO thickness ~100 nm). However, there they cannot contribute to the increase of the local fields inside the perovskite (since they are far from perovskite), thus their basic role will be to act as antireflectors. For that, nanoparticles of more complex geometry [43] or different shape [36] seem to be more appropriate than the spherical ones.

3.4 Optimizing PSC performance by combining plasmonic particles in different PSC layers

In this last section of our paper we aim to exploit the full potential of plasmonics in PSCs following our conclusions at earlier parts. This way, an enhanced absorption efficiency, compared to the conventional PSCs (with optimum thicknesses of about ~350 nm) could be achieved as well as the amount of the lead could be further reduced, using thinner perovskite absorbers or replacing perovskite by the nanoparticle material, without deteriorating the absorption.

The first step to explore the possibility of PSCs with reduced lead and high absorption efficiency is to examine and exploit the additive-like absorption behavior of spectrally separated resonances originating from nanoparticles at different PSC layers. For that reason, we utilize the combined effect of both aluminum nanospheres placed inside the PEDOT:PSS layer and of silver spheres located inside the perovskite. Aluminum spheres in PEDOT:PSS provide absorption enhancement at the range of $400<\lambda<700$ nm while silver spheres placed inside the perovskite layer, provide absorption enhancement at the region of $650<\lambda<800$ nm.

Figure 10(a) shows the absorption in perovskite of the combined case compared to the "individual" cases assuming a perovskite layer thickness of ~350 nm. Interestingly, a definite "additive" response is depicted, which is preserved for the whole range of perovskite layer thicknesses, from 400 up to 150 nm [see Fig. 10(b)], confirming the robustness of this approach. Indeed, the enhancement of the combined case equals the sum of the enhancements for only silver (in perovskite) and only aluminum (in PEDOT:PSS) spheres. We have to note here that the parameters used in this calculation have been obtained from the optimization studies discussed in the previous sections, but have been modified as to accommodate simulations, to minimize the probability to affect the electrical properties of the PSC and to ensure optimized combined case (i.e. with spheres in both PEDOT:PSS and perovskite layers). Thus, silver spheres of r=40 nm or r=30 nm, placed either in the middle or close to the bottom (position Z_4 of Fig. 5) of the perovskite layer have been employed (minimizing thus the interaction of the spheres in perovskite with those in the PEDOT:PSS), and the silver spheres periodicity in the combined case was considered 325 (i.e. 5×65) nm.

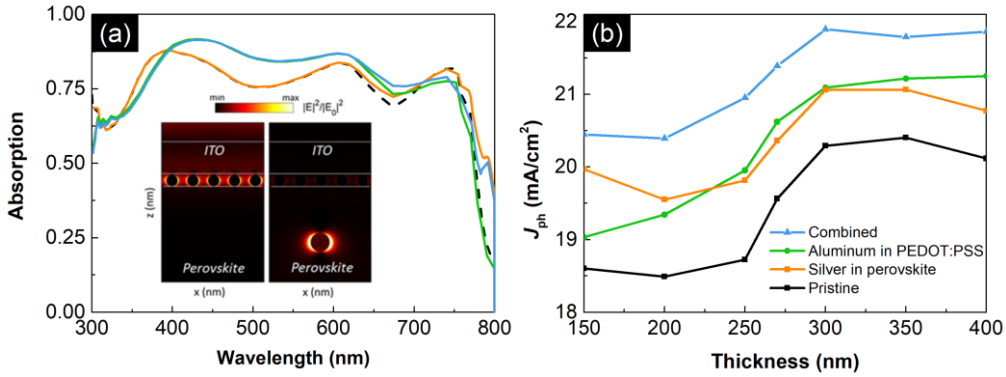

Fig. 10. (a) Absorption in perovskite with thickness equal to 350 nm for the following cases: pristine device (black dashed line), aluminum spheres placed inside the PEDOT:PSS (green

line – sphere radius 18 nm, period 65 nm), silver spheres inside the perovskite in the middle (orange line – sphere radius 30 nm, period 325 nm) and their combined case (blue line). Inset: Spatial distribution of the normalized electric field intensity for the combined case at λ=517 nm (left), λ=790 nm (right) verifying the "additive" response of spectrally separated resonances originating from nanoparticles at different PSC layers. (b) J_{ph} as a function of the perovskite thickness for the plasmonic PSCs. The green line corresponds to the case when only aluminum spheres (radius 18 nm, period 65 nm) are placed inside the PEDOT:PSS, the orange line corresponds to the case when only silver spheres are placed in the middle or close to the bottom (position Z_4 of Fig. 5) of the perovskite (with sphere radius of 40 nm and 30 nm respectively, and a period of 300 nm), the blue line shows the effect of the combination of aluminum spheres inside the PEDOT:PSS and silver spheres inside the perovskite in the middle or at Z_4 (with silver sphere radius of 30 nm, and a period of 325 nm); all results are compared to the pristine case (black line).

From Fig. 10(b) one can see that for a perovskite layer thickness equal to 150 nm the photocurrent reaches the record value J_{ph}=20.45 mA/cm^2. This result indicates that the lead content reduction can reach values up to 43% (taking into account only the thickness reduction), reducing this way the toxicity of the PSC by a great amount without reducing the photocurrent efficiency compared to conventional pristine PSCs with optimum perovskite thicknesses of about ~350 nm. Regarding the PSC of perovskite thickness 350 nm we found a maximum J_{ph}=21.80 mA/cm^2, corresponding to an enhancement of 6.8% relative to pristine PSC.

We have to note here, that the calculated J_{ph} was even higher than the values shown in Fig. 10(b), and equal to the champion 22.11 mA/cm^2 (~8.4% increase compared to pristine), assuming large silver spheres, with r=70 nm, placed close to the top surface of the perovskite layer (Z_5 see right panel in Fig. 5) with a thickness equal to 350 nm. The results in Fig. 10(b) though correspond to smaller spheres (r=30 nm), owing to the risk of increasing the interface transport resistance employing the larger ones.

Another parameter that is important for solar cell operation is the cell ability to absorb sunlight at off-normal incidence over a wide angular range (without requiring an expensive solar tracking system). To assess the robustness of the optimum parameters concluded in our study for different incidence angles, we calculated the dependence of J_{ph} on the incident angle for some of the above discussed optimum configurations and for the pristine case. The result, averaged over both TE and TM polarizations, is presented in Fig. 11.

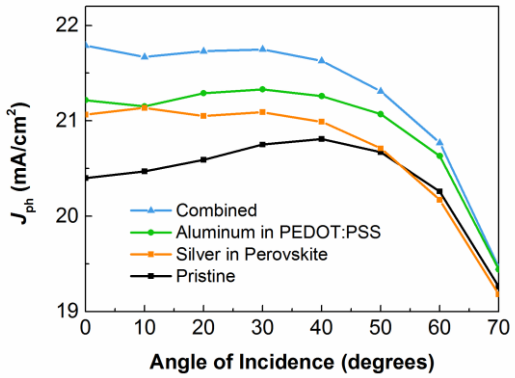

Fig. 11. Dependence of J_{ph} on incident angle averaged over both TE and TM polarizations for the plasmonic PSCs compared to the pristine case. The green line corresponds to the case when only aluminum spheres (radius 18 nm, period 65 nm) are placed inside the PEDOT:PSS, the orange line corresponds to the case when only silver spheres are placed in the middle or close to the bottom (position Z_4 of Fig. 5) of the perovskite (with sphere radius of 40 nm and 30 nm respectively, and a period of 300 nm), the blue line shows the effect of the combination of aluminum spheres inside the PEDOT:PSS and silver spheres inside the perovskite in the

middle or close to the bottom (position Z_4 of Fig. 5) (with sphere radius of 30 nm, and a period of 325 nm); all results are compared to the pristine case (black line).

As can be seen from Fig. 11, the J_{ph} of all plasmonic cases has no substantial degradation for incident angles up to 40 degrees. Moreover, for almost all the angular spectrum all plasmonic cases retain higher J_{ph} compared to the pristine.

11. Conclusions

We examined and discussed here the effect of plasmonic nanoparticles in realistic perovskite solar cells. Placing spherical nanoparticles in different layers of the PSC we examined the possibility to achieve enhancement in the light absorption and thus enhanced photocurrent density, J_{ph}, as well as the related conditions regarding nanoparticle material, size, vertical position and concentration, in particular for nanoparticles embedded in the perovskite layer. Moreover, we examined features that are likely to be present in a dispersion of metal particles in a realistic PSC, i.e. clustering formation and coating layers on the nanoparticles. Our study showed optimum response for silver nanoparticles of radius of around 60-70 nm, especially if placed close to the top of the perovskite layer, while the optimum nanoparticle distance was found to be around 300 nm. The calculated enhancement was found to be quite robust against nanoparticles randomness, polydispersity and angle of incidence. For silver spheres of r=70 nm an average photocurrent enhancement of 3.45%, corresponding to a J_{ph} equal to 21.11 mA/cm^2, was found. The origin of the photocurrent enhancement in all cases was the high local field values associated with the plasmonic resonances (which maximized the absorption), together with the enhanced scattering and antireflection properties of those particles, especially if placed close to the top of the solar cell.

We found considerable photocurrent enhancement (up to 4.0% corresponding to J_{ph}=21.22 mA/cm^2) also for nanoparticles placed in the hole transporting layer (PEDOT:PSS, on top of the perovskite layer) despite the small thickness of that layer and the associated restrictions in the nanoparticle size. The origin of the photocurrent enhancement there was the enhanced scattering in the forward direction (towards the perovskite layer) along with the high local fields which are also extended inside the perovskite layer. Here aluminum nanospheres (of r=18 nm and distance ~65 nm) gave the optimum performance.

The combined effect of placing both aluminum nanospheres in PEDOT:PSS and silver spheres in perovskite resulted at the champion 8.36% absorption enhancement (compared to the pristine case), corresponding to J_{ph} equal to 22.11 mA/cm^2, confirming the additive like absorption behavior of spectrally separated resonances originating from nanoparticles placed at different positions of the solar cell.

The absorption enhancement offered by the plasmonic nanoparticles in PSCs indicates the potential to employ PSCs with quite thin perovskite layers, e.g. 150 nm (thus with reduced toxicity due to the reduced amount of lead), maintaining though the performance of the current PSCs of optimum thickness 350 nm.

Summarizing, we found that embedding metal nanospheres inside realistic PSCs architectures provides a great strategy to improve the optical performance of the device as well as to decrease its toxicity without increasing the cost or the fabrication complexity.

Funding

This research has been co-financed by the European Union and Greek national funds through the Operational Program Competitiveness, Entrepreneurship and Innovation, under the call RESEARCH – CREATE – INNOVATE (T1EDK-01082).

References

1. N. K. Kumawat, M. N. Tripathi, U. Waghmare, and D. Kabra, "Structural, optical, and electronic properties of wide bandgap perovskites: experimental and theoretical investigations," J. Phys. Chem. A **120**(22), 3917–3923 (2016).
2. A. Kojima, K. Teshima, Y. Shirai, and T. Miyasaka, "Organometal halide perovskites as visible-light

sensitizers for photovoltaic cells," J. Am. Chem. Soc. **131**(17), 6050–6051 (2009).
3. *NREL Best research-cell photovoltaic efficiency chart*., (n.d.).
4. G. Kakavelakis, T. Maksudov, D. Konios, I. Paradisanos, G. Kioseoglou, E. Stratakis, and E. Kymakis, "Efficient and highly air stable planar inverted perovskite solar cells with reduced graphene oxide doped PCBM electron transporting layer," Adv. Energy Mater. **7**(7), 1602120 (2017).
5. G. Kakavelakis, I. Paradisanos, B. Paci, A. Generosi, M. Papachatzakis, T. Maksudov, L. Najafi, A. E. Del Rio Castillo, G. Kioseoglou, E. Stratakis, F. Bonaccorso, and E. Kymakis, "Extending the continuous operating lifetime of perovskite solar cells with a molybdenum disulfide hole extraction interlayer," Adv. Energy Mater. **8**(12), 1702287 (2018).
6. M. Anaya, G. Lozano, M. E. Calvo, W. Zhang, M. B. Johnston, H. J. Snaith, and H. Míguez, "Optical description of mesostructured organic–inorganic halide perovskite solar cells," J. Phys. Chem. Lett. **6**(1), 48–53 (2015).
7. Q. Lin, A. Armin, R. C. R. Nagiri, P. L. Burn, and P. Meredith, "Electro-optics of perovskite solar cells," Nat. Photonics **9**(2), 106–112 (2015).
8. A. H. Slavney, R. W. Smaha, I. C. Smith, A. Jaffe, D. Umeyama, and H. I. Karunadasa, "Chemical approaches to addressing the instability and toxicity of lead–halide perovskite absorbers," Inorg. Chem. **56**(1), 46–55 (2017).
9. L. J. Phillips, A. M. Rashed, R. E. Treharne, J. Kay, P. Yates, I. Z. Mitrovic, A. Weerakkody, S. Hall, and K. Durose, "Maximizing the optical performance of planar $CH_3NH_3PbI_3$ hybrid perovskite heterojunction stacks," Sol. Energy Mater. Sol. Cells **147**, 327–333 (2016).
10. H. A. Atwater and A. Polman, "Plasmonics for improved photovoltaic devices," Nat. Mater. **9**(3), 205–213 (2010).
11. H. Tan, R. Santbergen, A. H. M. Smets, and M. Zeman, "Plasmonic light trapping in thin-film silicon solar cells with improved self-assembled silver nanoparticles," Nano Lett. **12**(8), 4070–4076 (2012).
12. G. Kakavelakis, I. Vangelidis, A. Heuer-Jungemann, A. G. Kanaras, E. Lidorikis, E. Stratakis, and E. Kymakis, "Plasmonic backscattering effect in high-efficient organic photovoltaic devices," Adv. Energy Mater. **6**(2), 1501640 (2016).
13. J. D. Jackson, *Classical Electrodynamics* (Wiley, 1999).
14. C. Noguez*, "Surface plasmons on metal nanoparticles: the influence of shape and physical environment," (2007).
15. J. R. Krenn, A. Dereux, J. C. Weeber, E. Bourillot, Y. Lacroute, J. P. Goudonnet, G. Schider, W. Gotschy, A. Leitner, F. R. Aussenegg, and C. Girard, "Squeezing the optical near-field zone by plasmon coupling of metallic nanoparticles," Phys. Rev. Lett. **82**(12), 2590–2593 (1999).
16. A. Peer, R. Biswas, J.-M. Park, R. Shinar, and J. Shinar, "Light management in perovskite solar cells and organic LEDs with microlens arrays," Opt. Express **25**(9), 10704 (2017).
17. Q. G. Du, G. Shen, and S. John, "Light-trapping in perovskite solar cells," AIP Adv. **6**(6), 065002 (2016).
18. Z. Lu, X. Pan, Y. Ma, Y. Li, L. Zheng, D. Zhang, Q. Xu, Z. Chen, S. Wang, B. Qu, F. Liu, Y. Huang, L. Xiao, and Q. Gong, "Plasmonic-enhanced perovskite solar cells using alloy popcorn nanoparticles," RSC Adv. **5**(15), 11175–11179 (2015).
19. W. Zhang, M. Saliba, S. D. Stranks, Y. Sun, X. Shi, U. Wiesner, and H. J. Snaith, "Enhancement of perovskite-based solar cells employing core–shell metal nanoparticles," Nano Lett. **13**(9), 4505–4510 (2013).
20. G. Kakavelakis, K. Alexaki, E. Stratakis, and E. Kymakis, "Efficiency and stability enhancement of inverted perovskite solar cells via the addition of metal nanoparticles in the hole transport layer," RSC Adv. **7**(21), 12998–13002 (2017).
21. B. Cai, Y. Peng, Y.-B. Cheng, and M. Gu, "4-fold photocurrent enhancement in ultrathin nanoplasmonic perovskite solar cells," Opt. Express **23**(24), A1700 (2015).
22. N. K. Pathak and R. P. Sharma, "Study of broadband tunable properties of surface plasmon resonances of noble metal nanoparticles using mie scattering theory: plasmonic perovskite interaction," Plasmonics **11**(3), 713–719 (2016).
23. S. Roopak, A. Ji, P. K. Parashar, and R. P. Sharma, "Light incoupling tolerance of resonant and nonresonant metal nanostructures embedded in perovskite medium: effect of various geometries on broad spectral resonance," J. Phys. D. Appl. Phys. **50**(33), 335105 (2017).
24. J. Stratton, *Electromagnetic theory*, (2007).
25. S. Carretero-Palacios, M. E. Calvo, and H. Míguez, "Absorption enhancement in organic–inorganic halide perovskite films with embedded plasmonic gold nanoparticles," J. Phys. Chem. C **119**(32), 18635–18640 (2015).
26. S. Carretero-Palacios, A. Jiménez-Solano, and H. Míguez, "Plasmonic nanoparticles as light-harvesting enhancers in perovskite solar cells: a user's guide," ACS Energy Lett. **1**(1), 323–331 (2016).
27. P. Docampo, J. M. Ball, M. Darwich, G. E. Eperon, and H. J. Snaith, "Efficient organometal trihalide perovskite planar-heterojunction solar cells on flexible polymer substrates," Nat. Commun. **4**(1), 2761 (2013).
28. Z. Xiao, C. Bi, Y. Shao, Q. Dong, Q. Wang, Y. Yuan, C. Wang, Y. Gao, and J. Huang, "Efficient, high yield perovskite photovoltaic devices grown by interdiffusion of solution-processed precursor stacking layers," Energy Environ. Sci. **7**(8), 2619–2623 (2014).
29. R. Wu, J. Yang, J. Xiong, P. Liu, C. Zhou, H. Huang, Y. Gao, and B. Yang, "Efficient electron-blocking

layer-free planar heterojunction perovskite solar cells with a high open-circuit voltage," Org. Electron. **26**, 265–272 (2015).
30. E. D. Palik, *Handbook of Optical Constants of Solids. II* (Academic Press, 1998).
31. *Solar Spectral Irradiance: Air Mass 1.5*, https://rredc.nrel.gov/solar/spectra/am1.5/.
32. G. Kakavelakis, K. Petridis, and E. Kymakis, "Recent advances in plasmonic metal and rare-earth-element upconversion nanoparticle doped perovskite solar cells," J. Mater. Chem. A **5**(41), 21604–21624 (2017).
33. J. Burschka, N. Pellet, S.-J. Moon, R. Humphry-Baker, P. Gao, M. K. Nazeeruddin, and M. Grätzel, "Sequential deposition as a route to high-performance perovskite-sensitized solar cells," Nature **499**(7458), 316–319 (2013).
34. M. Omelyanovich, S. Makarov, V. Milichko, and C. Simovski, "Enhancement of perovskite solar cells by plasmonic nanoparticles," (2016).
35. R. Wu, B. Yang, C. Zhang, Y. Huang, Y. Cui, P. Liu, C. Zhou, Y. Hao, Y. Gao, and J. Yang, "Prominent efficiency enhancement in perovskite solar cells employing silica-coated gold nanorods," J. Phys. Chem. C **120**(13), 6996–7004 (2016).
36. H.-L. Hsu, T.-Y. Juang, C.-P. Chen, C.-M. Hsieh, C.-C. Yang, C.-L. Huang, and R.-J. Jeng, "Enhanced efficiency of organic and perovskite photovoltaics from shape-dependent broadband plasmonic effects of silver nanoplates," Sol. Energy Mater. Sol. Cells **140**, 224–231 (2015).
37. Z. Sun, Y. Xiahou, T. Cao, K. Zhang, Z. Wang, P. Huang, K. Zhu, L. Yuan, Y. Zhou, B. Song, H. Xia, and N. Chen, "Enhanced p-i-n type perovskite solar cells by doping AuAg@AuAg core-shell alloy nanocrystals into PEDOT:PSS layer," Org. Electron. **52**, 309–316 (2018).
38. N.-G. Park, "Perovskite solar cells: an emerging photovoltaic technology," Mater. Today **18**(2), 65–72 (2015).
39. J. M. Ball, S. D. Stranks, M. T. Hörantner, S. Hüttner, W. Zhang, E. J. W. Crossland, I. Ramirez, M. Riede, M. B. Johnston, R. H. Friend, and H. J. Snaith, "Optical properties and limiting photocurrent of thin-film perovskite solar cells," Energy Environ. Sci. **8**(2), 602–609 (2015).
40. S. Eustis and M. A. El-Sayed, "Determination of the aspect ratio statistical distribution of gold nanorods in solution from a theoretical fit of the observed inhomogeneously broadened longitudinal plasmon resonance absorption spectrum," J. Appl. Phys. **100**(4), 044324 (2006).
41. B. N. and and M. A. El-Sayed*, "Preparation and growth mechanism of gold nanorods (nrs) using seed-mediated growth method," (2003).
42. T. Shen, S. Siontas, and D. Pacifici, "Plasmon-enhanced thin-film perovskite solar cells," J. Phys. Chem. C acs.jpcc.8b07063 (2018).
43. W. Liu, J. Zhang, B. Lei, H. Ma, W. Xie, and H. Hu, "Ultra-directional forward scattering by individual core-shell nanoparticles," Opt. Express **22**(13), 16178 (2014).